Optimization and Characterization of Facility Effects for a Low-Power Electron Cyclotron Resonance Magnetic Nozzle Thruster

by

Benjamin N. Wachs

A dissertation submitted in partial fulfillment
of the requirements for the degree of
Doctor of Philosophy
(Aerospace Engineering)
in The University of Michigan
2022

Doctoral Committee:

Assistant Professor Benjamin Jorns, Chair
Assistant Professor Al-Thaddeus Avestruz
Professor John Foster
Professor Alec Gallimore
Professor Mark Kushner

We are as gods and might as well get good at it.

-Stewart Brand

Benjamin Natan Wachs

bwachsumich.edu

ORCID iD: 0000-0001-7935-700X

© Benjamin Natan Wachs 2022

To my parents.

ACKNOWLEDGEMENTS

My foray into the world of Electric Propulsion began with a flyer; one that (like a thruster) would forever change my life's trajectory. While this flyer proved oddly prescient at times, it did not foretell all of the many people who would shape my graduate school experience and without which this document would not have been possible.

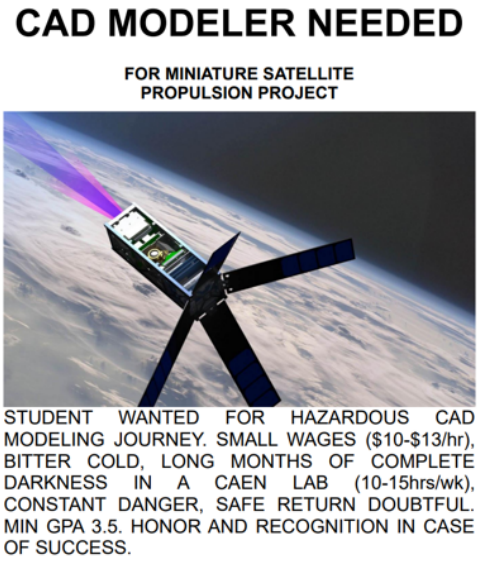

Figure 0.1: Flyer that started it all.

I want to start by thanking my committee members: Prof. Mark Kushner, Dean Alec Gallimore, Prof. John Foster, and Prof. Al-Thaddeus Avestruz, and to my NASA mentor Dr. Kamhawi: your guidance inside and outside of the classroom has given me the skills needed to complete this journey. Thank you for the candid advice pertaining to plasma physics and beyond. To my advisor, Ben Jorns: though having the same first name did not ultimately give me the leg-up on the competition I was hoping for, I have learned a great deal under your guidance. You have pushed me, through first principles approaches, to be a more thorough scientist, a better writer (the need was apparent), and to improve my dead-pan delivery.

While we are on the topic of Bens, I owe a great deal of gratitude to Ben Longmier who introduced me to the field and has served as a friend and mentor ever since. Your

optimism is contagious and you have been a great sounding board for some of my own crazy ideas. Thanks for your support over all these years.

I owe an enormous debt to my labmates, past and present. Though you may be terrible at picking vacuum chamber colors, you have been welcoming and extremely helpful over the years. Scott, Tim, Sarah, Marcel, Frans, and Ethan, thanks for showing me the ropes. Josh, Shad, Zach, and Matt, it has been a pleasure getting grilled with you. If any of you figure out what a plasma is, please let me know. I look forward to reunions to come. To Sophia, Sal, and Jack: thanks for filling in for me when my days of avoiding COVID finally came to an end. The final experiments of this thesis would not have been possible without your dedication. Zach, all those late nights in the lab would not have been survivable without your humor and industrial sized stash of goldfish. Leanne, thanks for bringing a bit of youthfulness to the lab, I am glad I could spend so much time in the presence of a true acronym prodigy. To all of the next generation of PEPLers: good luck, I wish you the best on this journey.

To Eric: I should probably set aside an entire chapter for all the many ways you have assisted me over the years, but instead I will give you this paragraph. Thanks for the many hours of leak checking and climbing around the chamber with me. I will always strive for your friendliness, engineering abilities, and mile time.

There have been many others who have shaped my engineering career outside the confines of 1919 Green Road; I will not be able to mention everyone. Perhaps the next dissertation will have a more complete list. My career in the sciences would not have been possible without Dr. Hurwitz, whose high school classes brought me into this orbit and whose lessons I still use to this day. To those who I have worked with in industry: thanks for keeping me (somewhat) tied to reality. A special thanks to the entire Apollo Fusion crew for showing me a thing or two about vacuum chambers, communal lunches, and most importantly, pivoting. Dr. Bob, without your guidance, the thesis writing process would have been a lot more disorganized to say the least. You provided clarity and and expert advice for navigating "the academy".

My time in Ann Arbor has lasted a bit longer than expected in no small part because of all the wonderful people I met outside of the lab. My time here has been deeply enriched by everyone who survived living with me at 420 High Street. I'm sure it wasn't easy. Asta, who encouraged me to try out this whole grad school thing. Laura, for expanding my horizons beyond what I (and especially my parents) could have dreamed. You have been a great study partner and friend over the years. Michael, who turned my freshmen year quest for free food at Hillel into a decade long friendship and mentorship. Ani for all of your many check-ins over the years and making sure I didn't starve.

The last chapters of this thesis and my time in Ann Arbor would not have been possible without Kate (who shares a last name with the lab). Thank you for welcoming me into your home, encouraging me when things were not exactly going as planned, laughing at (some of) my jokes, and the many 2 AM rides to the lab to check on the cryos. I am lucky that my journey through COVID lockdown and melted experiments eventually led to meeting you.

Finally, to my parents who made this all possible: thank you. You have encouraged me, taught me to be just a little less stubborn, and supported me through the thick

and thin. Despite not having science backgrounds, you always listened to my ideas and provided some level-headed advice. To my grandmother: your positive attitude and sense of humor were an inspiration throughout this process. I will finish this acknowledgements section with the sage advice given by my mom hours before my first prelim "just remember Ben, you might not fail".

This thesis was funded by NASA fellowship 80NSSC17K0157.

TABLE OF CONTENTS

LIST OF FIGURES

Figure

LIST OF TABLES

Table

LIST OF APPENDICES

Appendix

NOMENCLATURE

α_T	Transmission coefficient
$\dot{m}$	mass flow rate
η	Efficiency
Γ	Reflection coefficient
$\mathcal{V}$	Thruster volume
ω_{ce}	Electron cyclotron frequency
ω_{pe}	Plasma frequency
σ	Cross section
ε_0	Permittivity of free space
ε_e	Electron energy
A_e	Exit area
B	Magnetic flux intensity
c	Speed of light
F_T	Thrust force
g	Earth gravitational acceleration

h Edge-to-center density ratio

I_{sp} Specific Impulse

K Coupling coefficient

k_B Boltzmann constant

K_{ex} Excitation rate constant

K_{iz} Ionization rate constant

l Thruster length

m_e electron mass

m_g Neutral mass

M_{detach} Detachment Mach number

n_e Electron density

n_e Plasma density

n_g Neutral density

P^M Measured power

P^T Thruster power

P_{abs} Absorbed power

P_{Fwd} Forward power

P_{in} Power input

P_{Refl} Reflected power

q Electron charge

R	Thruster radius
T_i	Ion temperature
T_e	Electron temperature
u_B	Bohm velocity
u_e	Exit velocity
v_e	Exhaust velocity
Z	Impedance

ABSTRACT

The modelling, proper experimental testing techniques, and optimization of an electron cyclotron resonance magnetic nozzle thruster is investigated. A zero-dimensional model using spatially averaged quantities is constructed to predict thruster performance trends based a set of free model parameters. From these simulations, it is found that wall losses and magnetic nozzle efficiency are the key drivers of thruster performance. An overview of the thrust and input power measurement techniques is presented, including a rigorous uncertainty analysis for measured thrust and efficiency. The consequences of on-ground vacuum facility pressure and wall proximity are then investigated, and a model is constructed to extrapolate measurements taken with finite pressure to space-like environments. Finally, the setup and results of an optimization experiment seeking to improve thruster efficiency using custom input waveforms are presented. The waveforms investigated include single-frequency and two-frequency tuning and pulsed modulation. It is found that thruster performance is closely linked to input frequency for single-frequency tuning while two-frequency and pulsed modulation are not shown improve thruster efficiency beyond the single-frequency maxima for the powers and flow rates investigated.

CHAPTER I

Introduction

1.1 Small Satellite Technology

Not such a long time ago (in this very galaxy), spaceflight was accessible only to large government entities and deep-pocketed companies (who often went bankrupt in the process). Satellites of this age were large multi-million dollar behemoths that took years to develop and cost hundreds of millions of dollars to launch. This paradigm has fundamentally shifted over the past decades with the advent of Small Satellite (SmallSat) technology and the decrease in spacecraft launch costs.

SmallSats, typically defined as satellites with launch weights under 600 kg, are now commonly employed for commercial and research applications with uses ranging from communication to remote sensing. Often these SmallSats, such as SpaceX's Starlink, are launched as parts of large constellations of satellites, which can cover greater areas of Earth while being less prone to single-point-failures than traditional satellite services. This technology has been enabled by the continued miniaturization of key satellite components, which in turn, owes much credit to the consumer electronics industry [122].

The SmallSat market has seen exponential growth over the past decade, with over 1,500 satellites launched in 2021. We show an overview of these trends from a recent industry report in Fig. 1.1. This growth has led to the development of new

industries and supply chains and has enabled satellite manufacturers to employ mass manufacturing techniques, putting further downward pressure on the cost of these technologies.

The work presented in this dissertation focuses on SmallSats with less than 50 Watts of available power for propulsion. Such satellites tend have launch masses around 10 kg ($\sim$ 6U CubeSat) with established use cases ranging from earth imaging to low bandwidth communications.

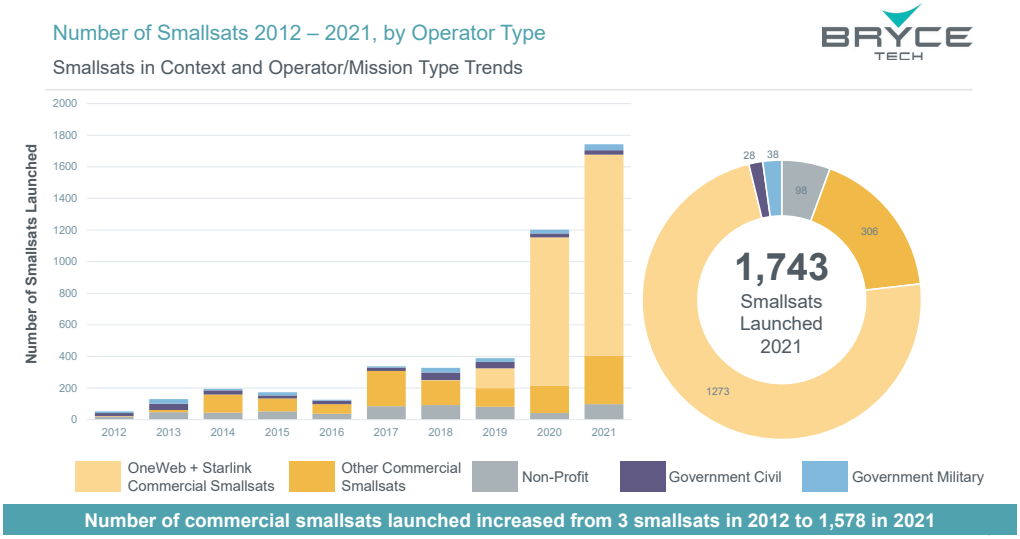

Figure 1.1: Number of SmallSats launched per year. Reproduced from BryceTech [4].

1.2 In-Space Propulsion

In-space propulsion plays a critical role in modern satellite systems, allowing them to station-keep, maneuver to different obits, overcome drag, and, increasingly, avoid collisions with other satellites. A satellite's in-space maneuverability is typically characterized using the total amount of velocity change, ΔV, available to the satellite. This metric can be calculated using the Tsiolkovsky rocket equation:

$$\Delta V = v_e \ln\left(\frac{M_i}{M_f}\right), \tag{1.1}$$

where v_e is the propellant exhaust velocity, M_i is the initial mass of the spacecraft (including on-board propellant), and M_f is the final spacecraft mass. From this equation, it is apparent that high exhaust velocities are desirable for maximizing the ΔV provided by the on-board propellant. We characterize the efficiency with which on-board propellant is utilised using specific impulse:

$$I_{sp} = \frac{F_T}{\dot{m}g}, \tag{1.2}$$

where F_T is the force produced by the thruster, $\dot{m}$ is the mass flow rate of the propellant, and g is the earth's acceleration due to gravity, 9.81 m/s^2.

Generally speaking, on-board propulsion can be divided into three categories: chemical, cold gas, and Electric Propulsion (EP). As the name implies, chemical propulsion relies on chemical reactions to heat a propellant and generate thrust– typically through the use of a convergent-divergent nozzle. A drawback of this technology is that the exhaust velocity is limited by the energy released during the combustion process. Furthermore, the propellant used in these thrusters—namely hydrazine or its derivatives—is highly toxic and difficult to handle.

Cold gas thrusters operate by releasing compressed gas through a nozzle. The expansion of the gas produces thrust, as in a chemical thruster. These thrusters are very simple in operation; however, they produce limited ΔV as the specific energy available from compressed gas is significantly lower than that of chemical propellants.

Electric propulsion uses electrical energy to accelerate an on-board propellant. Because electrical energy can be harvested in-flight, typically with solar panels, EP thrusters are not limited by the energy contained within the propellant [54]. The ΔV generated by these thrusters is therefore dictated by the availability of on-board power and the efficiency of the conversion from electrical power to propellant kinetic

energy, typically defined as:

$$\eta = \frac{F_T^2}{2\dot{m}P_{in}}, \tag{1.3}$$

where P_{in} is the electrical power input to the thruster . However, the conversion of electrical power to thrust power necessarily requires an on-board power processing unit, which adds weight to the satellite. Thus the optimal thruster system will depend on the mission at hand.

Examples of established EP technologies include resistojets, arcjets, electrosprays, pulsed plasma thrusters, ion thrusters, and Hall effect thrusters, and magnetic nozzle thrusters [54; 24; 67]. These devices use a variety of methods to transfer electrical energy into propellant kinetic energy. This includes electrothermal (resistojets, arcjets), electrostatic (electrospray, ion thrusters, Hall thrusters), and electromagnetic (pulsed plasma thrusters, magnetic nozzle thrusters). Each of these technologies has advantages and drawbacks in terms of engineering difficulty and fundamental limitations.

1.2.1 SmallSat Propulsion

Historically, most in-space propulsion technologies were developed with large satellites in mind. Options for SmallSat propulsion were therefore more limited. Given the tight mass requirements that often accompany SmallSat launches, EP thrusters are an obvious candidate for many SmallSat missions. The high specific impulse provided by EP thrusters (and thus low propellant usage) yields impressive cost savings and enables constellation-type missions that would be prohibitively expensive or difficult with the larger mass and volume footprint used by chemical propulsion [53; 64; 109]. As such, low-power (< 500 W) EP technology has seen a rapid growth in recent years [48; 67; 68; 85; 60; 3].

While it is possible in theory to scale down many EP technologies for use in SmallSats, their efficiency tends to decrease substantially at smaller scales. This

effect is in large part due to the higher electron thermal fluxes and ion recombination losses caused by the increased surface area to volume ratio inherent to miniaturized designs. Because of these trends, the design of SmallSat propulsion remains an active area of research.

Over the past decades, research and development into these technologies has included low-power ion thrusters, Hall thrusters, electrospray thrusters, magnetic nozzle thrusters, and other concepts [126; 79; 76; 25]. We show a rendering of an earlier low-power magnetic nozzle concept for CubeSats in Fig. 1.2.

Figure 1.2: Rendering of a CubeSat with a proposed plasma thruster.

While low-power thrusters have been commonplace in laboratories for over a decade, it is only in recent years that these devices have been flown in space [100; 14; 61]. Having said that, no single EP thruster has yet been established as the dominant technology for this market, particularly for the sub-200 watt class of satellites. We show in Table 1.1 a sample of existing commercially available SmallSat thruster technologies and their reported specifications [4]. We note here that the calculated efficiencies may not include power losses within the power processing unit and neutralizer (in the case of Hall and ion thrusters); thus the total system efficiency is often lower than that reported here.

The focus of this dissertation is magnetic nozzle thrusters, which we describe in more detail in the following section. These thrusters in principle can be scaled down to smaller sizes while avoiding some of the wall losses inherent to scaling down similar technologies such as Hall effect thrusters. However, as shown in 1.1, their efficiency has historically been low at sub-kilowatt power levels.

Table 1.1: State-of-the-art Commercially Available Low-Power Thrusters

Thruster	**Type**	**Power (W)**	**Thrust (μN)**	I_{sp} **(s)**	η **(%)**
Busek BGT-X5	Greeen Monoprop	N/A	5×10^5	220	N/A
Accion TILE-3	Electrospray	20	450	1650	18
Enpulsion IFM Nano	Electrospray	40	350	3500	15
ThrustMe NPT30	Gridded Ion	~ 50	~ 800	~ 1000	~ 6
Busek BHT-200	Hall Thruster	250	13000	1390	35
Exotrail ExoMG nano	Hall Thruster	53	2000	800	14
CU Aerospace FPPT-1.6	PPT	48	270	2400	6.6
T4i Regulus	Magnetic Nozzle	50	550	550	3
Phase Four Maxwell	Magnetic Nozzle	450	5500	800	4.8

1.3 Magnetic Nozzle Thrusters

Magnetic nozzle thrusters are an electrodeless form of electric propulsion that offer several potential advantages over state-of-the-art technologies [54; 13]. They in principle can have longer lifetimes as they do not require the types of plasma wetted electrodes that often are the life limiting components of conventional EP systems. Primarily, they do not require a neutralizer cathode, which is a known failure source on many EP devices [83]. Furthermore, these devices can be more resilient (though

not impervious) to plasma surface interactions, enabling the use of more exotic or storable propellants such as metal and water. Proposed magnetic nozzle thruster concepts range in power from tens of watts to hundreds of kilowatts, making them a viable technology for both large-scale interplanetary missions and nano-satellites [10; 113; 16]. The increasing demand for propulsion in small spacecraft missions in the past decade has led to a particular emphasis on magnetic nozzle development at lower powers.

Magnetic nozzles rely on a shaped magnetic field to turn randomized thermal energy into directed kinetic flow. This conversion is a complex process that varies with different magnetic nozzle designs [72]. For the low power designs that are actively being explored for small satellite propulsion, power is absorbed primarily by plasma electrons. These heated electrons are expelled through the magnetic nozzle setting up an ambipolar field that accelerates ions from the plasma source. A schematic overview of this process is shown in Fig. 1.3.

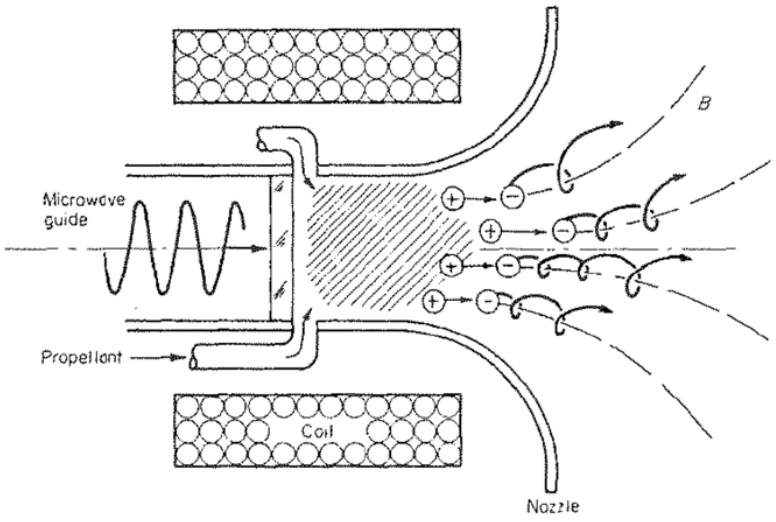

Figure 1.3: Early magnetic nozzle thruster concept. Reproduced from Ref. [54].

Magnetic nozzle thrusters are among the earliest EP concepts, with pioneering work beginning in the 1960s [59; 44; 87]. However, this research was largely abandoned in favor of ion thrusters and Hall thrusters, in part due to the bulky and inefficient

microwave power supplies available at the time. Interest in these devices was briefly renewed during the 1990's [102; 50], and has seen a thorough revival in the past two decades with projects ranging from over a hundred kilowatts [34] to hundreds of watts [115; 97], and, as we explore in this thesis, tens of watts [25; 15]. Practical application of these devices for in-space propulsion has been enabled largely by new solid-state RF and microwave power generators that are a fraction of weight and volume of the vacuum tubes used previously.

Most of the research into low-power magnetic nozzle thrusters to date has focused on helicon designs. In these devices, input propellant is ionized and heated by a radiofrequency helicon wave [23; 111]. These heating mechanism in theory can sustain highly dense plasmas, thus enabling high thrust densities which are advantageous for small thrusters. However, direct thrust measurements of these devices has often shown that their efficiencies at low powers (< 100 Watts) is on the order of 1% [97; 106].

1.3.1 Heating Schemes

In this section, we provide an overview of the two predominant heating mechanisms employed in magnetic nozzle thruster designs: Helicon wave heating and electron cyclotron resonance heating. These heating mechanisms both target plasma electrons, making these devices electron-driven magnetic nozzle thrusters. Other less common heating schemes for these thrusters include inductive coupling and ion cyclotron resonance.

1.3.1.1 Helicon Heating

Helicon plasmas are generated by launching a right-hand polarized electromagnetic wave into a bounded, magnetized plasma. For these waves to exist, the input frequency must fall between the ion cyclotron and electron cyclotron frequencies. The

dispersion relation for these waves is given by

$$\omega = \frac{k_0^2 \omega_{pe}^2}{k k_z \omega_{ce}}, \tag{1.4}$$

where k_z is the axial component of the wave vector, $k = (k_\perp^2 + k_z^2)^{1/2}$ is the magnitude of the wave vector, and $k_0 = \omega/c$.

Typically these waves are generated using a 13.56 MHz radiofrequency source with a magnetic field in the 100's of Gauss. The input electromagnetic wave is absorbed through a combination of collisional heating, Landau damping, and conversion to Trivelpiece-Gould modes, though the exact mechanisms are complex and likely vary between sources [23]. The densities produced in this process are in theory higher than those attainable at similar power levels using inductive coupling or DC power, which has made them attractive for use in propulsion where high plasma density is needed for high thrust density (N/m^2) [22]. To date, their have been several thruster prototypes using this heating mechanism. However, at low powers, their efficiency has typically been under 10% [115; 124; 97; 75; 90].

1.3.1.2 Electron Cyclotron Resonance Heating

ECR heating and ECR plasmas are commonly employed in a wide variety of plasma engineering fields including fusion [105], plasma processing [123], ion production [40], and propulsion [118]. ECR heating utilizes the phenomenon that electrons will naturally gyrate in the presence of a magnetic field with a frequency given by the electron cyclotron frequency:

$$\omega_{ce} = \frac{qB}{m_e}, \tag{1.5}$$

where q is the electron charge, B is the magnetic field strength, and m_e is the electron mass. By applying an alternating electric field with a frequency equal to that of the electron cyclotron frequency, the electrons experience a constant energy gain,

leading to resonant heating. A diagram of this process is shown in Fig. 1.4. By directly coupling to energy to electrons, ECR heating can generate high energy, non-maxwellian electron populations.

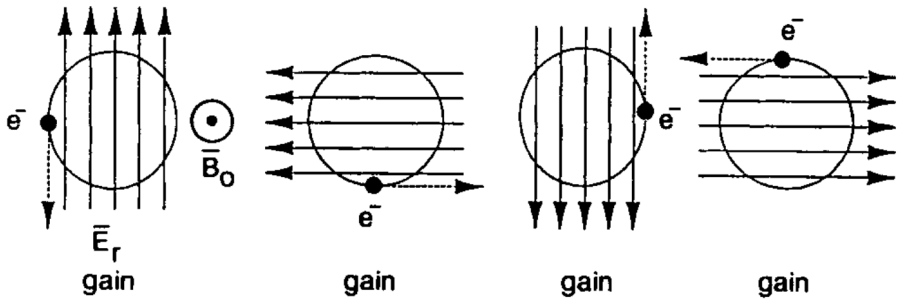

Figure 1.4: Electron energy gain caused by a right-hand polarized wave during ECR heating, from Ref. [69].

As an aside, we note the special case of overdense plasmas in which the excitation frequency, ω_{ce}, is less than the plasma frequency,

$$\omega_{pe} = \sqrt{\frac{n_e q^2}{m_e \varepsilon_0}}, \tag{1.6}$$

where n_e is the plasma density and ε_0 is the permittivity of free space [40]. In these plasmas, strong non-linear effects can dominate the wave heating physics making their theoretical analysis challenging.

A typical ECR source used in plasma processing is powered by 2.4 GHz microwaves, corresponding to a resonant magnetic field of $B_{res} \approx 875$ Gauss. Because most ECR sources, including the thrusters described in this thesis, have an axisymmetric magnetic field that varies in strength along the axis of the device, the resonant condition is only met at a single plane within the source, leading to strong local heating [58].

1.3.2 Coaxial ECR Magnetic Nozzle Thrusters

In the past decade, pioneering work by the Office National d'Etudes et de Recherches Aérospatiales (ONERA) has demonstrated significant efficiency gains for low-power magnetic nozzle thrusters [55; 16]. Their research used Electron Cyclotron Resonance (ECR) heating to power the thruster using microwave power. Specifically, the technology developed at ONERA employs a coaxial microwave injection ECR design. We provide a schematic view of one such thruster in Fig. 1.5. In these designs, a coaxial structure excites a Transverse Electromagnetic (TEM) wave within the thruster's discharge region, which then heats the plasma. These thrusters have demonstrated thrust efficiencies over of $\eta > 10\%$ while operating at under 50 watts input power [118; 92]. This represents an order of magnitude improvement over similar helicon-type thrusters.

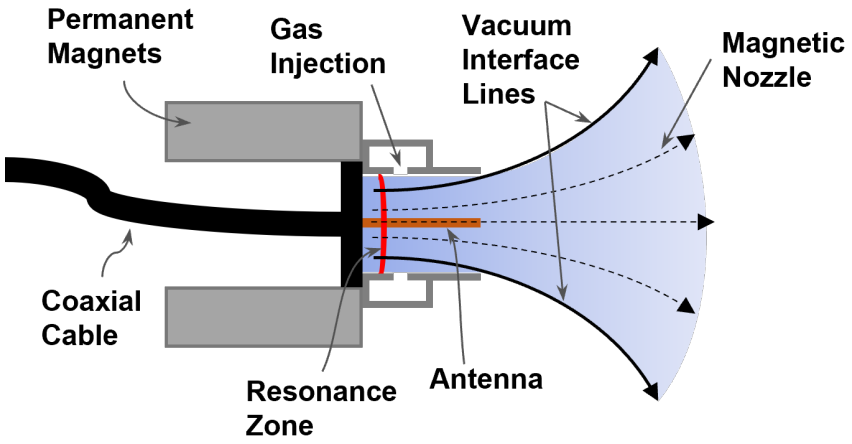

Figure 1.5: Schematic view of a coaxial ECR thruster.

Owing to the high efficiency demonstrated by these designs, several similar thrusters, including the devices tested in this dissertation (shown in in Fig. 1.6), have been developed based on the coaxial ECR architecture [101; 104].

While these thrusters have demonstrated high efficiencies in laboratory settings, the physical mechanisms underlying their performance remain unknown. In particular, it is not well understood why the switch from helicon to ECR heating pro-

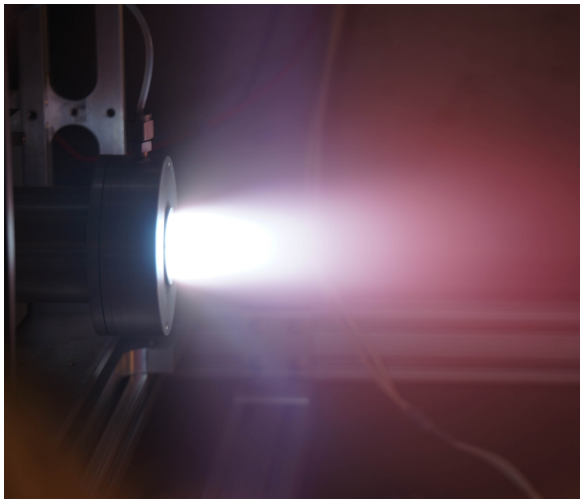

Figure 1.6: Coaxial ECR magnetic nozzle thruster firing in the Junior Vacuum Facility at the University of Michigan.

duces such marked efficiency improvements. Thus, while state-of-the-art coaxial ECR thrusters have demonstrated efficiencies competitive, if not exceeding, most low-power (sub-100 W) EP technologies, it is likely that further improvements can be made.

1.4 Objectives of Current Research

Given the high performance demonstrated by coaxial ECR magnetic nozzle thrusters and lack of high fidelity models for these devices, it is clear that this technology warrants further research and development. To this end, the objectives of the research presented in this dissertation are threefold. First, we seek to develop models of the low-power ECR thrusters to understand performance trends and inform potential avenues for improvement. Second, we aim to develop proper testing techniques for these devices. This includes translating and extrapolating on-ground measurements to space-like environments, which, in turn, requires understanding the effects vacuum chamber testing on thruster performance. Finally, we attempt to develop new techniques for improving thruster efficiency. Namely, we apply waveform optimization using automated testing techniques to increase the thrust produced these devices

while holding the input power and flow rate constant.

1.5 Dissertation Organization

This remainder of this thesis is unorganized as follows: In Chap. II, we present a zero-dimensional model of thruster performance. Chapter III overviews testing techniques for ECR magnetic nozzle thrusters including the thruster and facility used in our experiments. In this chapter, we provide an in-depth procedures for measuring microwave power absorbed by the thruster and determining thrust force produced by these devices. In Chap. IV, we present a series of experiments seeking to measure the effects of vacuum facilities on thruster performance. From these experiments, we construct a model that captures the detrimental effects of background pressure on thruster efficiency. Chapter V details the setup and results of a series of optimization experiments that use different microwave waveforms to improve thruster performance. Finally, we summarize our findings and provide suggestions for future work in Chap. VI.

CHAPTER II

Zero-Dimensional Modeling of the ECR Thruster Operation and Optimization

2.1 Introduction

In this chapter, we construct a first principles based model of the ECR thruster. Modelling plasma systems of any scale, be it solar winds or television pixels, involves numerous complex physical phenomena including gas kinetics, electromagnetic wave propagation, electron transport, surface reactions, and turbulence. Partially owing to these complexities, to date, theoretical and numerical models have not been able to accurately predict the experimentally measured performance of magnetic nozzle thrusters. As such, we do not attempt to increase the fidelity of existing models in this section, but rather introduce a simplified model of the thruster from which we can derive performance trends and describe theoretical device limitations. We then use this model to elucidate potential avenues of thruster efficiency improvements. In particular, we look at the effects of wall losses, increased nozzle efficiency, and pulsed operation.

2.2 Existing Magnetic Nozzle Thruster Models

Several theoretical analyses of magnetic nozzle thrusters have been developed since their inception in the 1960s. Kosmahl proposed a model based on single particle motion for an early ECR accelerator [59]. Sercel built on this early work to develop a quasi-1D model of an ECR thruster that included cross-field diffusion [102]. With the reemergence of magnetic nozzle technologies in the 2000s, a number of analyses have been published including models by Fruchtman [38] examining thrust produced by a 1D plasma source. More complex two-dimensional models were introduced by Ahedo and Navarro-Cavalle that examined the magnetic nozzle expansion [5]. Scaling laws derived by Little using a 2D fluid model suggested that high efficiency nozzle operation depended on high electron temperatures [71]. Recent work has examined the role of non-equilibrium electron dynamics in these devices [8][82]. Finally, particle-in-cell simulations have been constructed and are under development to provide more detailed picture of the underlying physics [36][96].

For the purposes of modelling, magnetic nozzle thrusters are often analyzed as an upstream plasma source and a downstream magnetic nozzle region. While this simplification makes modelling efforts more tractable, it is likely that the complex interplay between these two regions plays a critical role in device performance. In the source region, the plasma electrons absorb power from an external power source i.e. RF or microwave coupling. The hot electrons sustain the plasma generation and pull the ions from the thruster in an ambipolar acceleration process. The thruster exit plane is treated similarly to that of a traditional rocket nozzle throat, with upstream ions being accelerated to the Bohm velocity — as opposed to the the sonic velocity in gas kinetic nozzles. In the magnetic nozzle region, downstream of the exit plane, energy from the magnetized plasma electrons is converted to ion kinetic energy in the plume. At some point downstream of the exit plane, the plasma detaches from magnetic field lines, and the influence of the magnetic nozzle is no longer felt

[73][49][6][32][91].

An issue commonly encountered in these analyses is that of the electron thermodynamics within the magnetic nozzle. Because ions in this region draw their energy from electron thermal motion, assuming isothermal electrons along magnetic field line, a simplification often employed in EP, would imply infinite heat flux from the plasma source. To avoid this problem, models often use a polytropic index in the nozzle to relate electron temperature and density [103][114][28][81][120]. However, this assumption fails to capture some of the non-equilibrium dynamics that can occur in the nozzle. Recent work by *Hepner and Jorns* [45] has examined the role of instabilities in driving both heat flux and cross-field transport in magnetic nozzles.

The analysis presented in this chapter draws from the semi-empirical quasi-1D helicon thruster model developed by Lafleur [62]. The model solves the electron temperature and plasma density using a quasi-1D continuity equation coupled to a 1D momentum balance and global energy conservation equation. It employs an empirical fit from previous studies to assign a radial density profile in the thruster– and thus radial wall losses. The model makes the simplification of isothermal electrons in both the source and nozzle regions. Plasma detachment and electron heat flux are accounted for by assuming that ions detach at the location where the ion gyroradius is equal to the radius of the magnetic field lines emanating from the thruster exit plane. This detachment point has been measured experimentally under certain conditions but is not a universally observed phenomenon [21]. Other detachment criteria have been proposed by Olsen [91] and Arefiev [10].

With a predetermined detachment point, it is possible to calculate the ion mach number at detachment, and subsequently, the energy that is transferred from the plasma source to the nozzle. Our model uses a similar formulation, but neglects the radial and axial plasma profiles within the thruster and leaves radial losses and detachment mach number as free parameters. In doing so, we have generalized the

Lafleur model to allow for different nozzle dynamics and radial diffusion physics at the expense of generating more free parameters.

2.3 Zero-Dimensional Plasma Model

Zero-dimensional models, often referred to as global models, use spatially-averaged quantities to construct a system of equations from which global plasma properties are calculated. These models can incorporate any number of physical processes depending on their level of sophistication. Typically this will include electron-impact ionization and excitation, neutral gas dynamics, surface reactions, and other physical and chemical processes.

The thruster model presented in this chapter uses electron impact ionization, electron impact excitation, and wall recombination reactions for xenon atoms and singly charged ions. These processes can be described using:

$$e^- + Xe \Rightarrow e^- + e^- + Xe^+ \tag{2.1}$$

$$e^- + Xe \Rightarrow e^- + Xe^* \tag{2.2}$$

$$e^- + Xe^+ + \text{wall} \Rightarrow Xe, \tag{2.3}$$

where Xe^+ is singly charged xenon ion and Xe^* represents an average excited state xenon neutral. The ionization and average excitation energies used in the model are 12.13 and 8.32 eV, respectively [86]. We note here that the energy consumed by excitation collisions in the thruster model is not recovered, and as such, introduces an energy loss mechanism during thruster operation.

The reaction rates for the above ionization and excitation processes are governed by a reaction rate constant, K, which is calculated by averaging over the electron

energy distribution function and the reaction cross section:

$$K = \int_0^\infty f(\varepsilon) \left(\frac{2\varepsilon}{m_e}\right)^{1/2} \sigma(\varepsilon)\, d\varepsilon, \tag{2.4}$$

where ε is the electron energy, $f(\varepsilon)$ is the electron energy distribution function, and $\sigma(\varepsilon)$ is the reaction-specific cross section.

The reaction rate formulation relies on a predetermined electron energy distribution function (EEDF). In our case, we use a Maxwellian distribution; the EEDF produced by electrons in thermodynamic equilibrium:

$$f(\varepsilon) = 2\sqrt{\frac{\varepsilon}{\pi}} \left(\frac{1}{k_B T_e}\right)^{3/2} \exp\left(-\frac{\varepsilon}{k_B T_e}\right), \tag{2.5}$$

where T_e is the plasma electron temperature and k_B is the Boltzmann constant. Using this approach, we can derive an empirical expression for the rate constant for each reaction as a function of only electron temperature: $K \equiv K(T_e)$.

We note here that while the Maxwellian distribution is often used in describing ECR plasmas, these plasmas are inherently non-thermal and typically contain different velocity distributions in the directions parallel and perpendicular to the applied magnetic field [40]. Determining the degree to which these plasmas differ from thermodynamic equilibrium requires more extensive modelling and will not be explored in this chapter. However, there is evidence that the non-equilibrium EEDF produced by ECR heating in these thrusters can drive performance, and these effects remain an open area of research [93][30].

The xenon cross-sectional data used for modeling excitation and ionization reactions in our model are provided in Fig. 2.1a. From these models, we can derive rate constants for xenon ionization and excitation, K_{iz} and K_{ex}, as functions of electron temperature, as shown in Fig. 2.1b. At a first glance, the rate constants illustrate

that at low electron temperatures ($T_e < 11$ eV), excitation collisions dominate ionization collisions, indicating that excitation losses can be minimized by operating the thruster at higher electron temperatures.

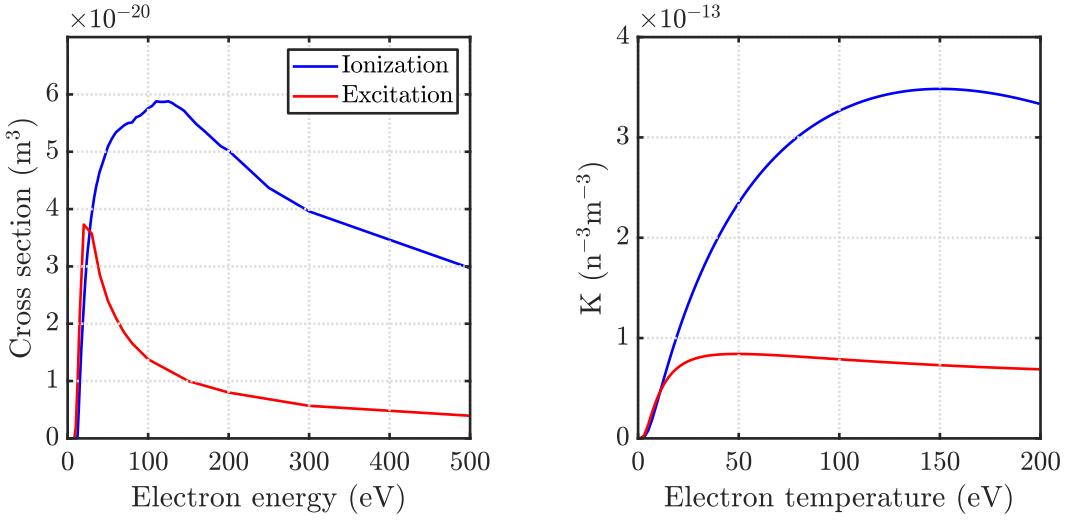

Figure 2.1: (a) Xenon cross sections and (b) xenon rate constants for ionization and excitation with electron temperatures ranging from 0 to 200 eV [86].

2.4 Thruster Model Description

A diagram illustrating the processes modelled in the thruster is shown in Fig. 2.2. Physically, the model can be understood as follows:

1. Neutral xenon gas enters the thruster through the propellant feed system.
2. Electrons bombard neutral atoms ionizing a fraction of the gas.
3. Ions diffuse to thruster walls and exit plane.
4. Ions at thruster boundaries are accelerated to the Bohm speed and fall through a sheath potential.
5. Ions and electrons recombine to form neutral xenon at the thruster walls.

6. Ions exiting the thruster are further accelerated through the magnetic nozzle, gaining energy from electrons in the nozzle.

7. Plasma detaches from the magnetic nozzle.

A similar model for argon plasmas is given in Ref. [41].

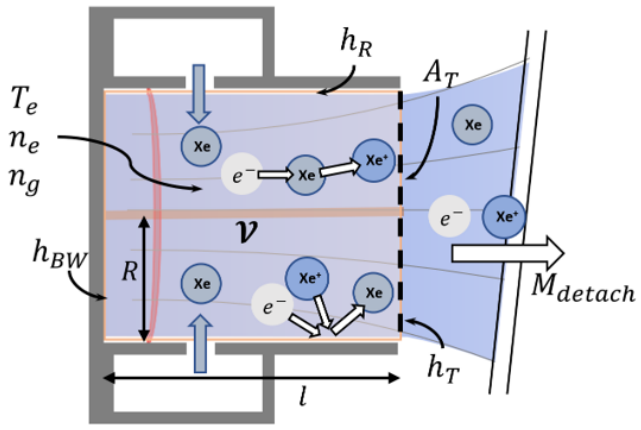

Figure 2.2: Thruster discharge region showing ionization, recombination and ion acceleration processes.

The plasma within the thruster (the discharge region) is assumed to be quasi-neutral and approximated as uniform density, similar to the models described by *Lieberman and Lichtenberg* [70]. This is a departure from the helicon thruster model developed by *Lafleur* [62], which uses radially and axially dependent plasma profiles. The model employs a coupled particle continuity and energy balance to solve for neutral density, plasma density, and electron temperature.

The conservation equations governing the overall process are described by:

$$\frac{\mathrm{d}N}{\mathrm{d}t} = \dot{N}_{in} - A_T(\Gamma_g + \Gamma_i) \tag{2.6}$$

$$\frac{\mathrm{d}}{\mathrm{d}t}\left(\frac{3}{2}N_e q_e T_e\right) = P_{\mathrm{abs}} - P_{\mathrm{loss}}\ , \tag{2.7}$$

where N is the total number of ions and neutrals inside the thruster, $\dot{N}_{in}$ is the input neutral flow rate (set by a flow controller), A_T is the thruster exit area, and Γ_g and Γ_i

are the neutral and ion fluxes, respectively. In Eq. 2.7, the left hand side represents the time rate of change of the total electron energy, where N_e is the total number of plasma electrons within the thruster. On the right hand side of the equation, P_{abs} is the total power absorbed by the plasma, which is an input to the model. The P_{loss} term represents a summation of the powers lost to collisions, walls losses, and the thruster plume, as we detail in Sec. 2.4.4. Our description of the energy balance assumes that all externally applied power is absorbed by plasma electrons. This is generally the case for RF and ECR plasmas but does not apply to heating schemes that target ions such as ion cyclotron resonance devices.

2.4.1 Ion Particle Balance

The ion particle balance accounts for ions generated through electron-impact ionization and lost through diffusion to the thruster walls and the thruster exit plane. In the model, ions are accelerated to the Bohm velocity at the sheath edges forming at the thruster walls. We additionally make the assumption that ions reach the Bohm speed at the thruster exit plane. Ion velocity measurements taken on by *Collard and Jorns* [28] on a higher density magnetic nozzle device have shown that the sonic transition can occur downstream of the throat, but accurately modelling the transition from the plasma source into the magnetic nozzle is beyond the scope of a 0D model.

Mathematically, the ion particle balance can be described as

$$\frac{\mathrm{d}n_e}{\mathrm{d}t} = n_e n_g K_{iz} - \frac{n_e u_B A_{eff}}{\mathcal{V}}. \tag{2.8}$$

The left hand side of this equation gives the time rate of change of the plasma density, where n_e is the electron (and thus ion) density. The first term on the right hand side of the equation represents the ionization rate where n_g is the neutral density and K_{iz} is the rate constant for ionization reactions, as given in Eq. 2.4. The second term

is the ion loss rate where u_B is the Bohm speed given by $u_B = \sqrt{qT_e/m_i}$, and $\mathcal{V}$ is the thruster volume. A_{eff} is a the effective loss area, which accounts for ion density variations near the walls and exit plane. This can be expressed as

$$A_{eff} = \pi R^2 h_T + \pi R^2 h_{BW} + 2\pi R l h_R, \tag{2.9}$$

where R and l are the thruster radius and length. The terms h_T, h_{BW}, and h_R are plasma edge-to-center density ratios at the exit plane, back wall, and radial walls, respectively. A more detailed description of these h-factors is provided in *Lieberman and Lichtenberg* [70]. For the back wall and exit plane, these ratios are calculated using a plasma diffusion model for parallel plates. Diffusion to the radial walls in the thruster involves cross-field transport, which cannot be easily modelled for these low-pressure conditions. Additionally, because the thruster walls are conducting, there are also short circuiting effects at play [107]. Because of the complex phenomena at play, we use the nominal unmagnetized radial diffusion value for a base case model, but leave h_R as a free parameter in our parameter sweeps. From Ref. [70], the unmagnetized axial and radial h-factors are:

$$h_T = h_{BW} \approx 0.86 \left(3 + \frac{l}{2\lambda_\mathrm{i}}\right)^{-1/2} \tag{2.10}$$

$$h_R \approx 0.8 \left(4 + \frac{R}{\lambda_\mathrm{i}}\right)^{-1/2}, \tag{2.11}$$

where λ_i is the ion mean free path. For the conditions simulated in this chapter, we find $h_T \approx 0.5$ and $h_R \approx 0.4$. For the magnetized conditions, we expect h_R to decrease compared to this nominal value, as the magnetic field impedes radial diffusion.

2.4.2 Neutral Particle Balance

The model provides two sources of neutral propellant: the propellant flow into the thruster and ion-electron recombination at thruster walls. Neutrals in the system are lost to ionization collisions and diffusion through the thruster exit plane. Excited state neutrals are not treated separately from ground state neutrals for the particle balance. The particle flow into the thruster can be expressed in terms of mass flow rate, $\dot{m}$, which is typically an experimentally controllable quantity, as

$$\dot{N}_{in} = \frac{\dot{m}}{m_g}, \tag{2.12}$$

where m_g is the propellant's molecular mass ($m_g = 2.180 \times 10^{-25}$ kg for xenon). The neutral flux generated by ion recombination is calculated as

$$\dot{N}_{recomb} = n_e u_B A_{recomb}, \tag{2.13}$$

where A_{recomb} is an effective area for ion recombination. For our model, this area is composed of the thruster back wall and radial walls:

$$A_{recomb} = h_{BW}\left(\pi R^2\right) + h_R\left(2\pi R l\right). \tag{2.14}$$

Here, we have included the h factors to create an effective loss area for the plasma, as in the previous section.

Due to the low neutral densities and accompanying low collision rates inherent to this thruster design, we assume that the neutrals behave according to free-molecular-flow dynamics. Thus the neutral flux exiting the thruster can be expressed as

$$\Gamma_g = \frac{1}{4} n_g u_g, \tag{2.15}$$

where u_g is the characteristic neutral speed at the thruster exit plane. The neutral speed is given by the mean thermal velocity:

$$u_g = \sqrt{\frac{8k_B T_g}{\pi m_g}}, \tag{2.16}$$

where T_g is the neutral gas temperature, and m_g is molecular mass. The propellant enters the thruster at room temperature, $T_g \approx 300K$. As an aside, we note that for higher neutral densities, the flux exiting the thruster will follow the sonic velocity, with $\Gamma_{g(sonic)} = n_g\sqrt{\gamma K_B T_g/m_g}$.

The rate of neutral loss to ionization can be expressed using

$$\frac{\mathrm{d}n_g}{\mathrm{d}t}_{ionization} = -\frac{\mathrm{d}n_e}{\mathrm{d}t}_{ionization} = -\left(n_e n_g k_{iz}\right), \tag{2.17}$$

Combining the above equations, we arrive at the rate equation used for neutral species in the model:

$$\frac{\mathrm{d}n_g}{\mathrm{d}t} = \frac{\frac{\dot{m}}{m_i} - \frac{1}{4}n_g u_g A_T + n_e u_B A_{recomb}}{\mathcal{V}} - \left(n_e n_g k_{iz}\right). \tag{2.18}$$

By calculating the neutral flux from the thruster exit plane, we can evaluate the thruster's mass utilization efficiency, η_{MU}, using

$$\eta_{MU} = \frac{\dot{m} - A_T \Gamma_g m_g}{\dot{m}}. \tag{2.19}$$

This expression provides a measure of the fraction of input propellant that is ionized and accelerated by the thruster. The remaining propellant escapes the thruster as neutral atoms, generating a small amount of momentum transfer in the form of cold gas thrust. Ultimately, however, the neutrals that diffuse through the exit plane cannot be accelerated by the thruster, which directly leads to a reduction in thruster

efficiency.

2.4.3 Magnetic Nozzle Detachment

The ion speed at the magnetic nozzle detachment point is described using a detachment mach number, M_{detach}. The detachment velocity and location are complex functions of electron heat flux and cross field diffusion physics that are active areas of research. As such, we simulate M_{detach} for two different speeds to study these trends in Sec. 2.5.1.2. For our base case models, we use the value from the Lafleur model [63], which uses the point at which the ion gyroradius equals the radius of the thruster exit plane. Using a 1-D momentum balance, this detachment point is found by solving

$$\frac{1}{2}\left(M_{detach}^2 - 1\right) - \ln M_{detach} = \ln\left(\frac{qB_0^2 R_T^2}{m_i T_i}\right), \tag{2.20}$$

where R_T is the thruster radius, B_0 is the magnetic field strength at the thruster exit, and T_i is the ion temperature, $T_i \approx 300$ K. Using our thruster parameters, this gives a nominal value of $M_{detach} = 1.8$.

2.4.4 Power Balance

Using Eq. 2.7, we can express the power loss term, P_{loss}, in terms of the the average energy lost to each ion-electron pair. In the description presented here, the energy loss accounts for the ion and electron energies at the sheath edge. We split the average energy loss per ion electron pair, ε_{tot}, into four terms,

$$\varepsilon_{tot} = \varepsilon_c + \varepsilon_i + \varepsilon_{e(W)} + \varepsilon_{e(T)}, \tag{2.21}$$

where ε_c is the energy lost to collisions, ε_i is the ion energy at the sheath edge, $\varepsilon_{e(W)}$ is the electron energy at the sheath edge adjacent to the walls and $\varepsilon_{e(T)}$ is the electron

energy at the exit plane (the throat) of the thruster. Thus P_{loss} can be expressed as

$$P_{loss} = \frac{d\varepsilon_{tot}}{dt}. \tag{2.22}$$

The collisional energy, ε_c is the sum of the average energies lost to ionization and excitation collisions:

$$\varepsilon_c = \mathcal{E}_{iz} + \frac{K_{ex}}{K_{iz}}\mathcal{E}_{ex}, \tag{2.23}$$

where $\mathcal{E}_{iz}$ is the first ionization energy (12.13 eV) and $\mathcal{E}_{ex}$ is the average excitation energy (8.32 eV) composed of the summation of the first several excites states of the neutral xenon atom [43]. This number may be an underestimate for the actual excitation losses that are incurred when accounting for each xenon excited state cross section, but provides a first order estimate. The energy lost to elastic collisions between electrons and neutrals is assumed to be small and is not accounted for in this model.

The ion energy at the sheath edge, which accounts for acceleration to the Bohm speed, can be expressed as

$$\varepsilon_i = \frac{T_e}{2}. \tag{2.24}$$

The electron energy at the wall sheath edges, $\varepsilon_{e(W)}$, is comprised of the electron kinetic energy and the energy transferred to ions through the sheath potential,

$$\varepsilon_{e(W)} = 2T_e + \varepsilon_{sheath}, \tag{2.25}$$

where the $2T_e$ term represents the average electron kinetic energy and ε_{sheath} is the sheath potential given by

$$\varepsilon_{sheath} = \frac{T_e}{2}\ln\left(\frac{m_i}{2\pi m_e}\right). \tag{2.26}$$

We note here that this value is an approximation as the actual sheath potential will be affected by the presence of a magnetic field and secondary electron emission effects.

For electrons exiting the thruster, we augment the ε_e term to include the energy transferred to the ions in the magnetic nozzle. This can be expressed as

$$\varepsilon_{e(T)} = 2T_e + \varepsilon_{ei(plume)}, \tag{2.27}$$

where $\varepsilon_{ei(plume)}$ is the energy transferred from electrons to ions in the magnetic nozzle:

$$\varepsilon_{ei(plume)} = \frac{1}{2} M_{detach}^2 T_e. \tag{2.28}$$

The right hand side of this equation gives the ion kinetic energy at the magnetic nozzle detachment point. It should be noted that the $2T_e$ term in this equation assumed isothermal electrons in the plume, which is non-physical but often employed in first order models.

Using the above equations, we can characterize the total power loss, P_{loss}, in terms of the power absorbed by collisions, the thruster walls, and the thruster plume:

$$P_{collisions} = \mathcal{V}\left(q_e n_e n_g K_{iz} \varepsilon_c\right) \tag{2.29}$$

$$P_{wall} = q_e n_e u_B A_{recomb}\left(\varepsilon_{e(W)} + \varepsilon_i\right) \tag{2.30}$$

$$P_{Plume} = q_e n_e h_T u_B A_T\left(\varepsilon_{e(T)} + \varepsilon_i\right). \tag{2.31}$$

Combing the above equations, the total power balance becomes

$$\frac{\mathrm{d}}{\mathrm{d}t}\left(\frac{3}{2} e n_e \mathrm{T_e}\right) = \frac{P_{abs}(t) - (P_{\mathrm{collisions}} + P_{\mathrm{wall}} + P_{\mathrm{plume}})}{\mathcal{V}}. \tag{2.32}$$

2.4.5 Force Derived from Simulations

Beginning with the general thrust equation, we can derive the force produced by the simulated thruster:

$$T = \dot{m} u_e + (p_e - p_a) A_e, \tag{2.33}$$

where $\dot{m}$ is the mass flow rate exiting the thruster, u_e is the exit velocity, p_e and p_a are the nozzle exit and ambient pressure, respectively, and A_e is the exit area. The ambient pressure, p_e, is negligible for a space-like environment. The exit pressure is given by

$$p_e = qT_e n_e, \tag{2.34}$$

where T_e is in units of eV.

For our derivation, we neglect the force produced by neutrals exiting the thruster. Thus the effective mass flow rate for the purpose of force calculation can be written as

$$\dot{m} \approx \dot{m}_i = m_i h_T u_e n_e A_e, \tag{2.35}$$

where n_e is the average plasma density within the thruster . The exit velocity is the ion velocity at the location where the plasma detaches from the magnetic field. As previously discussed, this location and the physics driving detachment are poorly understood phenomena. For the purposes of our model, we simplify the physics and assign a single detachment Mach number to the thruster. Using this assumption, we can write the exit velocity as

$$u_e = M_{detach} u_B. \tag{2.36}$$

2.4.6 Key Assumptions

The model presented above makes several key assumptions about the nature of the plasma which we will repeat here for clarity:

1. No multi-step ionization or multiply charged ions
2. Uniform plasma throughout source region
3. Ions reach Bohm velocity at walls and exit plane
4. Single detachment speed and location
5. Isothermal, Maxwellian electron population

It should be noted that while we assign an isothermal temperature to the electron population throughout the plasma source and plume regions of the thruster, we allow for heat flux. While this in nonphysical, it allows the simulation to be solved without complete knowledge of the heat flux dynamics within the thruster, which is an open area of research.

2.5 Steady State Simulations

Setting the time varying terms in Eqs. 2.8-2.32 to zero, we can solve for the steady-state electron temperature, neutral density, and plasma density using a standard non-linear systems solver. We provide the dimensions of the simulated thruster in Table 2.1. In Fig. 2.3 we present the results of these simulations for the thruster operating at 1 sccm xenon. Here, we have used to h-factors listed in Eqs. 2.10-2.11 and have used a nominal detachment mach number of $M_{detach} = 1.8$.

Table 2.1: Thruster Parameters Used in Simulations

Thruster Length , l (mm)	**Thruster Radius, R (mm)**	**Flow Rate (sccm)**
20	13.25	1.00

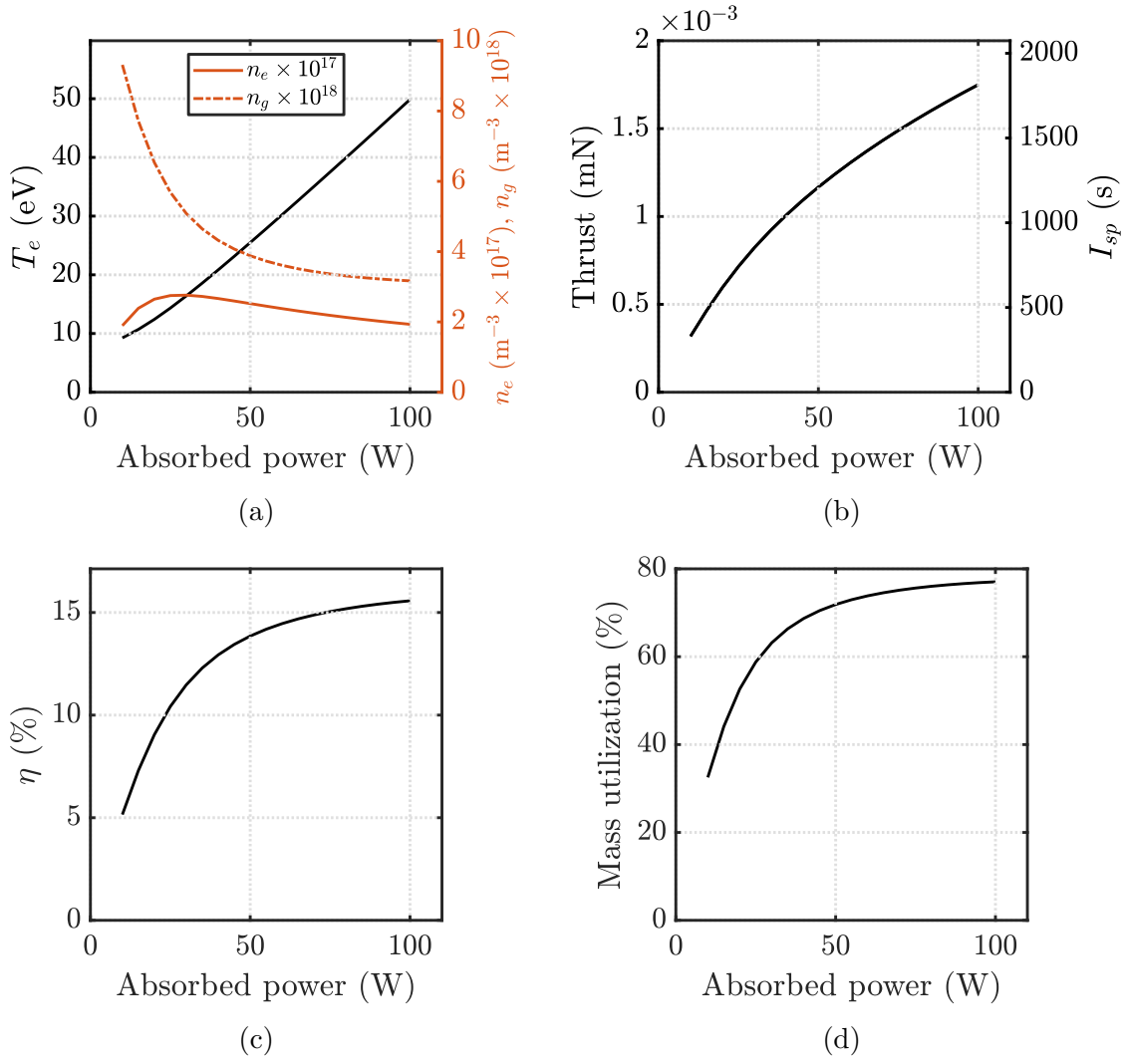

Figure 2.3: (a) Electron temperature, plasma and neutral density within the thruster (orange), (b) specific impulse (c) thrust efficiency, and (d) mass utilization efficiency vs. absorbed power, P_{abs} for 1 sccm xenon flow rate.

The plots show that as absorbed power increases the plasma density (Fig. 2.3a) reaches a maximum at $P_{abs} \approx 30$ W after which it monotonically decreases with power. This effect is caused by increased fraction of ionized propellant creating a deficit in neutral xenon atoms available to ionize and sustain the discharge. As ions are created, they leave the thruster at a rate proportional to the Bohm speed, lowering the total density of ions and neutrals ($n_e + n_g$) in the thruster. From Eq. 2.8, this necessarily results in a higher ionization rate constant, $K_{iz}(T_e)$, to sustain a stable

discharge. For xenon, this pushes T_e higher for electron temperatures under 150 eV, which is a much higher than typically seen in EP. When the absorbed power increases beyond $\sim$ 100W, the model becomes unstable as the rate constant cannot compensate for the decreased ion and neutral density. We note here that this pattern of electron temperature scaling with absorbed power stands in contrast to constant pressure plasma reactors in which T_e is determined by pressure and geometry [69].

As an aside, it is interesting to note that the calculated plasma densities (Fig. 2.3a) correspond to plasma frequencies in the range of $f_{pe} \sim 4$ GHz. Thus, with the input microwave frequencies ($1000 < f < 2500$ MHz) used in the experiments conducted in the following chapters, these simulations predict that the plasma will be overdense [40].

The model predicts that for the specified operating conditions, the total thrust efficiency, η, will remain below 20%. The predicted mass utilization efficiency (Fig. 2.3d) shows that for powers greater than 20 W, over 50% of the propellant is utilized. Therefore, we cannot ascribe the majority of the efficiency losses to underutilized propellant.

Plotting the constituent powers in Fig. 2.4, we find that most of the power input to the thruster is lost to the radial walls as ions are accelerated through the sheath potential. The ion momentum at the radial walls is perpendicular to the thrust vector and thus does not contribute to usable thrust. This suggests that shielding the walls can significantly increase thruster performance, as will be explored in the next section.

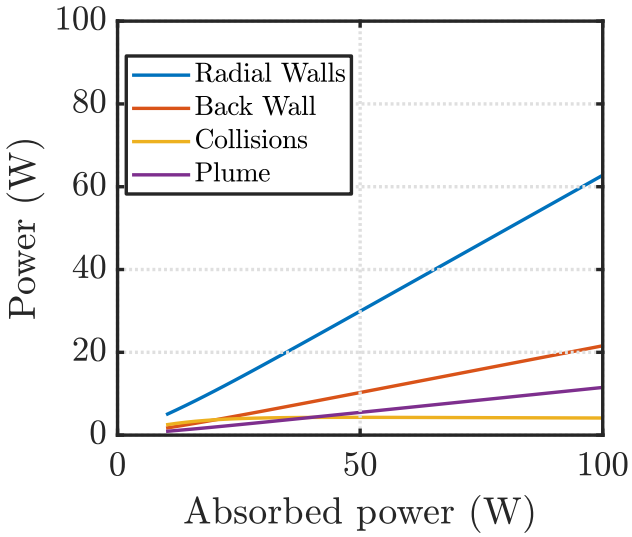

Figure 2.4: Power absorbed by wall losses, collisions, and the thruster plume.

2.5.1 Parameter Sweeps

In this section, we investigate the effects of varying two of the crucial, yet poorly understood parameters in our model: the radial edge-to-center density ratio, h_R, and the detachment Mach number, M_{detach}. By sweeping these parameters, we can simulate the effects of better plasma confinement and a more efficient magnetic nozzle.

2.5.1.1 Radial Confinement Sweep

We simulate various degrees of plasma confinement in the radial direction, i.e. how much the magnetic field shields the walls from the plasma by sweeping h_R through three values: $h_R = 0.1$, $h_R = 0.3$, and $h_R = 0.5$. Here, we have kept the propellant flow rate at 1 sccm xenon and set the detachment Mach number to its nominal value of $M_{detach} = 1.8$. The results of these simulations are provided in Fig. 2.5.

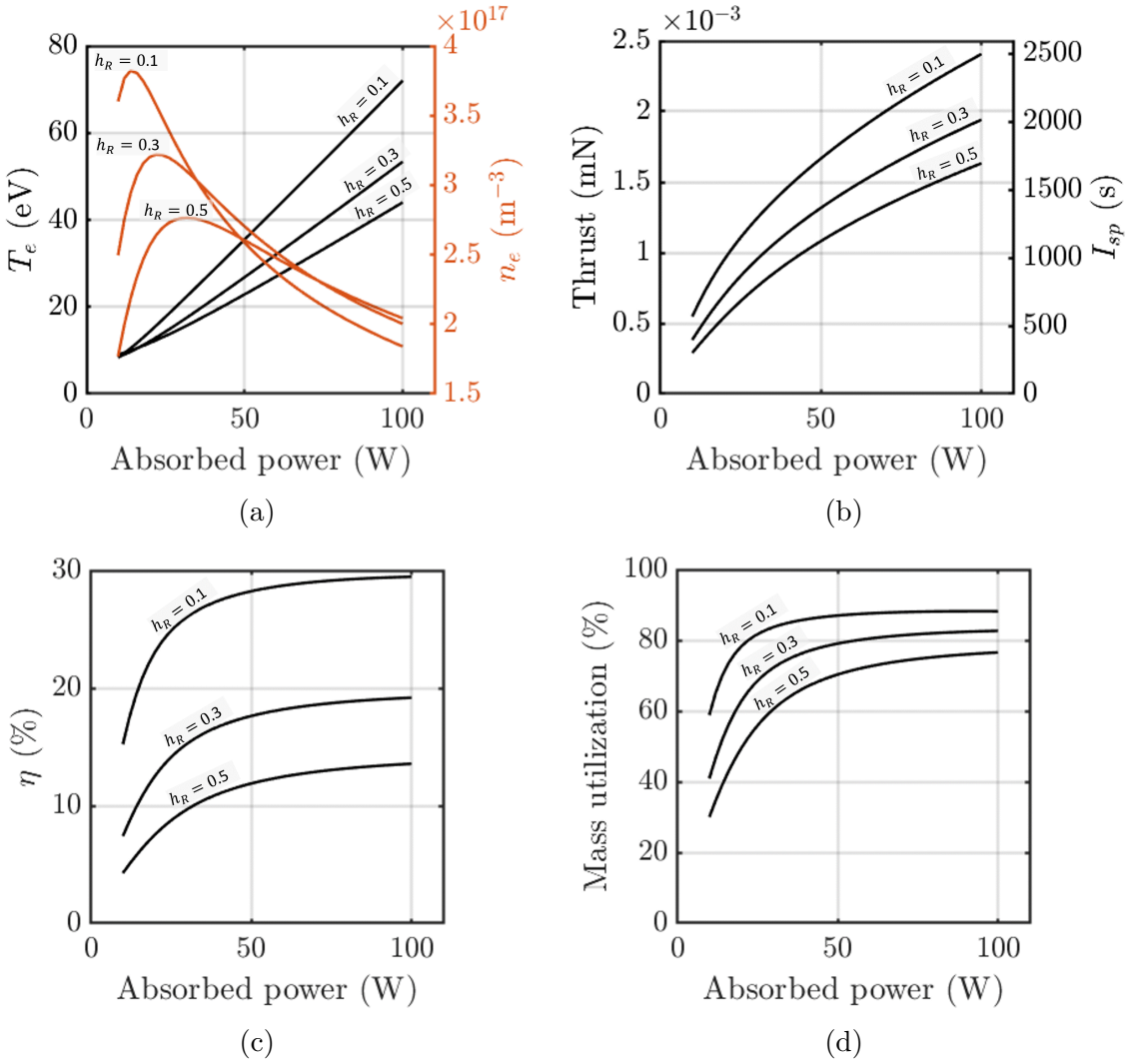

Figure 2.5: (a) Electron temperature and plasma density (orange) (b) specific impulse (c) thrust efficiency, and (d) mass utilization efficiency vs. absorbed power, P_{abs} for 1 sccm xenon flow rate and three radial sheath edge-to-center density ratios, h_R simulating different degrees of plasma confinement.

These plots show that efficiency scales roughly linearly with the inverse of h_R. This is expected as the nominal condition simulation showed that a majority of the absorbed power was lost to the radial walls. It is interesting to note in Fig. 2.5(a) that better plasma confinement leads to higher electron temperatures. Looking at the ion particle balance (Eq. 2.8), this effect is somewhat counter-intuitive. Radial confinement lowers the effective ion loss area, A_{eff}, which, absent other effects, would decrease the required ion generation rate. This, in turn, would decrease the equi-

librium electron temperature. However, for low flow rate operation, another effect dominates the effective loss area decrease. The lower rate of ion recombination at the thruster walls caused by increased plasma confinement leads to fewer neutrals being generated at the walls thus lowering the neutral density within the thruster. This forces the ion generation rate to increase to compensate for the lower neutral density, which forces the electron temperature higher. The net effect is higher electron temperatures as the radial confinement increases. This effect is not seen in high propellant flow rate simulations.

In Fig. 2.6, we again analyze the relative losses from each power sink for the high confinement case ($h_R = 0.1$). The results show that the majority of power is now deposited on the back wall, which, in turn, contributes to thrust generation.

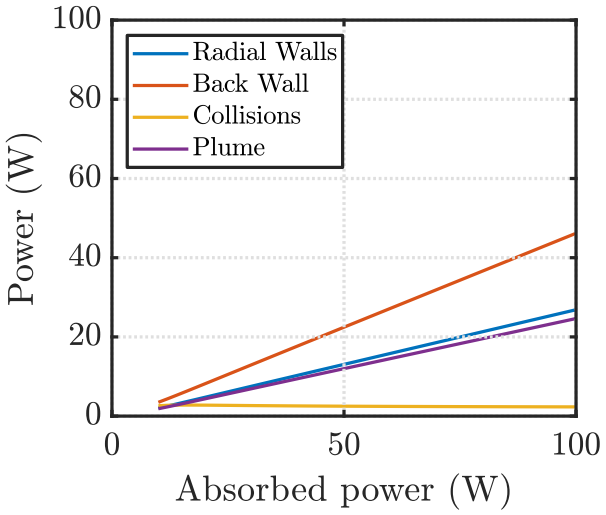

Figure 2.6: Power absorbed by wall losses, collisions, and the thruster plume for $h_R = 0.1$.

2.5.1.2 Detachment Mach Number Sweep

In this section, we simulate the effects of increasing the ion detachment Mach number, which would result from a more efficient magnetic nozzle design. We use the nominal detachment Mach number, $M_{detach} = 1.8$ and twice the nominal Mach

number, $M_{detach} = 3.6$. The radial sheath edge-to-center ratio is held at $h_R = 0.5$. The results are presented in Fig. 2.7. We note that the analogy between traditional adiabatic nozzle theory and the magnetic nozzle model used here breaks down. Here, increased ion mach number causes more heat transfer at the thruster exit plane (the throat), whereas downstream conditions would not effect the throat in an adiabatic nozzle model.

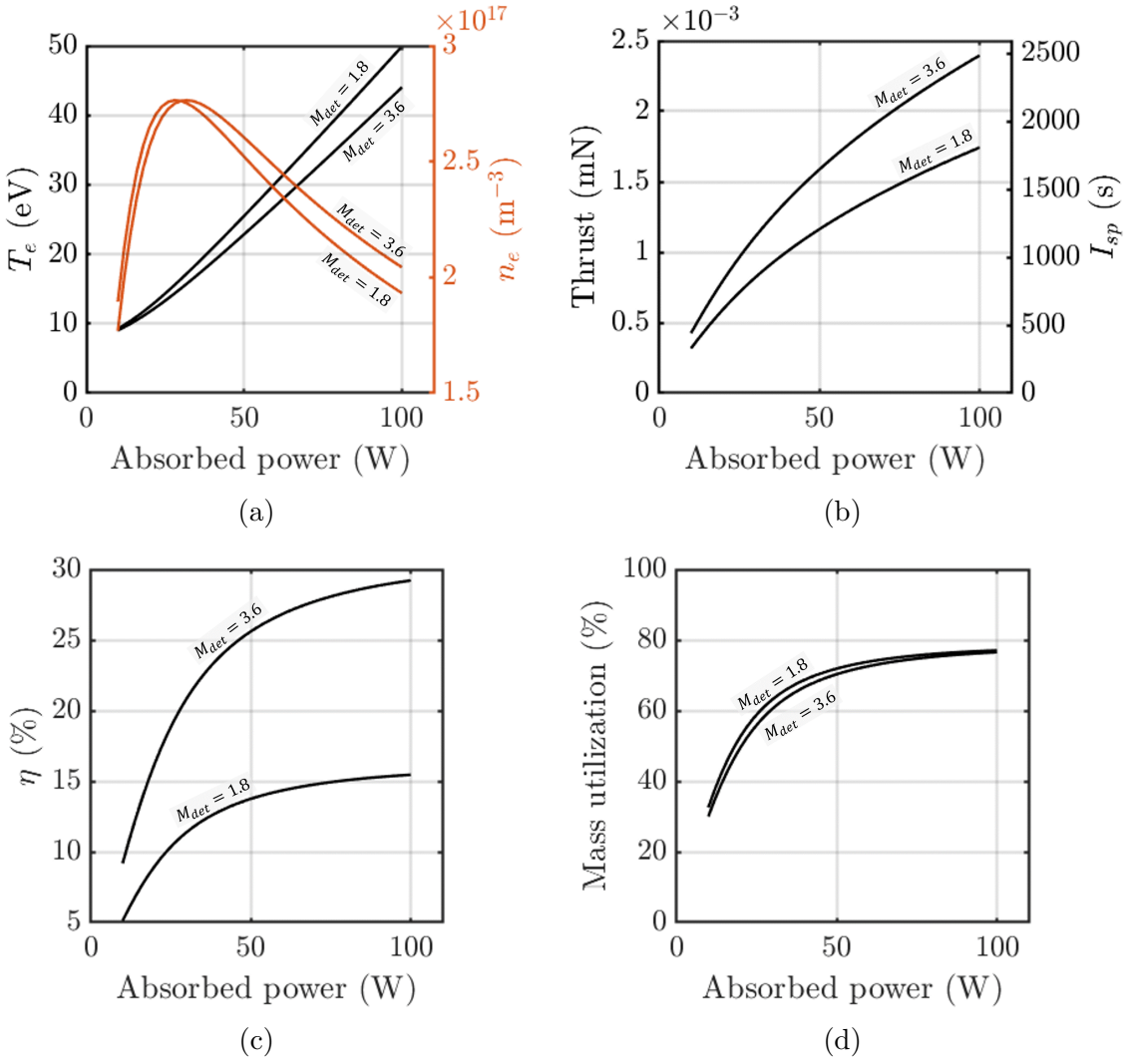

Figure 2.7: (a) Electron temperature and plasma density (orange) (b) specific impulse (c) thrust efficiency, and (d) mass utilization efficiency vs. absorbed power, P_{abs} for 1 sccm xenon flow rate and two M_{detach} simulating different degrees of ion acceleration in the magnetic nozzle.

The results show that increasing Mach number leads to much higher thrust effi-

ciencies as the fraction of total power going into ion acceleration increases. Because total power is held constant, this leads to a lower plasma density, which in turn leads to a slightly lower mass utilization efficiency. This effect is overcome by the greater thrust produced by each ion. Figure 2.8 shows a marked increase in the proportion of power that is directed to the plume for $M_{detach} = 3.6$ versus the nominal case shown in Fig. 2.4.

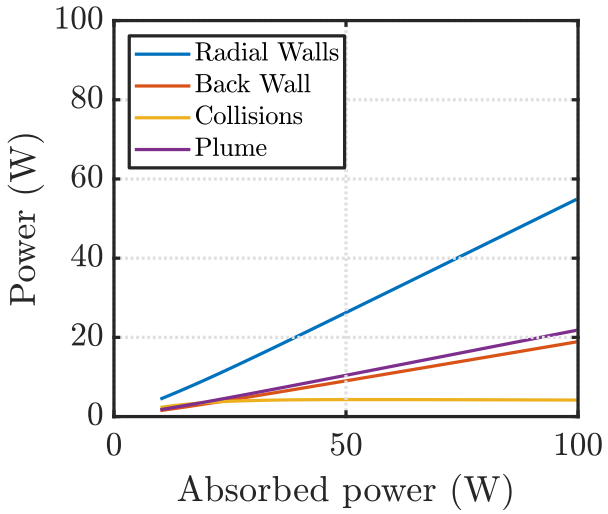

Figure 2.8: Power absorbed by wall losses, collisions, and the thruster plume for $M_{detach} = 3.6$.

2.6 Transient Simulations

In this section, we simulate the transient behavior of the thruster. By including the time-dependent terms in our simulations, we can capture the non-equilibrium conditions that occur during start-up and pulsed operations. We use an explicit Runge-Kutta to solve Eqs. 2.18-2.32 at discrete points in time.

2.6.1 Constant Power

For the simulation shown in the section, we set the absorbed power to 20 W with a flow rate of 1 sccm, as in Sec. 2.5. We seed the simulation with a neutral density

$n_g = 1 \times 10^{19}$ m^{-3}, a plasma density $n_e = 2 \times 10^{16}$ m^{-3}, and an electron temperature $T_e = 0.1$ eV. Lower seed values tend to make the simulations unstable. While varying the initial conditions does change the output of the first few cycles, the pulsed steady state conditions remained unchanged. The absorbed power is ramped to its final value over ~ 0.5 ms, as shown in Fig. 2.9a.

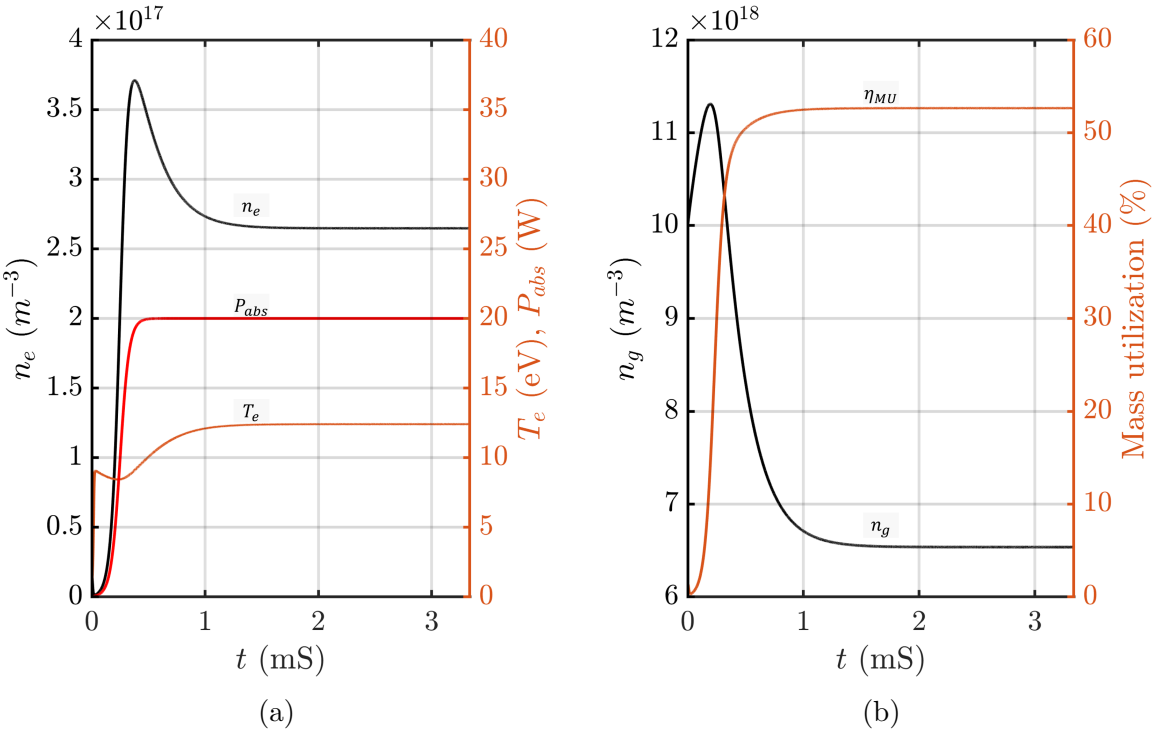

Figure 2.9: Time resolved global model showing (a) absorbed power (red) electron temperature (orange) and electron temperature (black) and (b) neutral density and mass utilization efficiency vs. time for $P_{abs} = 20$ W and 1 sccm xenon flow rate condition.

Averaging the data once the simulation reaches steady state (from $t = 2 - 3$ ms), we can derive the predicted force and efficiency using Eq. 2.33. This calculation yields a predicted thrust of $F = 0.58$ mN with a specific impulse of $I_{sp} = 600$ s and efficiency $\eta = 8.6\%$, in agreement with the results shown in Sec. 2.5.

We briefly comment here on the transient behavior at thruster startup. Figure 2.9 shows that both the neutral and plasma density overshooting their respective steady state values. This occurs as the thruster fills with propellant faster than the neutrals

and ions diffuse through the exit plane. From Eq. 2.8, we can observe that the high neutral density, n_g, leads to a large ion generation rate as $\mathcal{V}(n_e n_g k_{iz}) > n_e u_B A_{eff}$. As the plasma density grows, the ion loss term in the equation surpasses the growth rate, and the plasma density begins to go down. Simultaneously, the total density of ions and neutrals decreases as ions exit the thruster at the Bohm speed. In sum, these effects cause the plasma density to lag behind the neutral density, as seen in Fig. 2.9. Importantly, these simulations show that at start-up, the plasma conditions generated by the thruster can be significantly different than those supported by steady-state operation.

2.6.2 Pulsed Power Simulations

In this section, we use our global model to simulate pulsed operation of the thruster. By continuously pulsing the thruster, we are able to produce electron temperatures and plasma densities that are unsustainable with continuous wave (CW) operation. Using these simulations, we explore the possibility that these transient properties could be beneficial for generating thrust efficiently. The pulsed waveform can be described in term of a duty cycle (D), a pulse period (T), and a maximum and minimum absorbed power ($P_{abs(min)}$ and $P_{abs(max)}$). For our simulations (and experiments), we set a minimum absorbed power, $P_{abs(min)} = 7$ W to ensure steady thruster operation. From the minimum absorbed power and duty cycle, the peak power is calculated using $P_{abs(max)} = P_{abs(min)} + \frac{P_{abs} - P_{abs(min)}}{D}$ with P_{abs} being the average power. We show the output of a pulsed simulation in Fig. 2.10. Here, the pulse period is set to $T = 100$ μS and the duty cycle is $D = 50\%$. The average delivered power is set to $P_{abs} = 20$ W and the flow rate is 1 sccm xenon, as in the previous simulations. We provide a magnified view of a single power cycle in Fig. 2.11.

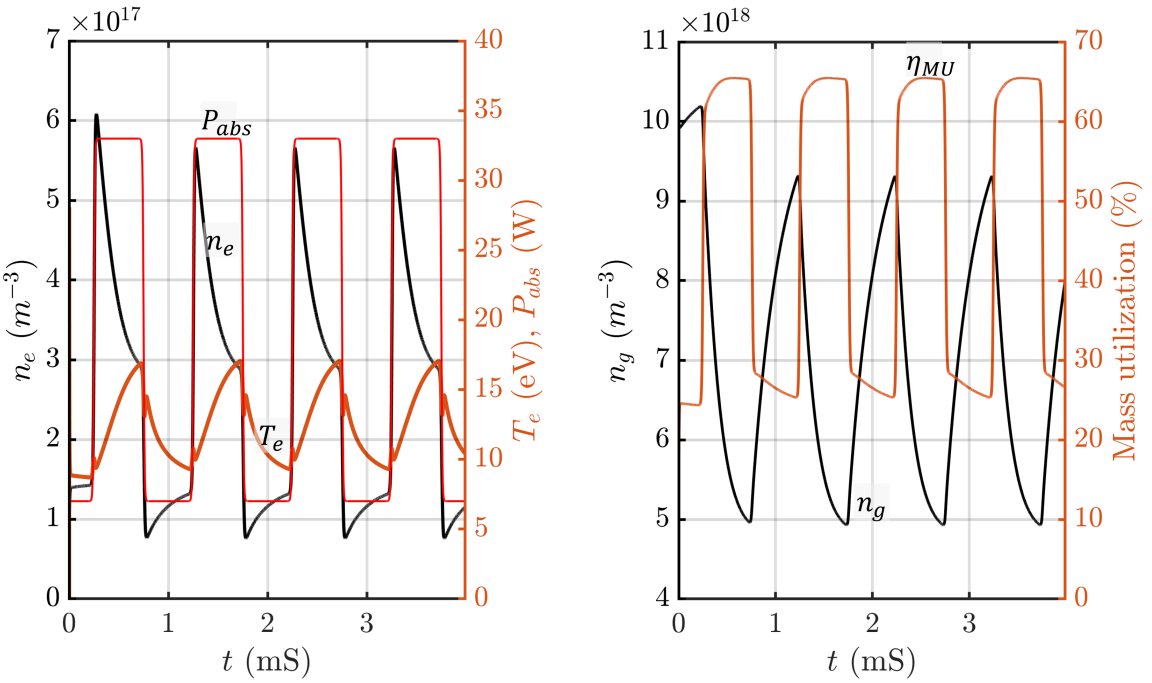

Figure 2.10: Pulsed power time resolved simulation showing (a) absorbed power, P_{abs}, electron temperature, T_e, and plasma density n_e, and (b) neutral density, n_g, and mass utilization efficiency vs. time. The average absorbed power is 20 W with a minimum power of 7 W. The duty cycle is 50% and the flow rate is 1 sccm xenon.

Averaging the pulsed-steady-state values, we find that the $F_{(pulsed)} = 0.58$ mN, $I_{sp(pulsed)} = 604$ s, and $\eta_{(pulsed)} = 8.6\%$. Physically, Fig. 2.11 shows that as power pulses to $P_{abs(max)}$, the ion density quickly increases, simultaneously decreasing the available neutrals in the thruster. By the end of the pulse, the overall density of ions and neutrals is lower than in the steady-state case, which pushes the electron temperature higher. When the power is switched back to $P_{abs(min)}$, the ion density quickly decreases. The spike in T_e seen at the end of the pulse is caused by the depletion of ions and neutrals causing the remaining input power to be absorbed by relatively few electrons. As the thruster begins to fill with neutrals again, the electron temperature relaxes. From this simulation, the performance decreases calculated can be understood by examining the average mass utilization efficiency, η_{MU}. By introducing a pulsed waveform, η_{MU} drops from 52.6% to 50.0%. This results from

neutral propellant leaking out of the thruster during the period when power is at a minimum.

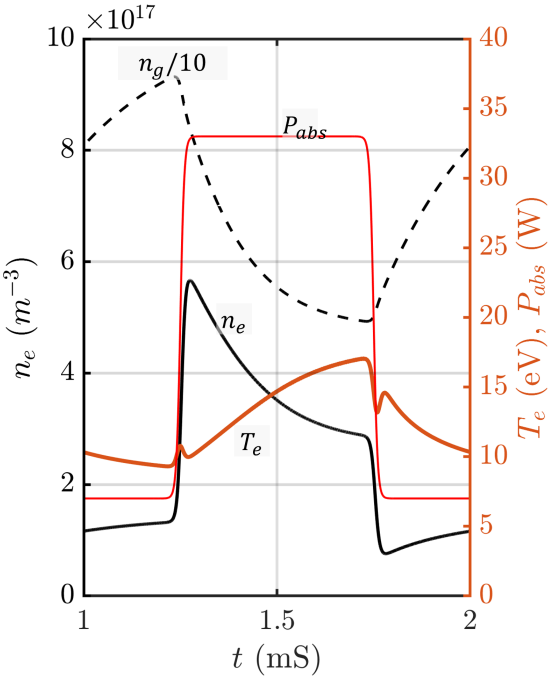

Figure 2.11: Pulsed power time resolved simulation showing a single pulse period.

Using this tool, we can simulate the thruster performance under pulsed power for a range of duty cycles. We show the results of a sweep from 20 to 100% duty cycle for 20 W average power, 1 sccm flow rate with a set pulse period of $T = 100$ μS in Fig. 2.12.

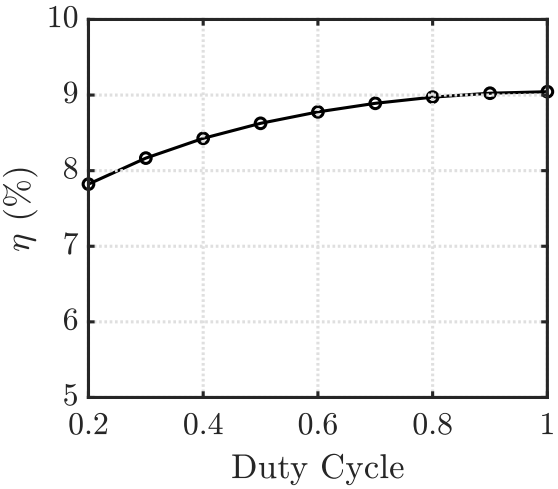

Figure 2.12

The simulations predict that the highest efficiency is reached at continuous operation (without pulsing). Again, the underlying cause is lower mass utilization efficiency that is the result of propellant escaping during low power periods. However, while pulsing the power alone is predicted to waste propellant, we leave unexplored the possibility of pulsing the input gas flow. This strategy in theory could mitigate propellant losses during the pulse off times, but would increase the complexity of the thruster's mass flow control design.

2.7 Summary

In this section, we have provided a zero-dimensional global model of the ECR thruster. We simulated its operation for 1 and 10 sccm xenon flow rates, with input powers ranging from 10 to 100 watts. These simulations generated estimates of neutral density, plasma density, electron temperature, and thruster performance. Using the model, we showed that thruster efficiency could be significantly improved by increasing both the radial plasma confinement and the detachment ion mach number. Finally, by simulating the transient response of the thruster, we predicted that running the thruster in a pulsed power mode is not expected to increase performance.

CHAPTER III

ECR Thruster Testing and Diagnostics

3.1 Introduction

In this chapter, we cover the techniques and nuances involved in the on-ground testing and thrust measurement for microwave-powered magnetic nozzle thrusters. To this end, we first provide the specifications of the ECR thrusters and vacuum facilities used during our experimental campaign. We then discuss the equipment and measurement techniques used in operating the thruster including pressure measurement, propellant flow control, and microwave power generation and diagnostics. We additionally describe the laser-induced fluorescence techniques used for measuring ion velocities during some of our experiments. Finally, we describe the thrust stand used for measuring thrust forces throughout our testing. We include an uncertainty analysis for the pertinent performance metrics i.e. thrust, specific impulse, and efficiency, based on the measured input power, flow rate, and thrust.

3.2 ECR Thrusters Used During Testing

The experiments in this chapter use coaxial based ECR magnetic nozzle thrusters. An overview of their operation is provided in Sec. 1.3.2. We tested two different thruster models for the experimental campaigns. The initial design, designated ECR

Thruster I, was used for the background pressure studies covered in Chapter 4. The final design, designated ECR Thruster II, was used for the thrust measurement and optimization campaigns described in Sec. 3.8 and in Chapter 5. The thrusters share a common design in their overall structure but differ in their magnetic field topology and materials. We provide details on each variant in the following sections.

3.2.1 ECR Thruster I

Figure 3.1 provides a picture and cross-sectional CAD diagram of the ECR Thruster I.

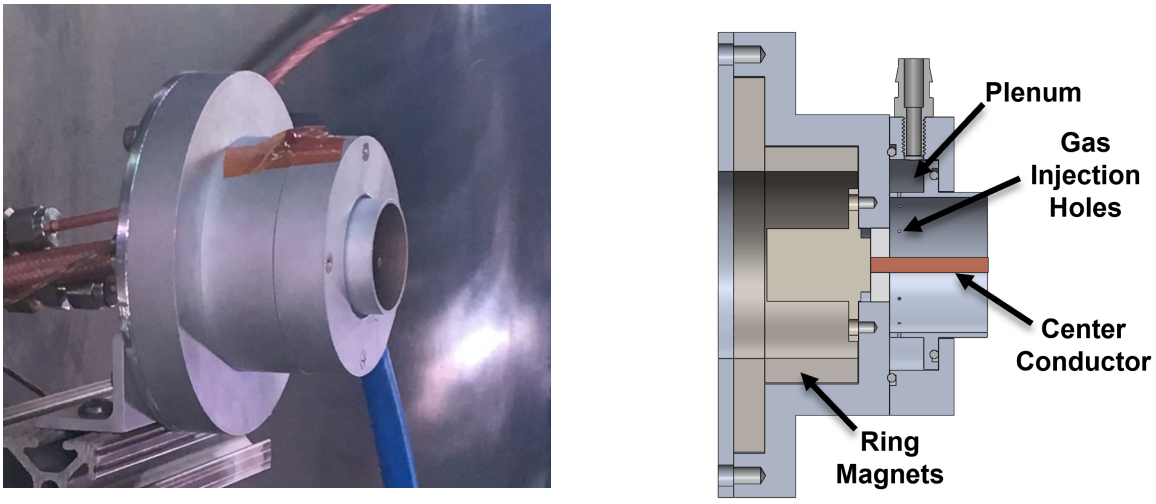

(a) (b)

Figure 3.1: (a) Picture of the ECR I Thruster mounted in the Junior Test Facility, (b) Cross-sectional CAD model of ECR I thruster.

The thruster is constructed using an aluminum 6061 alloy enclosure. The plasma discharge region measures 27.5 mm in diameter by 20 mm in length, similar to the designs found in Ref. [117]. The design features a gas plenum surrounding the plasma discharge region that uses radial injection to provide propellant to the discharge region through 12 0.025 inch (0.635 mm) diameter holes on the side wall. Visual inspection of the resultant plasma showed an even discharge emanating from each of the 12

holes. The center conductor, which is immersed in the plasma, is made of copper brazed to a TNC type RF connector at the back of the thruster. The magnetic field is produced by a set of Neodymium ring magnets (grade N42) positioned behind the discharge region.

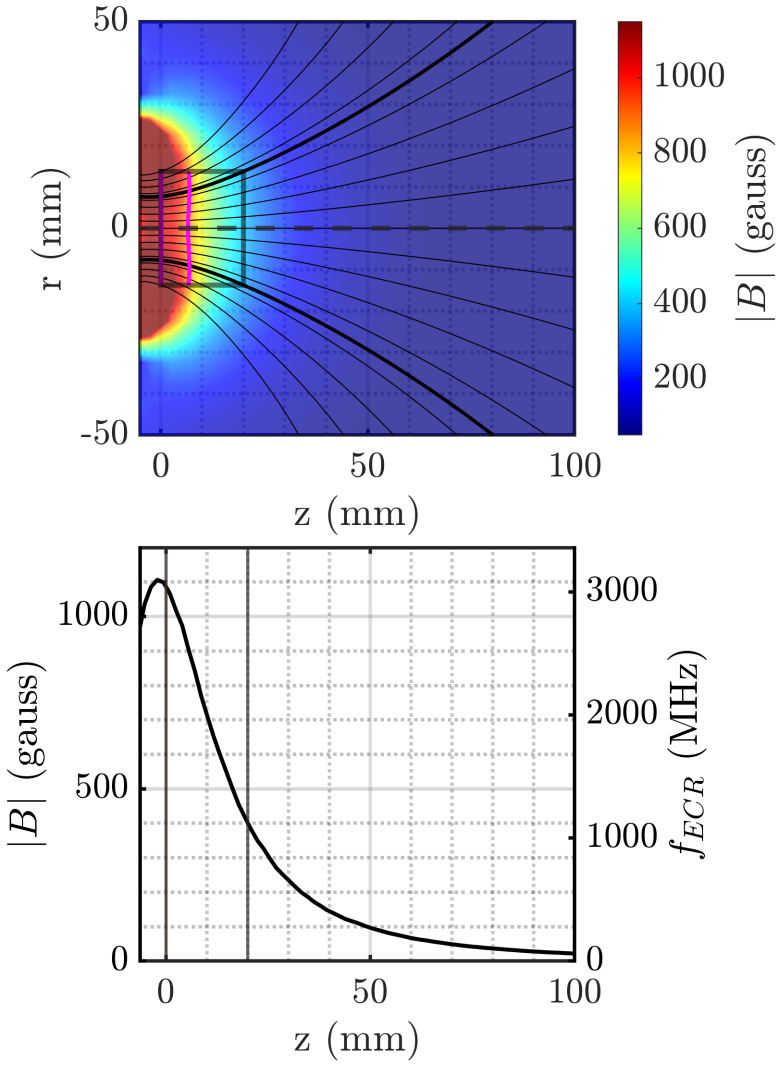

Figure 3.2: Contour plot showing magnetic field strength produced by the ECR I thruster (top). The magenta curve shows the ECR surface corresponding to $f = 2400$ MHz. Center-line magnetic field strength with corresponding ECR frequencies (bottom).

We show the magnetic field topology and center-line field strength for the ECR I

thruster in Fig. 3.2. The electron cyclotron resonance frequency, f_{ECR}, corresponding to the center-line field strength is shown on the right-hand side of the bottom plot. The vertical black lines indicate the back plane of the discharge region and exit plane of the thruster. The magenta curve shown in the top figure provides the resonant surface corresponding to an input frequency $f = 2400$ MHz, which is located ~ 6 mm from the back plane for this thruster design. The bolded magnetic field lines correspond to the field lines that graze the outer edges of the thruster exit. For a fully magnetized plasma, these lines would correspond to the plasma-vacuum interface.

It is worth noting that the maximum operating temperature of the N42 grade neodymium magnets is 80 C. However, some reduction in magnetic field strength will occur even at temperatures below this point. As such, we used water cooling to ensure thruster operation below 40 C for the background pressure studies. This was achieved by wrapping two turns of 1/8 inch copper tube around the magnets. Because of the low input powers (¡ 50 W), this provided more than enough cooling to maintain sub 40 C temperatures when connected to tap water pressures.

3.2.2 ECR Thruster II

Throughout the first experimental campaigns, we identified several drawbacks to the ECR I thruster design. These included melted solder and inconsistent connections to the center conductor, excessive sputtering from the copper used in the center conductor, and the need for active cooling to maintain steady state operation. In light of these design flaws, we redesigned the thruster for the thrust measurement and optimization studies. Figure 3.3 shows a picture and CAD diagram of the redesigned thruster: ECR Thruster II. Like the initial design, the ECR Thruster II features an aluminum 6061 enclosure with a plenum surrounding the plasma discharge region that provides radial gas injection to through 12 holes. The discharge region measures 28 mm in diameter by 20 mm in length. The outer surfaces of the thruster are black

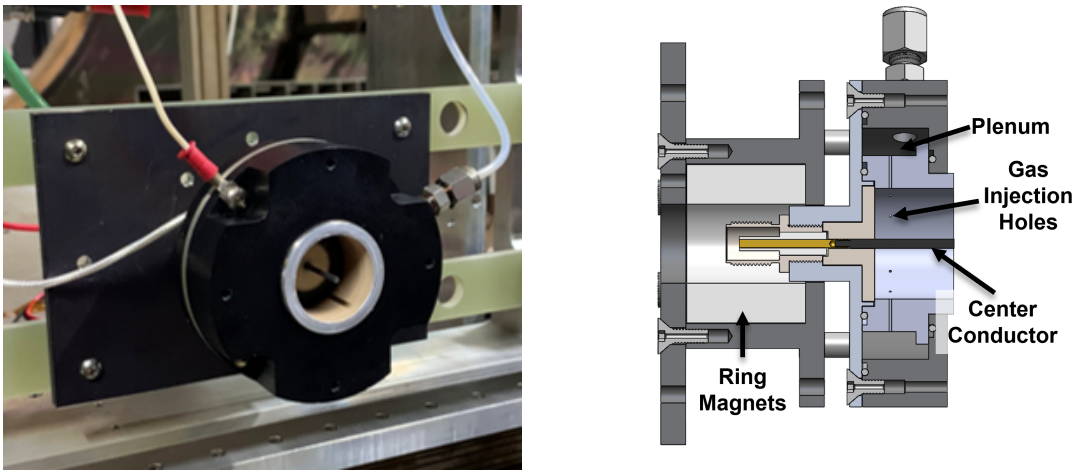

(a) (b)

Figure 3.3: (a) Picture of the ECR II Thruster mounted on the thrust stand, (b) Cross-sectional model of the ECR II thruster.

anodized to improve radiative heat rejection. The center conductor is made of a 3/32" graphite rod. One end is threaded into a TNC connector at the back end of the thruster, similar to those designs found in Ref. [92]. Graphite provides lower sputter yields in plasma environments compared to copper at the cost of a higher electrical resistivity. Although this material potentially decreases thruster efficiency, it enables longer lifetimes and more consistent performance throughout tests. Because of the complex interaction between the input microwaves and the plasma, it is difficult to determine how much power is lost to ohmic heating of the antenna. However, tests conducted with the graphite antenna did not yield measurably lower performances than the more conductive antenna materials.

The magnetic field is produced by a set of samarium cobalt magnets (grade YXG28H) positioned behind the discharge region. These magnets have a 350C operating temperature, which eliminates most thermal concerns for the thruster. We show the magnetic field topology for ECR Thruster II in Fig. 3.4 with the center-line magnetic field strength plotted in Fig. 3.4. The magenta line in Fig. 3.2(a) corresponds

to the resonant surface for $f = 2400$ MHz located $\sim$ 1mm from the back plane of the discharge region. Figure 3.4 shows that within the discharge region, the possible frequencies for ECR excitation range from $f \approx 2420$ to $f \approx 900$ MHz. Compared to the ECR I design, the resonant zones are closer to the back plane of the thruster for equal input frequencies, and the magnetic field gradient along the thruster axis is more gradual. We explore the optimal position of the resonance zone in Chap. V.

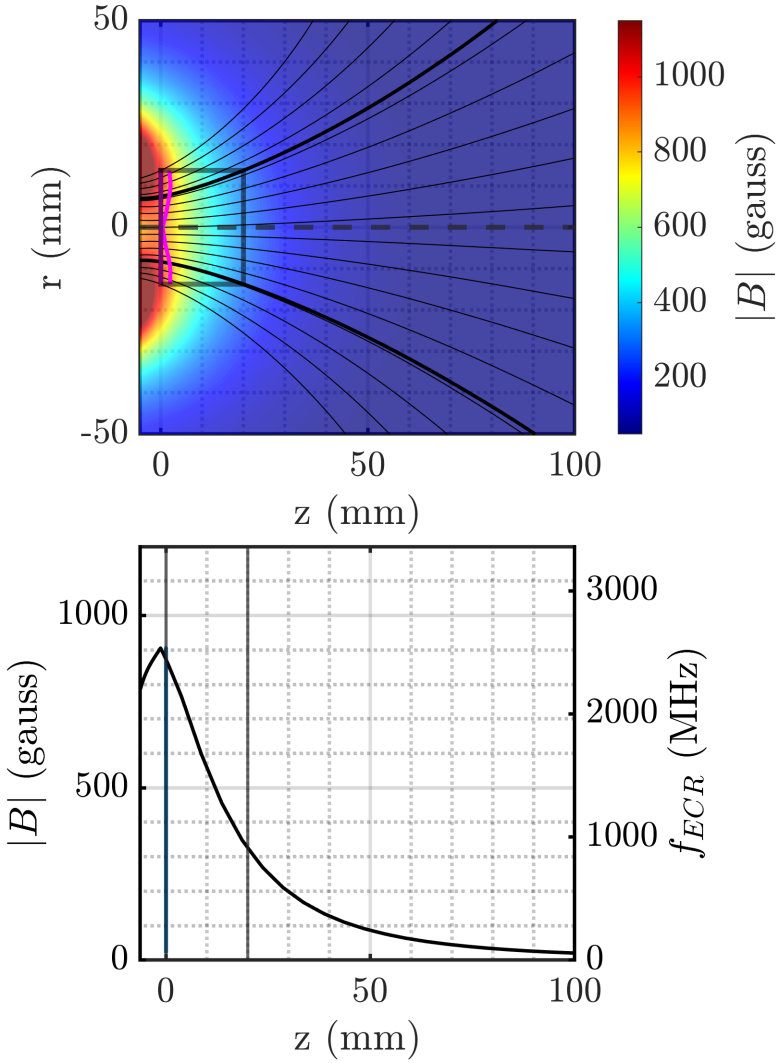

Figure 3.4: Contour plot showing magnetic field strength produced by the ECR II thruster (top). The magenta curve shows the ECR surface corresponding to $f = 2400$ MHz. Center-line magnetic field strength with corresponding ECR frequencies on the right (bottom). The antenna tip is located at the exit plane of the thruster.

3.3 Vacuum Facility

The experiments presented in this chapter and Chapter 5 were conducted in the Junior Test Facility at the University of Michigan's Plasmadynamics and Electric Propulsion Laboratory, shown in Fig. 3.5a. This vacuum facility is a cylindrical stainless steel clad chamber measuring 1 meter in diameter by 3 meters in length. It is equipped with two high-vacuum pumps: a turbomolecular pump (Leybold Mag 2000) rated for 1550 liters/s on N_2 ($\sim$ 1240 liters/s on Xe), and a cryogenic plate capable of pumping roughly 38500 liters/s on xenon. The cryogenic pump maintained a temperature of $\sim$ 30 K throughout testing. The actual pumping speed observed during the experimental campaigns ranged from approximately 19000 to 30000 liters/s xenon. We show a typical pressure versus flow rate measurement in Fig. 3.5b. The discrepancy between predicted and measured pumping speeds was likely caused by partial blockages of the cryogenic pumping surface during thruster testing. The base pressures were below 10^{-7} Torr-N_2 throughout the duration of the tests. More details on the test facility and pumps are provided in Ref. [119].

3.4 Pressure Measurements

We measured chamber pressure using a Stabil Series 370 Ion Gauge (calibrated for nitrogen) mounted along the side of the chamber, in plane with the thruster. The low pressures involved in this experiment necessitate taking into account the finite base pressure when correcting the readings for xenon. Pressures reported in this experiment were therefore calculated using

$$P_{corrected} = \frac{P_{measured} - P_{base}}{2.87} + P_{base}, \tag{3.1}$$

where 2.87 is the correction factor from nitrogen to xenon. Here, we assume that the base pressure consists of mostly nitrogen gas.

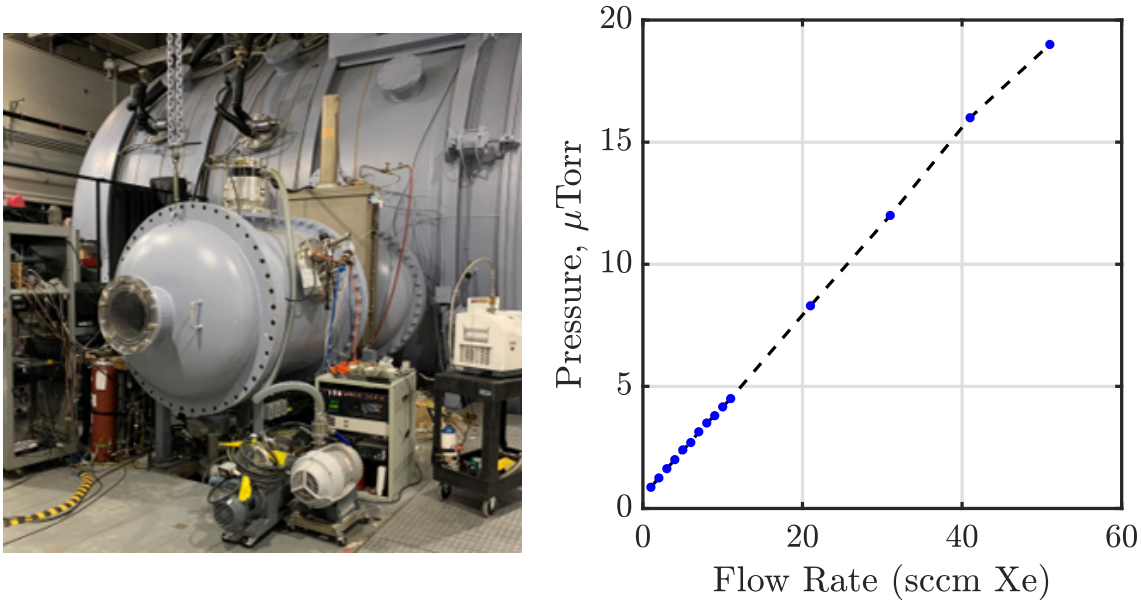

(a) (b)

Figure 3.5: (a) Junior Test Facility at the University of Michigan, (b) chamber pressure vs. xenon flow rate with both the turbomolecular and cryogenic pumps in operation.

3.5 Propellant flow control

The experiments presented here used xenon propellant with flow rates ranging from 0.75 to 10 sccm (6.71×10^{-7} - 8.95×10^{-7} Kg/s). The flow control setup, shown in Fig. 3.6, uses an Alicat MCV-10SCCM-D/5M mass flow controller to both set and monitor propellant flow rate. A second flow controller was used to inject excess propellant in order to control the chamber background pressure during some experiments.

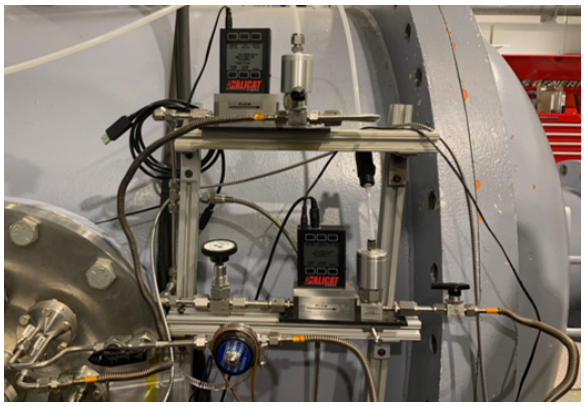

Figure 3.6: Flow control setup showing flow controller and solenoid valve.

We calibrated the MCV-10SCCM-D/5M flow controller using a MesaLabs Definer 220 DryCal system. Our in-house calibrations demonstrated a mass flow accuracy within a range of +/– 5%. The setup additionally features a solenoid valve used for flooding the thruster with propellant on startup.

3.6 Microwave Generation and Diagnostic Techniques

In this section, we provide an overview of the microwave generation and diagnostic techniques used in our experiments. Accurate power measurements are a vital facet of thruster testing needed for assessing thruster efficiency and spacecraft requirements. However, microwave power diagnostics present much more complexity compared to their DC counterparts, stemming from the difficulty in directly measuring voltage and current without perturbing the system. We begin this section with a description of the equipment used in testing. We then detail the subtleties of the microwave signal paths and examine the sources of uncertainty inherent to our diagnostic techniques.

3.6.1 Microwave Test Equipment Used in Experiments

Figure 3.7a shows a schematic diagram of the microwave equipment used in the experiments. The setup uses a computer controlled dual-output microwave signal source (WindFreak Synth HD Pro) to generate the initial low-power microwave sig-

nals. The signals used in our experiments include single-frequency, two-frequency, and pulsed wave-forms. The Synth HD Pro is capable of generating frequencies ranging from 10 MHz-20 GHz with output powers ranging from -40 to 15 dBm. The output signal can be pulsed at a maximum frequency of 250 KHz. The signal generator's outputs are combined (in the case of two frequency heating) using a 3 dB combiner. The final low-power signal feeds into to a solid-state power amplifier (Comtech PST ARD88258-50). The amplifier outputs the high-power microwave signal used to power the thruster. The maximum output power is $\sim$50 W. The operational bandwidth of the amplifier spans 800-2500 MHz, making it the limiting component in selecting output frequencies.

The high power microwave signal is fed through a coaxial cable to a series of two 20 dB bi-directional couplers (Mini-Circuits ZGBDC20-372HP+). The forward coupled port of the first directional coupler is connected to a spectrum analyzer (HP 8563E) to verify the frequency of the output signals. The second coupler is connected to two thermocouple-based power sensors (Keysight N8482H) used to measure forward and reverse power to the thruster. It is important to note here that while diode-based power sensors can provide faster measurements, they typically cannot accurately measure mixed-frequency signals. The directional coupler attaches directly to a vacuum feedthrough. On the vacuum side of the feedthrough, a coaxial cable attaches to either a DC block or, in the case of direct thrust measurements, a wireless coupler, which then connects to the thruster. The setup uses LMR-400 cables for transmitting the high-power microwave signal. In vacuum, we use TNC connectors for all high-power connections. These connectors were selected because of their relatively high power ratings and lack of internal air-gaps. The air-gaps in RF connections, such as N-type connectors, can slowly depressurize and allow micro-discharges to form when under vacuum. This, in turn, causes undesirable power consumption and connector damage.

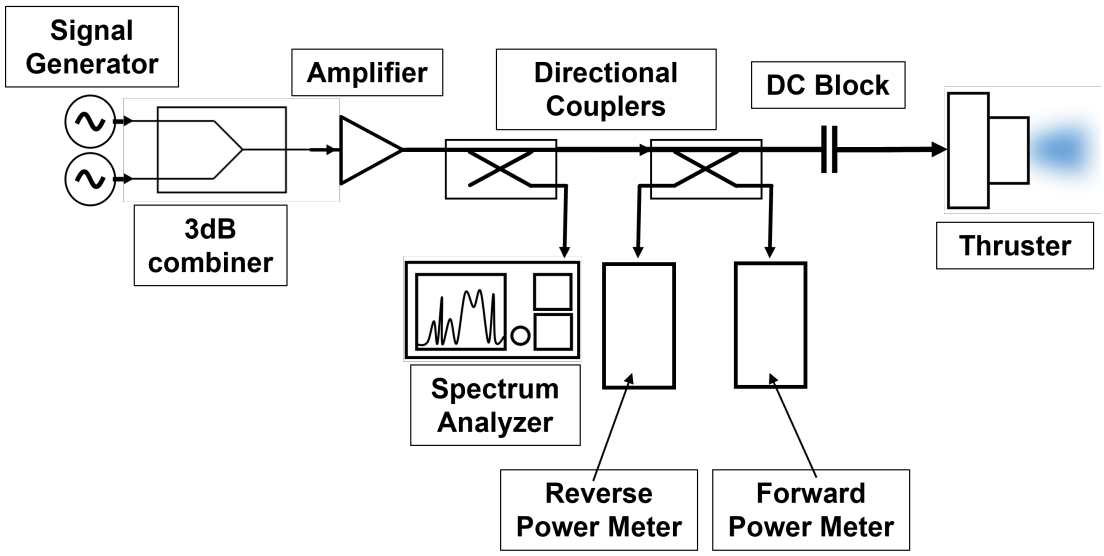

(a)

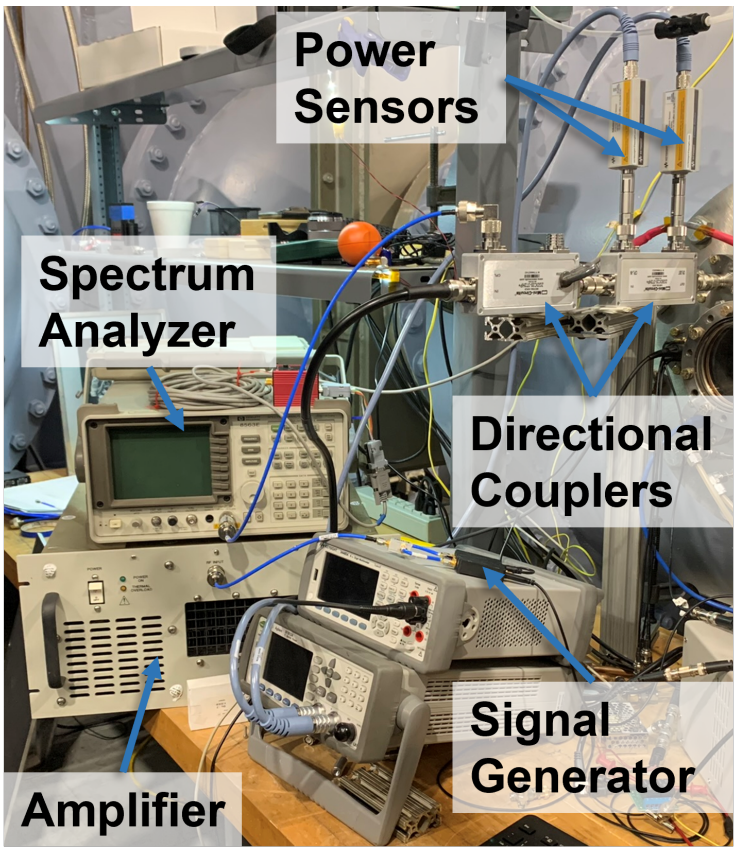

(b)

Figure 3.7: (a) Schematic of microwave power injection, (b) picture of microwave equipment setup used in the experimental campaigns.

3.6.2 Microwave Power Measurements and Uncertainty

In this section, we detail the components used in measuring microwave power delivered to the thruster and describe the sources of uncertainty inherent to these diagnostics.

3.6.2.1 Microwave Power Sensors

Generally speaking, microwave power sensors fall into three categories: thermistor, thermocouple, and diode detectors. Thermistor and thermocouple sensors measure the heat generated by an incoming microwave signal. Diode detectors rectify the input signal and measure the resulting DC voltage. Typically diode sensors have faster response times allowing them to measure time-resolved waveforms, while thermal-based sensors can achieve higher accuracy for average power measurements. Additionally, thermal sensors are less prone to error when measuring mixed signals such as the two-frequency waveforms used in some of the experiments performed in Chapter 5.

The measurement uncertainty in these sensors stems from non-linearities in the power and frequency response, zero-drift, instrument noise, and mismatch uncertainty [2]. The sensor's power deviation, frequency response, and noise parameters are typically provided by the datasheet. The zero-drift can be corrected by periodically taking zero-power measurements. The mismatch uncertainty, however, depends on the consistency of the connections, and cannot easily be determined a priori. This uncertainty can be minimized by using the fewest number of adapters possible and by ensuring that connectors are tightened to the appropriate torque specifications.

The power sensor used in our experiments, the Keysight N8482H, uses a thermocouple-based design. It features a highly linear power response with a $\sim 1\%$ deviation over the powers measured and a $\sim 1\%$ variation in calibration factor over the frequency range used our experiments. The N8482H has a low SWR ensuring minimal mismatch uncertainty. In total, we estimate the error due to the power sensor, ΔP_{sens}, to be

under 3% for our experimental setup.

3.6.2.2 Microwave Signal Path used in ECR Experiment

Figure 3.8 shows the microwave power flow from the directional coupler to the thruster. We cover more details on the directional coupler and power sensors in the following sections. The signal path can be understood as follows: Forward power from the amplifier (P_1) enters the directional coupler at port 1, as shown by the blue signal path in Fig. 3.8. Within the coupler, a small fraction of the forward, given by the coupling factor (K), is diverted to port 3 where it is measured by a microwave power meter. The remaining forward power exits the coupler at port 2 and is transmitted via a series of feedthroughs and coaxial cables to the thruster. When measuring thrust, the signal path also includes a wireless power coupler, as described in Sec. 3.8.2.8. The cables, connectors, and wireless power coupler absorb a fraction of the incident power, given by an attenuation constant (α_T). The power incident to the thruster (P^T_{Fwd}) is then partially absorbed by the thruster. Because of mismatch between the cable and thruster, a portion of this incident power (P^T_{Refl}) is reflected, as shown by the red signal path in Fig. 3.8. This reflected power is again attenuated by the cables and wireless power coupler and enters the directional coupler at port 2. Within the coupler, a fraction of the reflected power (K) is diverted to port 4, and the remaining power is absorbed by the amplifier. As an aside, we note that an alternative setup could use a circulator to divert the reflected power away from the amplifier. However, the solid-state amplifier used in our setup had internal protection circuitry that enabled operation without an external circulator.

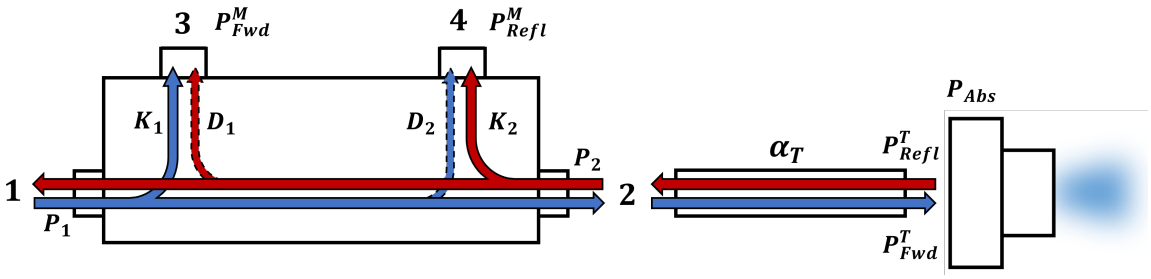

Figure 3.8: Signal flow from the directional coupler to the thruster. K_1 and K_2 show the coupled signal paths. D_1 and D_2 show the signal leakage caused by finite directivity. α_T represents the signal attenuation in the cable. P^T_{Fwd} and P^T_{Refl} 0are the powers incident to and reflected by the thruster. P^M_{Fwd} and P^M_{Refl} are the forward and reflected powers measured at the directional coupler.

3.6.2.3 Directional Coupler Signal Measurements

In the previous sections, we introduced a simplified explanation of directional couplers as used microwave power measurements. In this section, we provide a more detailed overview of their operation, and in the next section we expand upon a critical source of uncertainty in these devices, directivity error.

Directional couplers are passive devices that tap a percentage of the input forward and reflected powers and redirect the signals to the coupled ports. As shown by the signal paths in Fig. 3.8, a fraction of the microwave power entering port 1, K_1 is coupled to port 3. Similarly, a fraction of the reflected power entering port 2, K_2 is coupled to port 4. These forward and reflected coupling factors are defined in decibels as

$$K_1 = 10 \log \left(\frac{P_1}{P_3} \right), \tag{3.2}$$

$$K_2 = 10 \log \left(\frac{P_2}{P_4} \right), \tag{3.3}$$

where P_1 is the power incident to port 1, P_2 is the power incident to port 2, and P_3 and P_4 are the fractional powers coupled to port 3 and port 4, respectively. Typically $K_1 = K_2$, with $K_1 = K_2 \equiv K \approx 20.5$ dB in the coupler model used in our experiments.

In an ideal directional coupler, the coupled port would be entirely isolated from all other ports i.e. port 3 would not be affected by the signals entering ports 2 and 4, and port 4 would not be affected the signals entering ports 1 and 3 in the coupler shown in Fig. 3.8. In practical coupler designs, there is finite isolation between ports. A small fraction of the power incident to port 1 leaks into port 4; likewise, a fraction of the power incident to port 2 leaks into port 3. We show these undesired signal paths in dashed lines in Fig. 3.8. The effect of this finite isolation is typically characterized by the coupler's directivity, D, a metric describing the ratio of desired to undesired coupling given in decibels as

$$D_1 = 10 \log \left(\frac{P_3}{P_4} \right) \tag{3.4}$$

$$D_2 = 10 \log \left(\frac{P_4}{P_3} \right). \tag{3.5}$$

The coupler model used in our experiments has a directivity of $D_1 = D_2 \equiv D = 23$ dB, meaning that $\sim 0.05\%$ of the power directed from port 1 to port 3 will leak into port 4.

3.6.2.4 Control of Delivered Microwave Power

Typically, we use the power absorbed by the thruster, P_{Abs}, to determine thruster efficiency. For more practical spacecraft and mission design, the total efficiency would include the DC power going from the satellite bus to the DC to microwave power converter, which would in turn power the thruster. The power reflected by the thruster could be returned to the thruster using a matching network. However, for the purposes of our experiments, we do not make use of such a network and instead focus on optimizing the thruster itself.

Using the definitions shown in Fig. 3.8, the power deposited to the thruster can

be defined as

$$P_{Abs} = P^T_{Fwd} - P^T_{Refl}. \tag{3.6}$$

The relationship between the incident and reflected powers is typically described using a signal reflection coefficient, Γ, where

$$P^T_{Refl} = |\Gamma|^2 P^T_{Fwd}. \tag{3.7}$$

We note here that the reflected signal is again attenuated by a fraction, α_T, as it travels back to the directional coupler. Neglecting errors caused by the directional coupler and power sensors (discussed below), we can relate the forward and reflected powers deposited at the thruster to those measured at the directional coupler as

$$P^T_{Fwd} = \frac{\alpha_T P^M_{Fwd}}{K}, \tag{3.8}$$

$$P^T_{Refl} = \frac{P^M_{Refl}}{\alpha_T K}, \tag{3.9}$$

where P^M_{Fwd} is the power measured at port 3, P^M_{Refl} is the power measured at port 4. These are the relations used when setting the power absorbed by the thruster during experiments.

Combining Eqs. 3.6-3.9, we can calculate the expected measured forward and reflected powers as a function of the reflection coefficient for a set absorbed power for given attenuation and coupling parameters as

$$P^M_{Fwd} = \frac{K}{\alpha_T(1 - |\Gamma|^2)} P_{Abs}, \tag{3.10}$$

$$P^M_{Refl} = \frac{K\alpha_T}{(1/|\Gamma|^2) - 1} P_{Abs}. \tag{3.11}$$

We show the predicted measured powers for a constant absorbed power in Fig. 3.9 for reflection coefficients ranging from 0 to 50%. For demonstration purposes, we

have set the attenuation and coupling coefficient to $\alpha_T = 1$ and $K = 1$.

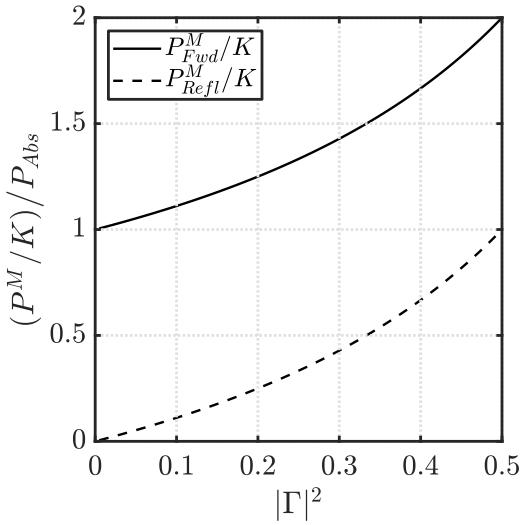

Figure 3.9: Example calculation of the predicted measured and reflected powers for a fixed absorbed power vs. reflection coefficient for a lossless transmission line ($\alpha_T = 1$) and neglecting directivity errors.

3.6.2.5 Directivity Errors

The finite isolation between ports in a directional coupler results in so-called directivity errors that can add significant uncertainty to power measurements at the coupled ports. Because the signal arriving at the coupled ports is a vector summation of two waves—the coupled (desired) signal and the leaked (undesired) signal—the resulting signal amplitude depends on the phase relationship of the two forward and reflected powers. For the thruster experiments, the phase relationship is a function of frequency, cable length, and plasma properties. As such, it cannot be easily calculated prior to conducting the experiments and must be treated as an unknown when assessing power delivered to the thruster.

Using the definitions of coupling coefficient and directivity provided in the previous section, we can relate the power measured by the power sensors to forward power incident to the coupler at port 1 (P_1) and the reverse power incident to the coupler

at port 2 (P_2) as follows:

$$P^M_{Fwd} = P_1 K + P_2 K D + 2K\sqrt{P_1 P_2 D}\cos\phi_1, \tag{3.12}$$

$$P^M_{Refl} = P_2 K + P_1 K D + 2K\sqrt{P_2 P_1 D}\cos\phi_2, \tag{3.13}$$

where ϕ_1 is the relative phase of the forward and reflected signals entering port 3 and ϕ_2 is the relative phase of the forward and reflected signals entering port 4. This formulation does not include the power losses incurred inside the coupler.

We relate the powers entering the directional coupler to the power delivered to the thruster with $P_1 = P^T_{Fwd}/\alpha_T$ and $P_2 = P^T_{Refl}\alpha_T$. Using these relations, we can express Eqs. 3.12-3.13 in terms of the power incident to the thruster, P^T_{Fwd}, the power reflected by the thruster, P^T_{Refl}, and relative phases of the forward and reflected powers at the directional coupler, ϕ_1 and ϕ_2, and the directional coupler parameters, K and D, as

$$P^M_{Fwd} = \frac{P^T_{Fwd}}{\alpha_T} K + P^T_{Refl}\alpha_T K D + 2K\sqrt{P^T_{Fwd} P^T_{Refl} D}\cos\phi_1, \tag{3.14}$$

$$P^M_{Refl} = P^T_{Refl}\alpha_T K + \frac{P^T_{Fwd}}{\alpha_T} K D + 2K\sqrt{P^T_{Refl} P^T_{Fwd} D}\cos\phi_2. \tag{3.15}$$

Using Eqs. 3.14-3.15, we can calculate the phase dependence of the measured forward and reflected powers for a constant reflection coefficient and true forward power to the thruster.

We denote error caused by finite directivity effects on the forward and reflected power measurements as ΔP^M_{Fwd} and ΔP^M_{Refl}. Figure 3.10 shows ΔP^M_{Fwd} and ΔP^M_{Refl} normalized by the ideal measured powers given in Eqs. 3.10 and 3.11 as a function of relative phase for two different reflection coefficients, $|\Gamma|^2 = 0.5$ and $|\Gamma|^2 = 0.1$. Here we have set $\alpha = 1$ and $K = 1$ for demonstration purposes. These plots show that, even with ideal power sensors, substantial errors can arise from finite directivity.

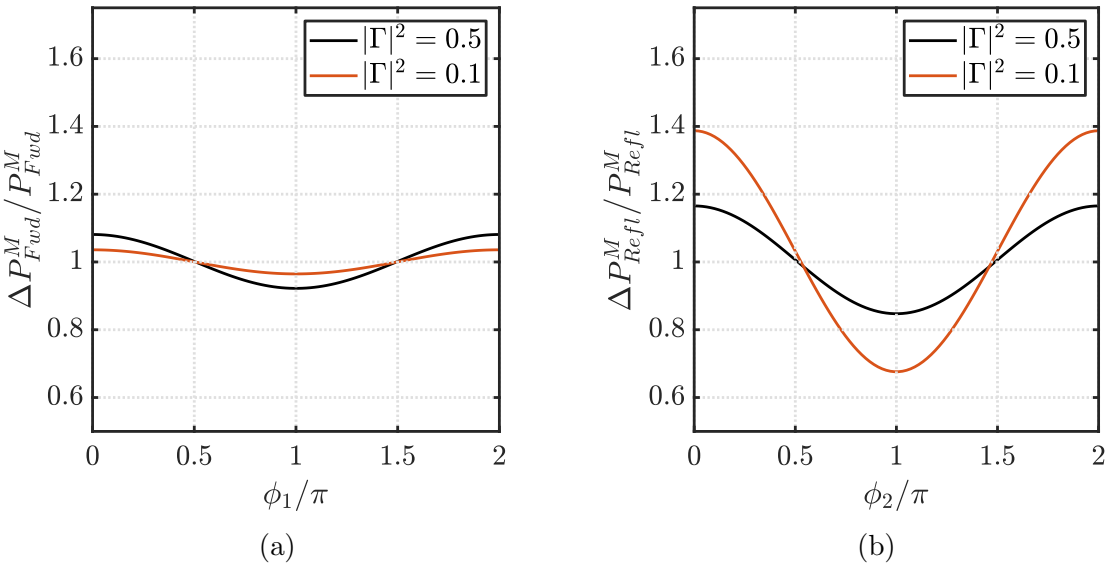

Figure 3.10: (a) Example of the calculated measured forward power (P^M_{Fwd}) and (b) calculated measured reflected power (P^M_{Refl}) as a function of reflected signal phase (ϕ) for a constant incident power and reflection coefficients $|\Gamma|^2 = 0.5$ (black line) and $|\Gamma|^2 = 0.1$ (orange line). The directivity is 23 dB for the calculations.

Taking the worst case scenario with ϕ_1 180° out of phase with ϕ_2, we can calculate a range of the possible measured forward and reflected powers compared to the true forward and reflected powers as a function of the reflection coefficient. We show in Fig. 3.11 the upper and lower bounds for the forward and reflected powers normalized by the ideal values given in Eqs. 3.10 and 3.11. These plots demonstrate that the forward power measurements tend to become less accurate as the reflection coefficient increases, though the overall error is less than 10% for reflection coefficients under 50% (typically the maximum seen in our experiments). The reflected power measurements, on the other hand, decrease in accuracy for small reflected powers. This effects stems from the reflected power being on the order of the power leaked from the forward power to the reflected power measurement port.

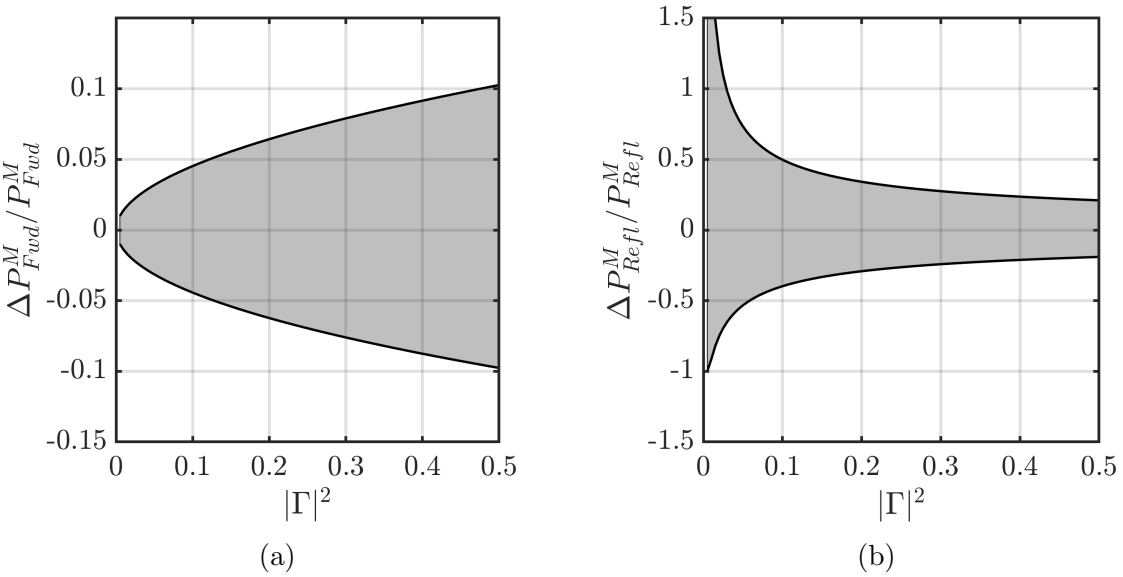

Figure 3.11: Range of uncertainty caused by directivity errors normalized by the measured power predicted by Eqs. 3.10-3.10 as a function of reflection coefficient for (a) forward power (b) reflected power.

The salient metric for characterizing the thruster performance in our experimental campaign is the power absorbed by the thruster, P_{Abs}. Combining Eqs. 3.6-3.15, we can derive the range of true absorbed powers for a set of measured forward and reflected powers. We show the results of these calculations in Fig. 3.12a for a fixed measured forward power. Using Eqs. 3.10 and 3.11, we can further predict the range of true absorbed powers for a constant measured absorbed power, as shown in Fig. 3.12b. The x-axis in these graphs is the measured reflection coefficient, which may differ from the true reflection coefficient used in the previous plots. We denote the uncertainty arising from directivity errors ΔP_{dir}. We note that, in contrast to measurement error caused by noisy signals, we cannot presuppose a distribution function for the directivity error. Furthermore, the relative uncertainty in absorbed power is not constant but instead a non-trivial function of the thruster's reflection coefficient. Therefore, test points with the same value of measured absorbed power, but different measured reflected powers, can have vastly different uncertainties in their absorbed power and thus thrust efficiency.

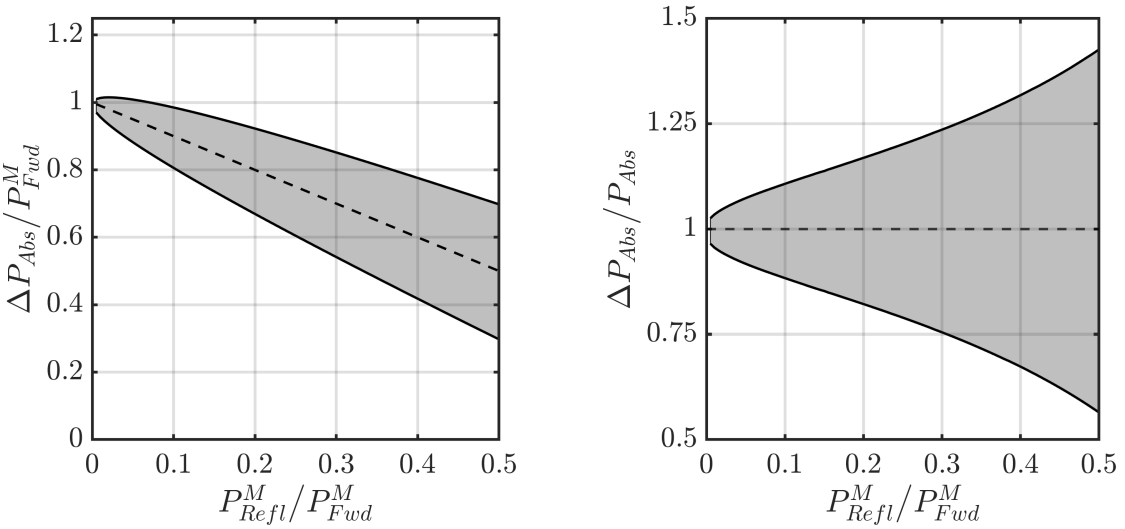

Figure 3.12: (a) Range of true absorbed power for a fixed measured forward power and (b) fixed measured absorbed power. The ratio of measured reflection coefficient is swept from 0 to 50%. The directivity of the simulated directional coupler is 23 dB and the transmission and coupling coefficients are set to 1. The uncertainty in absorbed power increases significantly with reflection coefficient.

3.6.3 Transmission Losses and Coupling Coefficient

We measure the directional coupler's coupling coefficient K and the system's attenuation constant, α_T, prior to conducting any experiments. These properties are frequency dependent and we therefore sweep measurements over the operating frequency range of the tests.

We determine the coupling coefficient by attaching power sensors to the coupler's transmitted and coupled ports (ports 2 and 3 in Fig. 3.8) and a matched load to the isolated port (port 4). A low power signal is then applied to the input port (port 1) and the coupling coefficient can then be measured from the difference in powers measured at the transmitted and coupled ports. We show the results of this test in Fig. 3.13.

The attenuation constant can be measured by attaching a power sensor in place of the thruster. With this setup, we can relate the power measured at the coupler to

the power delivered to the thruster using

$$\alpha_T \approx \frac{P_{Fwd}^T}{P_{Fwd}^M K_1}, \tag{3.16}$$

where K is the frequency-dependent value measured in Fig. 3.13. Here, we have ignored the reflected power contribution, which should be small for a well matched load such as the power meter. We show the measured attenuation values as a function of input frequency in Fig. 3.13b. From this plot, we see an overall trend of higher losses (lower α) with increased frequency. This is expected as attenuation in cables and the wireless power coupler (see Sec. 3.8.2.8) tends to increase with frequency.

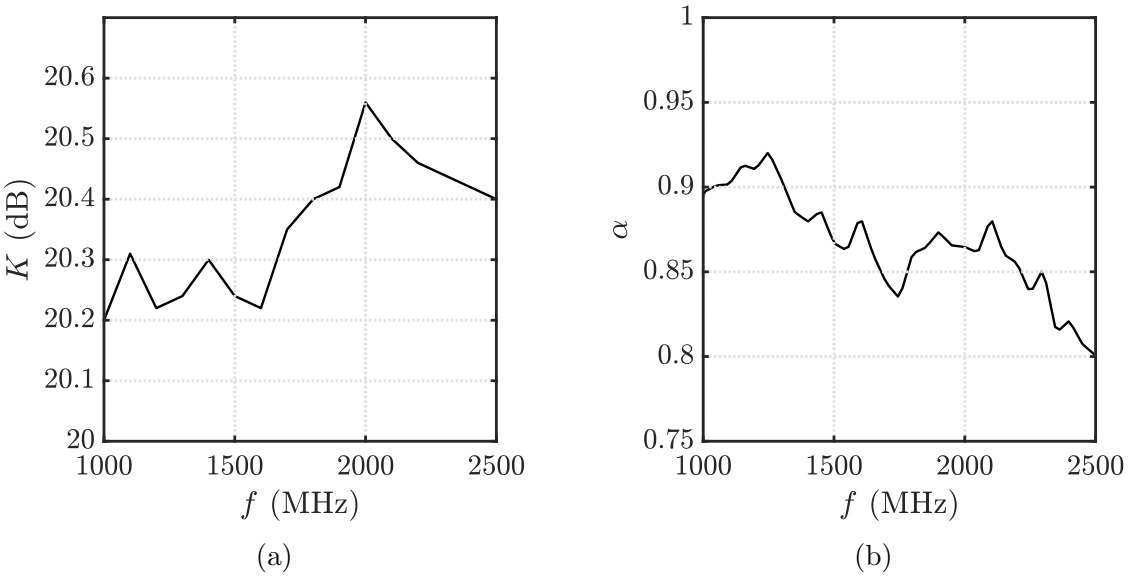

Figure 3.13: (a) Directional coupler coupling coefficient vs. frequency. (b) Attenuation coefficient vs. frequency for the setup used in the thrust measurement and optimization campaigns.

3.6.3.1 Combined Delivered Microwave Power Uncertainty

We estimate the total uncertainty in delivered power measurements by combining the uncertainties caused by power sensor and directivity errors. The error caused by directivity is not random in nature but systematic i.e. increasing the number

of measurements will not reduce directivity error. Because of this, we cannot add directivity error in quadrature with other errors, but must use a worst case scenario approach. Thus the total delivered power error is quantified as

$$\Delta P_{Abs} = \Delta P_{sens} + \Delta P_{directivity}. \tag{3.17}$$

3.7 Laser-Induced Fluorescence Diagnostics

The LIF diagnostics employed in this experiment are based closely on previous studies described in Refs. [26] and [35]. A tunable laser pumps the 834.953 nm (vacuum) metastable excited state of Xe II, which then emits a 542.066 nm (vacuum) photon as it relaxes to the Xe II ground state. We deduce ion velocities using the Doppler shift between the tunable input laser wavelength and the known 834.953 nm transition, given by

$$V_{ion} = c\left(\frac{\nu}{\nu_0} - 1\right) \tag{3.18}$$

where c is the speed of light, ν is the input frequency, and ν_0 is the metastable transition frequency. The exact setup is described in more detail in Ref. [26].

The large magnetic fields near the thruster may impact our measured VDFs through the effect of Zeeman splitting. Following Huang [51], at the maximum magnetic field strengths encountered by our LIF measurements ($\sim$ 400 G), we anticipate that Zeeman splitting will lead to symmetric broadening of the IVDF by $\sim$ 910 m/s. While at the exit plane this splitting is commensurate with the bulk velocity, moving further away from the source, the relative effect decreases as the ions are accelerated and the magnetic field drops from $\sim$ 400 Gauss at the exit plane to under 50 Gauss midway through the acceleration region. Here, the calculated fractional shift is less than 1%. Moreover, we infer the average velocity by fitting normal distributions to the data, which effectively removes the effect of this symmetric splitting. Zeeman

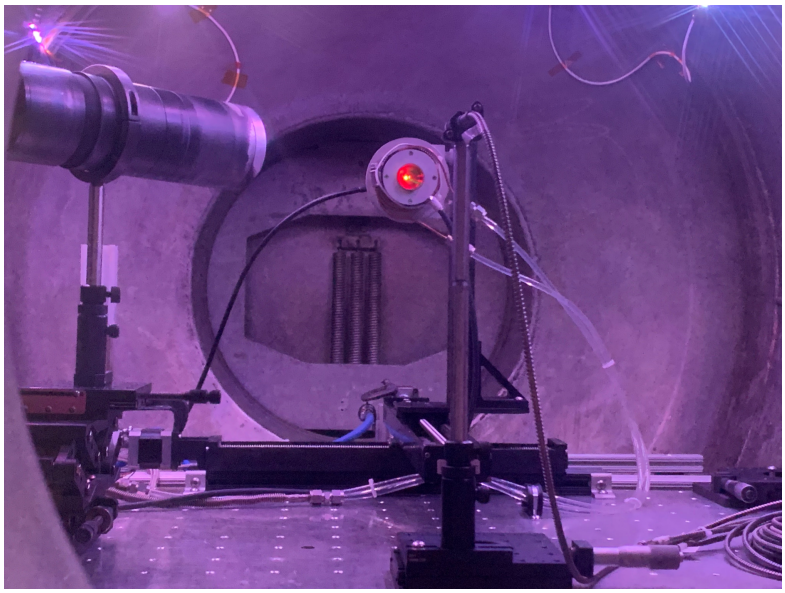

Figure 3.14: Laser-induced fluorescence setup during alignment

splitting thus is ignored in our analysis.

3.8 Direct Thrust Measurement Techniques for Low-Power ECR Thrusters

Thrust measurements are perhaps the most critical diagnostic in propulsion design, allowing mission designers to accurately predict spacecraft trajectories and set mass requirements. Accurately measuring the thrust forces produced by EP thrusters poses a unique challenge due to their low thrust-to-weight ratio. To give some perspective, a thruster weighing $\sim$ 1Kg on earth and producing a $\sim$ 1mN thrust has a thrust-to-weight ratio of 10^{-4}; equivalent to measuring a fraction of the weight of a penny with a device capable of supporting humans. As such, there has been a large body of research over the years dedicated to accurately assessing thrust forces in on-ground vacuum facilities [95].

Experimentalists can forgo direct thrust measurements by using proxy methods to extrapolate thrust based on non-direct measurements such as electrostatic probes,

laser induced fluorescence, or momentum flux sensors. However, these methods make several assumptions and are not as accurate or reliable as direct thrust measurements [16; 74; 31].

Direct thrust measurements for low-power RF and microwave driven thrusters, such as the ECR magnetic nozzle thruster, pose a particular challenge. These devices, intended for limited power small-sat missions, produce low force levels –typically less than 1 mN thust requiring greater force resolution than their high power counterparts. RF thruster operation additionally produces high levels of electrical and thermal noise relative to standard DC thrusters. In particular, the high-power coaxial cabling used in testing these systems poses a challenge from a thermal and structural standpoint.

In this section, we present the design and performance of a novel hanging pendulum thrust stand intended for microwave-driven thrusters. We describe its operation and provide sample results taken with the ECR II thruster.

3.8.1 Thrust Stand Operating Principle

Generally speaking, EP thrust stands fall into three categories; inverted pendulums, torsional pendulums, and hanging pendulums [95]. Our design uses a hanging pendulum architecture due to its overall simplicity and compactness. A schematic diagram of our thrust stand is shown in Fig 3.15. The design is similar to thrust stands that have been used previously to characterize ECR thrusters [118; 56] and ion thrusters [33; 46]. The operating principle is as follows: the thruster is mounted a distance l_T from a central flexural pivot. The thrust force it produces generates a torque τ_T about the pivot point causing the pendulum arm to rotate an angle θ. We measure the change in position of the pendulum arm using a fiber-optic displacement sensor. The sensor is pointed at a mirror mounted to the bottom of the pendulum arm located a distance l_{sens} from the pivot point. The sensor detects the distance δ_{disp}, which is fed to a DAQ system. We translate the distance readings, δ_{disp}, to force

measurements using an in-situ calibration system. The calibration systems works by dropping a series of calibration weights, m_{cal}, located at a distance, l_{cal}, from the pendulum pivot point. The thrust stand uses a counterweight, m_{CW}, located a distance l_{CW} above the pivot point to increase sensitivity compared to a conventional hanging pendulum design.

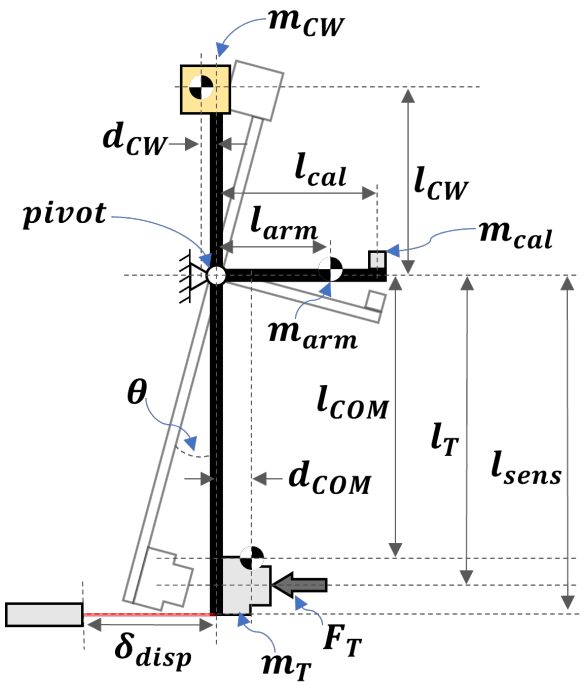

Figure 3.15: Schematic of thrust stand showing in null ($\theta = 0$) and displaced orientations.

Using a moment analysis about the central pivot point, we can relate the linear displacement, δ_{disp}, to thrust force F_T as follows:

$$\delta_{disp} = A_T F_T + b_0, \tag{3.19}$$

where the slope of the line is given by

$$A_T = l_{sens} \frac{l_T}{m_T g l_T - m_{CW} g l_{CW} + k}, \tag{3.20}$$

where k is the spring constant of the flexural pivot and g is the acceleration of gravity.

We provide a complete derivation of this expression in Appendix A.1. Equation 3.20 shows that the thrust stand's sensitivity can be increased by increasing the counterweight mass, m_{CW}, or position, l_{CW}. This allows the user to select higher signal to noise ratio (larger $m_{CW}gl_{CW}$) or decreased measurement settling time (smaller $m_{CW}gl_{CW}$).

As with all EP thrust stands, we must infer A_T in Eq. 3.19 using a calibration procedure. Most EP thrust stands use a known weight system, though other alternatives such as electrostatic combs and load cells are possible. Here, we use a variation of the known mass system in which we apply weights to the calibration arm a distance l_{cal} from the central pivot. This is a similar approach to that described in Ref. [56]. We show in Appendix A.2 that the relation between applied calibration mass and displacement is given by

$$\delta_{cal} = A_{cal}(m_{cal}g) + b_{cal}, \tag{3.21}$$

where A_{cal} is the slope relating calibration weight to displacement. We note that this is not the same slope as A_T in Eq. 3.19. This difference stems from the fact that the thrust force and calibration force are applied at different locations. Geometrically, we can relate relate this calibration slope to the slope in Eq. 3.19 with the expression:

$$A_{cal} = \frac{l_{cal}}{l_T} A_T \tag{3.22}$$

where $\frac{l_{cal}}{l_T} = \frac{1}{3}$ in our design. This calibration procedure must be repeated each time we adjust the counterweight.

3.8.2 Thrust Stand Design

In this section, we provide a detailed description of our thrust stand construction and its subsystems. For reference, we provide a CAD diagram and picture of the

thrust stand in Fig. 3.16. The dimensions and characteristic weights and thrust forces used in the design are listed in Table 3.1.

Table 3.1: Thrust stand properties

	Description	**Value**	**Units**
F_T	Thrust force	0.1-1	mN
m_T	Thruster mass	1.5	kg
m_{CW}	Counterweight mass	1.5	kg
m_{cal}	Calibration mass	0.1	g
l_T	y length: pivot to center of thrust	0.305	m
l_{COM}	y length: pivot to thruster center of mass	0.305	m
d_{COM}	x length: pivot to thruster center of mass	0.05	m
l_{CW}	y length: pivot to counterweight center of mass	0.08-0.22	m
d_{CW}	x length: pivot to counterweight center of mass	0.00	m
l_{cal}	x length: pivot to calibration weight center of mass	0.102	m
k	Pivot stiffness	0.0016	N-m/degree
g	acceleration of gravity	9.81	m/s^2

3.8.2.1 Structure

The thrust stand can be broken down into two main structural components: the stationary frame and the free-swinging pendulum arm. These parts are connected by two flexural pivots – stainless steel torsional springs – that allow rotation without the stiction inherent to sliding mechanisms such as ball bearings. Our design uses Riverhawk 5016-800 pivots shown in Fig. 3.17. Each has a stiffness constant of a 0.0142 in-lb/degree (0.0008 N-m/degree) load capacity of 26 kg giving the pendulum arm a total weight limit of 52 kg.

3.8.2.2 Calibration System

The calibration system consists of three servo actuators that are used to drop the calibration weights onto the calibration weight bar attached to the swinging pendulum arm. The weight bar, shown in Fig. 3.18, catches the calibration weights in a v-groove ensuring consistent placement during each calibration. The geometry is such that the

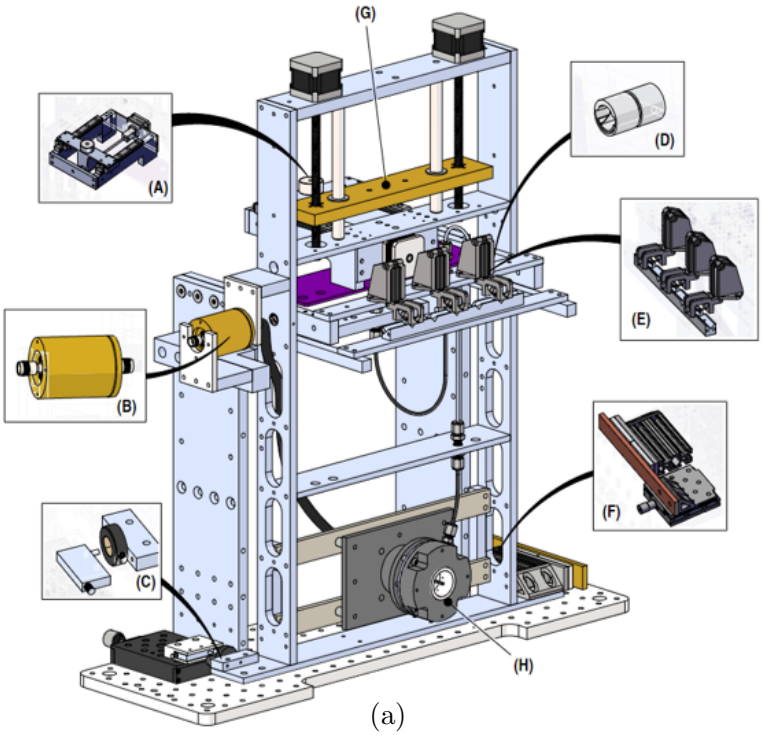

(a)

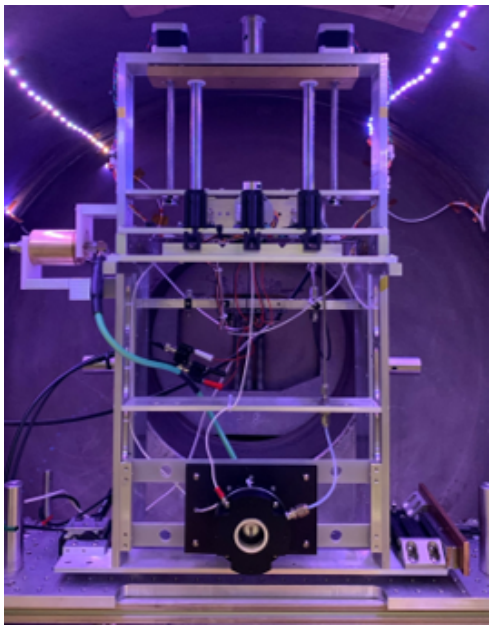

(b)

Figure 3.16: Thrust stand CAD model showing (A) horizontal counterweight, (B) wireless power coupler, (C) optical displacement sensor, (D) flexural pivot, (E) calibration system, (F) eddy-current damper, (G) vertical counterweight, and (H) ECR thruster, and (b) thrust stand installed in the Junior Test Facility

Figure 3.17: Riverhawk flexural pivots used in the thrust stand.

weights do not need a string to keep them in place, eliminating a common error source in these systems. We operate each servo can independently, and therefore can combine masses to create more calibration points than there are weights. By using two servos, we can test three test calibration points while three servos can test six different calibration weights. We weigh each calibration weight using a Mettler AE200 precision balance masses prior to thruster testing.

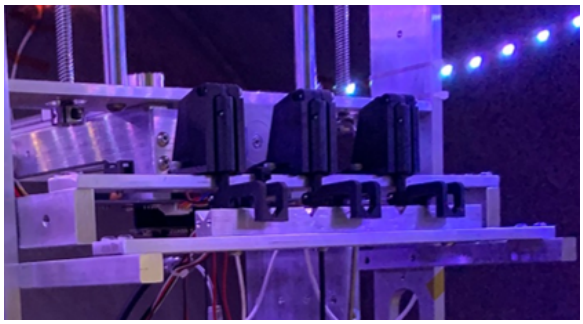

Figure 3.18: Calibration weight catcher.

3.8.2.3 Counterweight Systems

The thrust stand features two counterweights; one adjusts the force resolution and the other balances the pendulum arm. By moving the vertical counterweight, shown in Fig. 3.16(G)), we can effectively change the length l_{CW} as described by Eq. A.5. This, in turn, increases or decrease the thrust stand's sensitivity. The vertical counterweight is comprised of a 1.3 kg brass bar connected to the top of the pendulum arm using a pair lead screws. The lead screws are attached to two stepper motors that enable precise in-vacuum positioning. The horizontal counterweight,

shown in Fig. 3.16(A)), is used to orient the pendulum arm vertically. By maintaining a perpendicular angle between the pendulum arm and the ground, we can minimize calibration errors stemming from misalignment between the gravitational vector and the calibration bar normal. The horizontal counterweight in our design consists of an aluminum bar attached to the pendulum arm with a set of linear guide rails. The block is repositionable via a 9/64"-41.7" lead screw connected to a stepper motor. This provides in-vacuum positioning with sub-0.01 mm linear resolution, in turn allowing for sub-0.1°

3.8.2.4 Displacement Sensor

The thrust stand uses a Philtec D63 fiberoptic sensor (Fig. 3.16 (C)) to measure the pendulum arm displacement (δ_{disp}). The sensor works by transmitting infrared light to a target surface and measuring the intensity of the resulting reflected light. Our design uses a gold-coated mirror affixed to the bottom of the pendulum arm as the measurement target. These types of optical sensors have been shown to be more impervious to electrical noise emitted by RF thrusters than previously used linear variable differential transformer (LVDT) sensors [98].

The maximum possible thrust stand resolution is dictated largely by the displacement sensor's resolution. The D63 outputs an analog signal with an amplitude equal to 2.7 mV/μm while operating in its far range (typically between 0.5 and 1mm). We feed this analog signal to an 18-bit National Instruments PXI-6289 digital-to-analog converter. This yields a maximum possible displacement resolution <10 nm.

3.8.2.5 Eddy Current Damper

The thrust stand design employs an eddy current damper (Fig. 3.16 (F)) to reduce mechanical oscillations in the system. The damper uses a set of steel-backed neodymium magnets opposite a fixed copper bar mounted to the bottom of the pen-

dulum arm. The copper bar's position, and thus the damping force, is adjustable using a linear translation stage.

The thrust stand acts as a damped oscillator system; as such the damping ratio dictates the settling time required for thrust measurements. The fastest measurements possible require a critically damped system. It is in theory possible to achieve this damping value by adjusting the magnet-to-conductor gap. In practice, however, the strength of the magnets in our design leads to a slightly under-damped system for most thruster and counterweight masses. We note here that the magnetic materials are kept on the swinging portion of the thrust stand. This prevents the interaction of the damper magnets and thruster magnets from generating a net torque on the pendulum arm.

3.8.2.6 Electronic Systems

The thrust stand is equipped with several sensors and electronic systems to gather temperature, inclination, and electrical potential data, and to control the counterweight and calibration motors. We show a schematic diagram of the system architecture in Fig. 3.19. The electronic systems include four PT100 resistance temperature detectors (RTDs) for measuring the temperatures, a ADIS16209 tilt sensor for detecting the pendulum arm inclination, three stepper motor controllers for moving the vertical and horizontal counterweights, and three servomotors for raising and lowering the calibration weights. In its current configuration, the temperature sensors are positioned with one along the side of the fixed frame, one on each side of a flexural pivot, and one attached to the back of the thruster. The thrust stand uses two microcontrollers to communicate between the fixed and swinging portions of the thrust stand. This architecture allows data to be transmitted using only two data lines with the UART protocol. In total there are five wires spanning the swinging and fixed portions of the thrust stand: ground, +5V, TX, RX, and V_{sense}. We use 18 gauge

stranded silicone jacketed wire to reduce stiction. We transmit power to the thruster via a wireless power coupler described in Sec. 3.8.2.8.

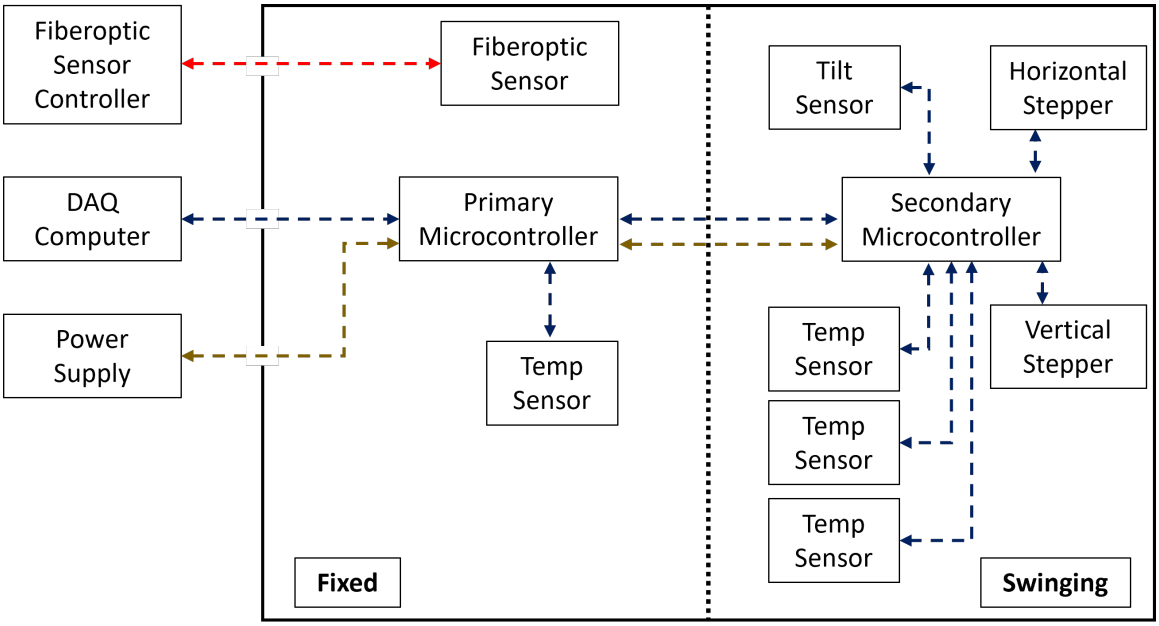

Figure 3.19: Schematic diagram of the thrust stand's electrical and fiber-optic connections.

3.8.2.7 Gas Interface

The ECR thruster used in testing requires only a single propellant feed. We use a 1/4 inch ID fluoroelastomer tube to feed to connect the fixed and free-swinging parts of the thrust stand.

3.8.2.8 Wireless Power Coupler

Delivering power to RF and microwave based thrusters typically involves heavy and relatively stiff coaxial cables that almost always contain dielectric materials – PTFE or polyethylene – that have high coefficients of thermal expansion (CTE). These properties inhibit their use in thrust stand testing as they both prevent the pendulum arm from swinging freely and cause thermal drift errors as they thermally expand [125]. Recent efforts to measure thrust on microwave thrusters have used

wireless power transfer techniques to avoid these errors [118; 110; 80]. Previous designs have included the use of pairs of standard rectangular wave guides separated by a small air gap (Refs. [110; 118]), and non-contact stripline joints (Ref. [80]).

(a) (b)

Figure 3.20: Wireless power coupler CAD model showing (a) dimetric and (b) cross section views

Our thrust stand uses a novel wireless power coupler that improves upon previous designs by increasing the bandwidth (in the case of rectangular waveguides), and alignment requirements (in the case of non-contact stripline joints). The coupler employs a coaxial air-gap design, as we show in Fig. 3.20. Each half is separated by a 1 mm gap. The coupler uses capacitive coupling to transfer power across the gap. This design provides greater bandwidths than most rectangular waveguide systems, while the axial symmetry yields a high tolerance to misalignment. This coupler allows microwave power in the range of 600-2490 MHz to be transferred to the thrust stand. Additionally, as with other designs, the coupler acts as a DC isolator, thus eliminating the need for lossy DC blocks on the thrust stand for tests requiring electrical isolation.

We designed the coupler using the COMSOL Multiphysics electromagnetics solver. We show the results of the spatially-resolved simulations for 1 and 2.4 GHz in Fig. 3.21. The coupler was manufactured using brass conductors and stainless steel TNC conections. The key figures of merit for this design are the s-parameters, S_{11} and S_{21}, over the frequency range of interest. We measured these values using an Agilent E5071C network analyzer shown in Fig. 3.22.

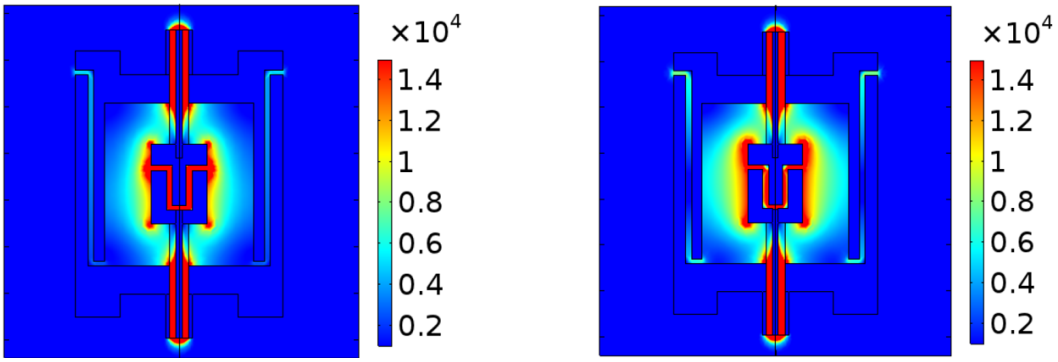

(a) (b)

Figure 3.21: COMSOL simulation of the wireless power coupler showing the electric field strength for (a) 1 GHz and (b) 2.4 GHz excitation

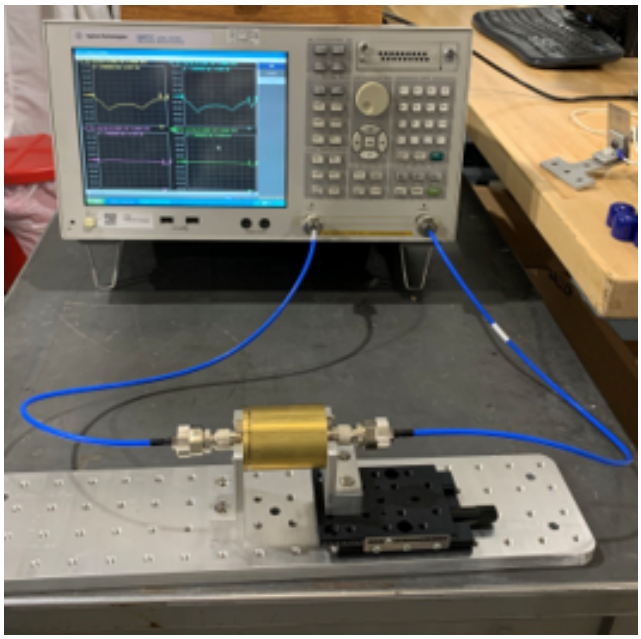

Figure 3.22: VNA testing the wireless power coupler.

The resulting plots, including the simulated data, are shown in Fig. 3.23. The measurements show a -1 dB bandwidth– the range over which 90% of incident power is transmitted– from 600-2490 MHz.

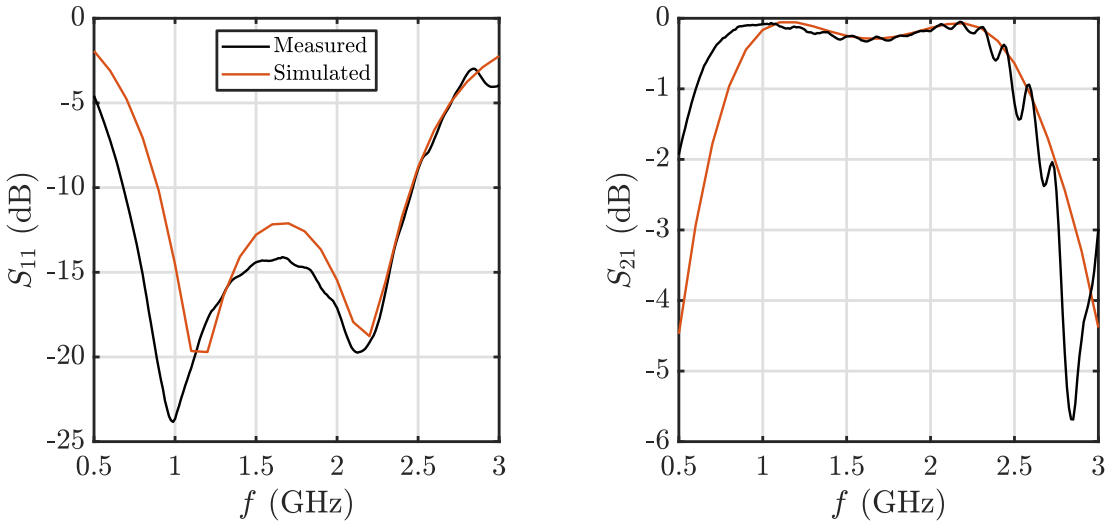

(a) Reflection coefficient, S_{11} (b) Transmission coefficient, S_{21}

Figure 3.23: Wireless power coupler simulated and measured S parameters

3.8.3 Thrust Stand Performance

In this section, we characterize the thrust stand performance by testing the following metrics: vibrational noise, thermal drift, electrostatic and electromagnetic interference, and finally cold gas and plasma thrust. Additionally, we show the results of the calibration procedure (as described in Sec. 3.8.2.2) with the vertical counterweight in two different positions, demonstrating the thrust stand's variable sensitivity. We use the calibration and ambient noise data to calculate the error in Sec. 3.8.6.

3.8.3.1 Vibrational Noise Analysis

Vibrational noise can affect thrust measurements in two ways; it can overwhelm displacement readings arising from thrust, and can cause false measurements when the thruster is pulsed close to the thrust stand resonant frequency. The vacuum chamber environment produces a significant amount of vibrational noise. In the Junior Test Facility, the main source of mechanical vibration is the cryogenic pump, which uses a reciprocating piston in its operation.

We characterized the noise environment by reading the displacement sensor's output with the thruster powered off. For this test, we recorded data for one minute at a rate of 200 samples/s. We present the raw displacement data in Fig. 3.24a. For comparison, we also show the results taken without the cryogenic pump in operation. The RMS displacements are on the order of 15 and 5 μM for the cryogenic pump on and off cases, respectively. Figure 3.24b gives the power spectral density of the readings using a Fourier Transform. The data show that the thrust stand has a natural oscillating frequency of ~ 11.9 Hz. Comparing the results with and without the cryogenic pumping, we that the cryogenic pump adds additional noise at ~ 9.7 and ~ 40.7 Hz. The results indicate that vacuum chamber noise can be easily averaged out with relatively short (< 1 s) averaging periods.

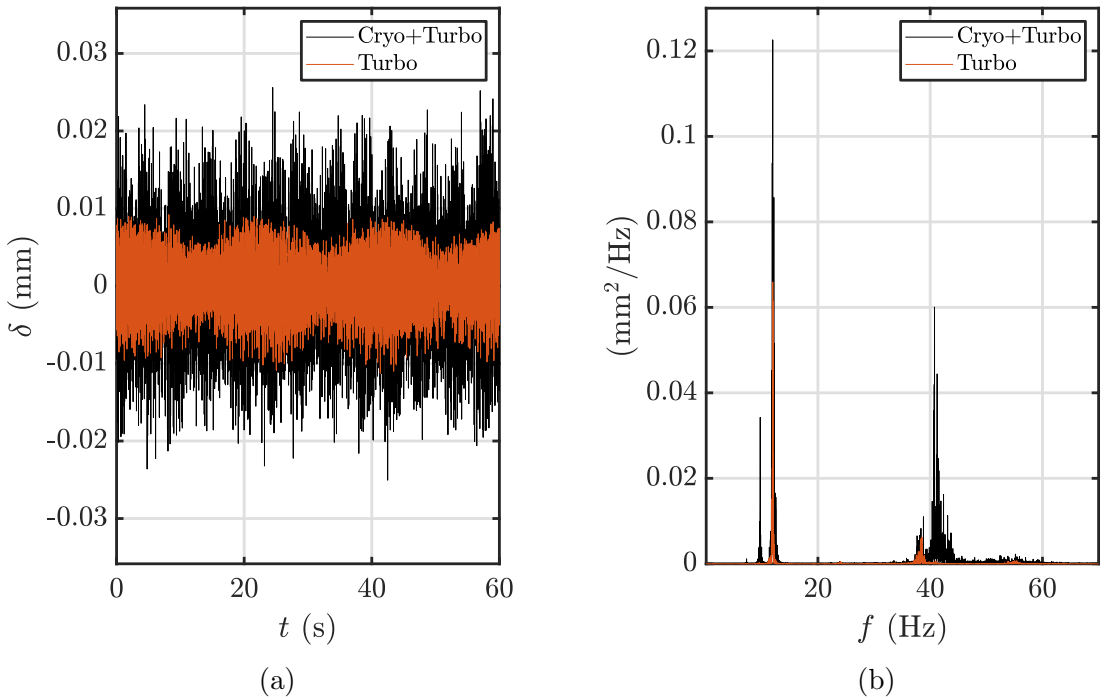

Figure 3.24: Thrust stand virbrational noise environment showing (a) displacement sensor output and (b) power spectral density

3.8.3.2 Calibration

In this section, we detail the calibration procedure and present the calibration results for the thrust stand in two counterweight configurations. Table 3.2 provides the calibration test point data, including test mass and equivalent force as calculated by Eq. A.10.

Table 3.2: Calibration points

Test Point	**Weights Used**	**Mass (g)**	**Equivalent Thrust (mN)**
1	1	0.0495	0.1618
2	2	0.1798	0.5878
3	1+2	0.2293	0.7496

The complete calibration procedure is as follows: we record data 12 seconds at 200 samples/second before and after all weights are dropped to capture thermal drift trends, as discussed in the next section. We then drop each calibration weight for 15 seconds total. Typically, we drop the weights in ascending and then descending order, as shown in Fig(3.25). In post-processing, we smooth the data using a Gaussian moving average filter with a 5 second window. We then employ a linear regression to fit a line to the first and last 10 seconds of data. Using this data, apply a linear correction factor to the data to remove the thermal drift. We average the last 5 seconds of data for each weight point to generate a displacement versus weight data point. The calibration slope is calculated by taking least squares fit of the calibration points.

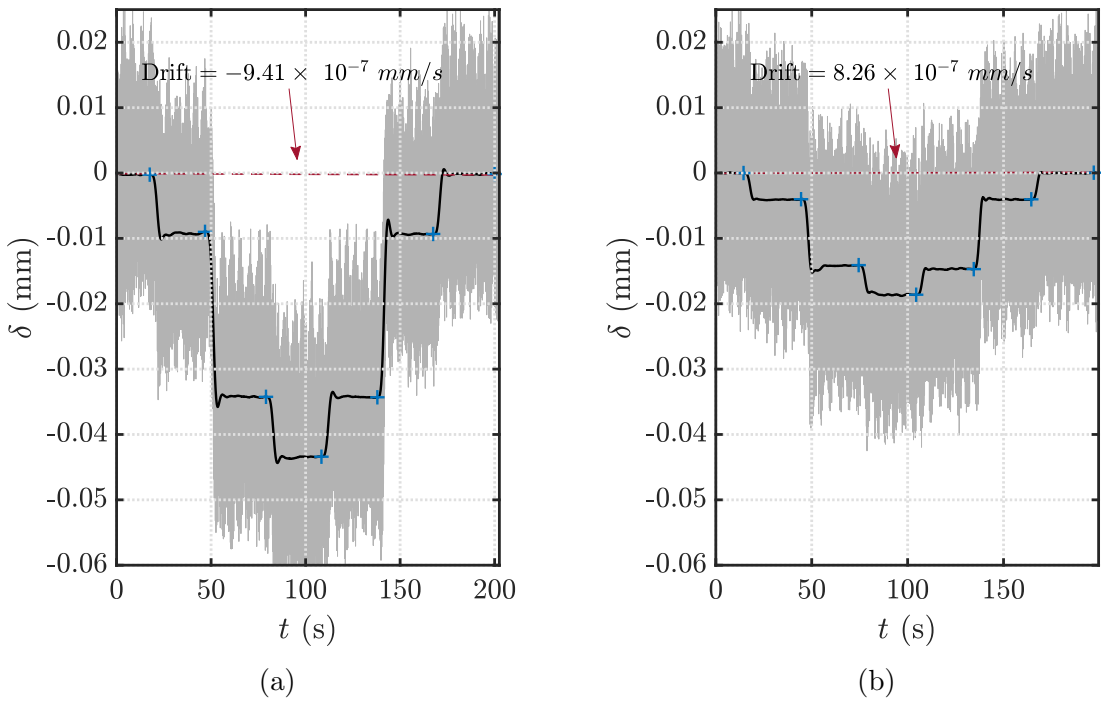

Figure 3.25: Calibration data showing the raw data and a linear fit

Figure 3.25 shows the calibration data for the thrust stand with the vertical counterweight at the upper limit (Fig. 3.25a), and 80 mm from the top (Fig. 3.25b). The grey lines are the raw displacement data (taken at 200 samples/second) while the smooth black line shows the output of the Gaussain moving average filter. The blue plus markers indicate the data points used for calculating the calibration slope. Figure 3.26 shows the resultant linear fits for displacement versus calibration force; -0.0580 mm/mN (-17.24 mN/mm) with the counterweight at the top position, and -0.0247 mm/mN (-40.49 mN/mm) with the counterweight 80 mm down.

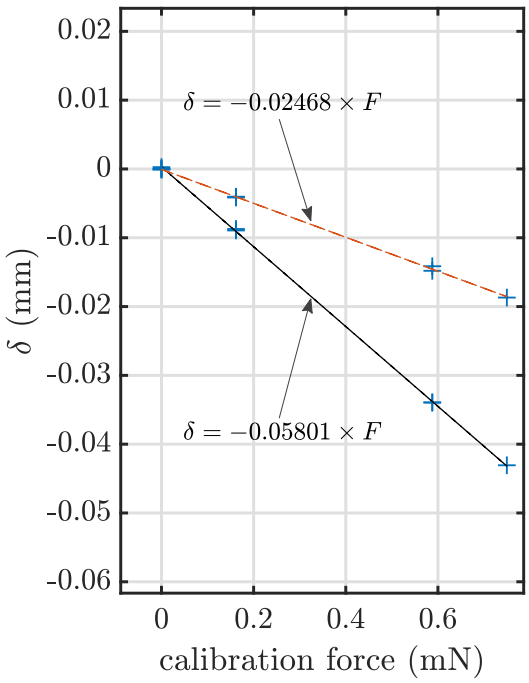

Figure 3.26: Fit of displacement vs. applied calibration force with the vertical counterweight in the top (black line) and bottom (orange line) positions.

3.8.4 Thermal Drift Characterization

In this section, we characterize the thermal drift exhibited by the thrust stand during typical thruster operation. This test is performed using a high power RF termination in place of the ECR thruster. This "dummy load" is shown mounted to the thrust stand in Fig. 3.27.

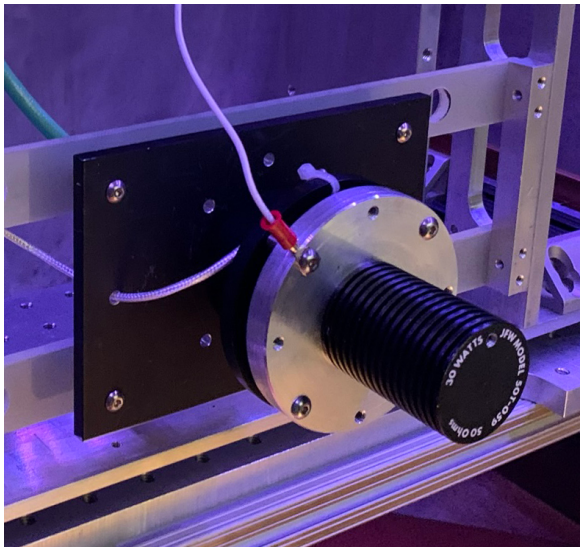

Figure 3.27: Dummy load used for thermal testing.

During the test, we supplied 30 watts of microwave power at 2400 MHz 30 minutes and recorded displacement and temperature data. The resulting plots are shown in Fig. 3.28a, with thruster temperature shown in red. Here, we can observe almost a direct correlation between thruster displacement and temperature. In Fig. 3.28b, we look at the 90 second window before and after turning off power to the thruster, as this is the timescale relevant to thrust acquisition. The black vertical lines in this plot show 15 provide the beginning and ending times for a typical thrust data point. The data indicate that although thermal drift is present, it follows a nearly linear trend on these timescales. We show the line derived from a linear fit – equivalent to -0.08 mN/minute– of the 15 seconds of data prior to power being shut off in blue in Fig. 3.28b. By subtracting the slope of this line from the data, we can remove the effects of thermal drift for thrust measurements without losing significant accuracy.

The observed thermal drift is likely caused by expansion in the flexural pivots. We tested this theory by applying heat tape to the fixed side of the pivots, which induced a drift in the opposite direction of that shown in 3.28a.

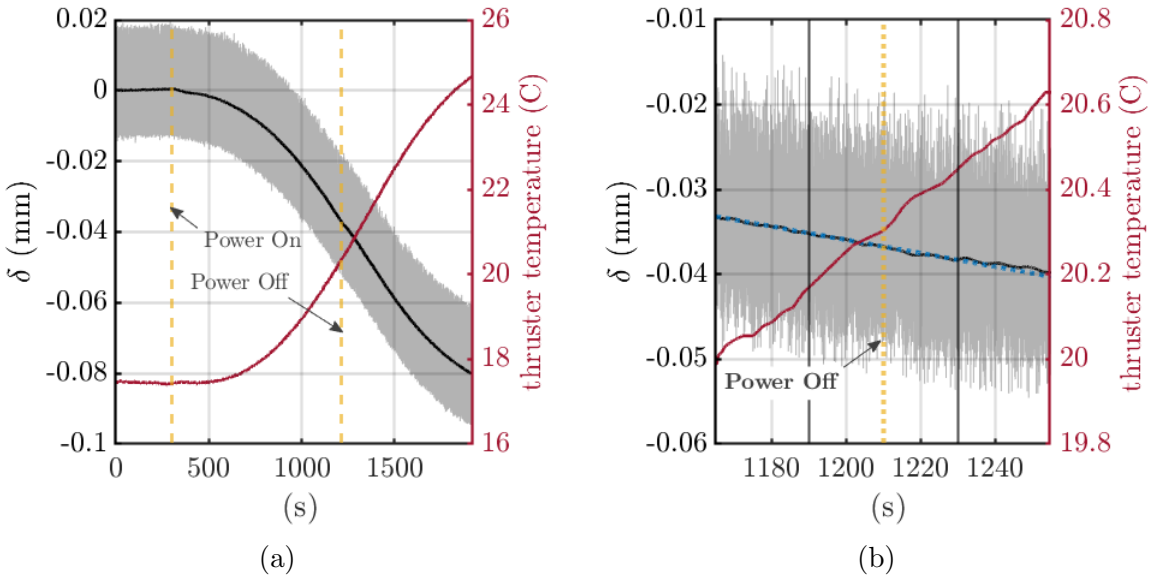

Figure 3.28: Thermal drift testing data (left). Close up view of the data showing a quasi-linear drift for timescales used for thrust measurements (right).

3.8.5 Electrostatic Testing

In this section, we examine the effects of electrostatic charging on thrust stand measurements. Evaluating this potential source of error is important as ECR thrusters have been shown to reach voltages over 200 V during operation. We test this effect by attaching an electrical contact to the thruster body and sweeping the potential from 0 to 300 V using an external DC power supply while measuring displacement. The results of this test are shown in Fig. 3.29. The data show that thrust readings are not affected in any significant way by electrostatic charge, eliminating this as a source of error.

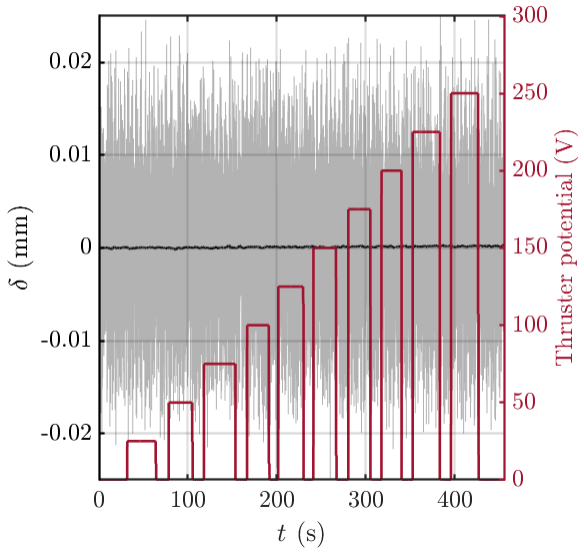

Figure 3.29: Results of electrostatic test showing negligible displacement caused by externally applied voltage.

3.8.6 Thrust Uncertainty Analysis

We quantify uncertainty in the thrust measurements following the approach outlined in Ref. [95]. In this formulation, measurement errors arise from four main sources: random disturbances in the displacement measurement (σ_δ), calibration slope errors ($\sigma_{k_{cal}}$), and geometrical tolerances of the center of thrust to pivot length (σ_{L_T}), and center of calibration force to pivot length ($\sigma_{L_{cal}}$). From these uncertainties, the total normalized uncertainty of a thrust measurement can be calculated as

$$\frac{\sigma_T}{T} = \sqrt{\left(\frac{\sigma_\delta}{\delta}\right)^2 + \left(\frac{\sigma_{k_{cal}}}{k_{cal}}\right)^2 + \left(\frac{\sigma_{l_t}}{l_t}\right)^2 + \left(\frac{\sigma_{l_{cal}}}{l_{cal}}\right)^2}. \tag{3.23}$$

We calculate the uncertainty in displacement, σ_δ, using the thrust stand's ambient displacement. The data in Fig. 3.24a show that while the displacement, δ_{disp}, exhibits a large deviation from the mean, the disturbances are mostly periodic and we can therefore eliminate most of this error by averaging the signal for a time $t_{avg} \gtrsim 100$ mS. However, by extending t_{avg} indefinitely, the averaged signal begins to incorporate

the non-linearity in the thermal drift, as shown in Fig. 3.28. This would cause a systematic error in the displacement measurement. We therefore encounter a trade-off in selecting t_{avg} between random error and thermal drift error.

Based on the data in Fig. 3.28, we chose an averaging time of $t_{avg} = 5$ seconds. We can now calculate σ_δ by taking the variance of the time averaged displacement data. Using the 60 second ambient data set yields a value of $\sigma_\delta = 8 \times 10^{-5}$ mm. We note here that this approach to calculating σ_δ differs from that used in Ref. [95], which uses the variance in calibration points. We believe this approach underestimates σ_δ for our thrust stand.

We can estimate the uncertainty in the thrust stand's calibration slope, K_{cal}, by taking the standard deviation a series of calibration measurements:

$$\sigma_{k_{cal}} \approx s_{K_{cal}} = \frac{s_\delta}{\sqrt{\sum_{i=1}^{n} \left(F_i - \bar{F}\right)^2}}, \tag{3.24}$$

where $s_{K_{cal}}$ is the standard deviation of the calibration slope, s_δ is the standard deviation of the time-averaged displacement (calculated from σ_δ), F_i is a sample calibration force, and $\bar{F}$ is the average of the applied calibration forces. For our calculation of $\sigma_{k_{cal}}$, we take 21 sample calibration points, which yields $\sigma_{k_{cal}} = 5.8 \times 10^{-5}$ mm/mN.

The geometric uncertainty of l_T and l_{cal} is based on manufacturing tolerances. For our thrust stand design we estimate these values to be $\sigma_{l_T} \approx \sigma_{l_{cal}} \approx 1$mm. From these components, we calculate an aggregate error using Eq. 3.23. We plot the 95% confidence interval ($2\sigma_T/T$) versus the measured thrust in Fig. 3.30. By introducing a maximum allowable error, we can use this plot to determine the thrust stand's minimum measurable unit of thrust. Setting the allowable error to 10%, for instance, yields a minimum force of $F_{min} \approx 25\mu$N.

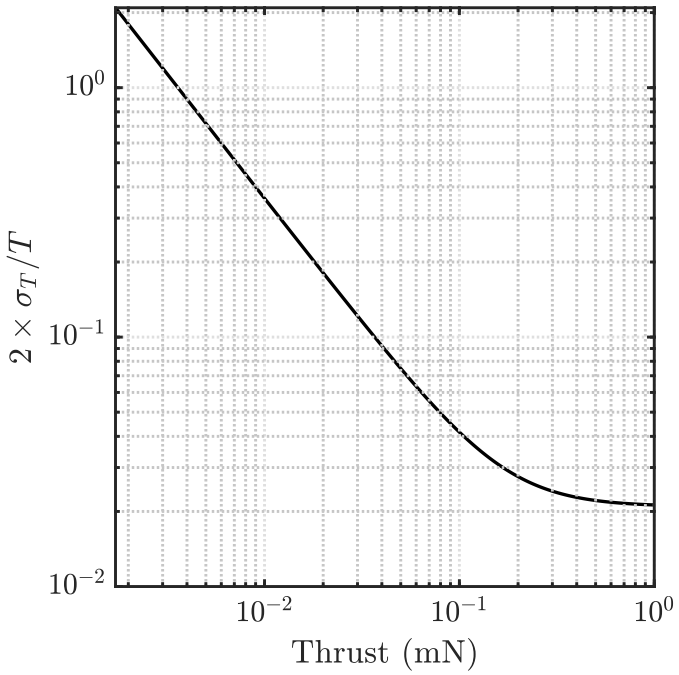

Figure 3.30: Normalized 95% confidence interval ($2\sigma_T/T$) vs. measured thrust force

3.8.6.1 Cold Gas Testing

As a preliminary benchmark, we measured the thrust produced by cold gas flow through the ECR II thruster. The tests were performed by flowing xenon propellant until reaching steady-state displacement. We then shut off the main propellant feed valve and determined thrust by measuring the difference in displacement. We show the data for the 1 and 5 sccm Xe cold gas tests in Fig. 3.31. In post-processing, we calculated cold gas thrusts of 0.012 +/−0.004 mN and 0.065 +/−0.004 mN for the 1 and 5 sccm cases, respectively. As is evident from Fig. 3.31a, 0.012 mN is close to the smallest force measurable by the thrust stand in its current configuration.

3.8.6.2 ECR Thruster Testing

In this section, we demonstrate the thrust stand's performance using the ECR II thruster. The tests were conducted with the 1 and 10 sccm Xe flow rates with delivered power ranging from 20-40 W. The procedure for measuring each thrust

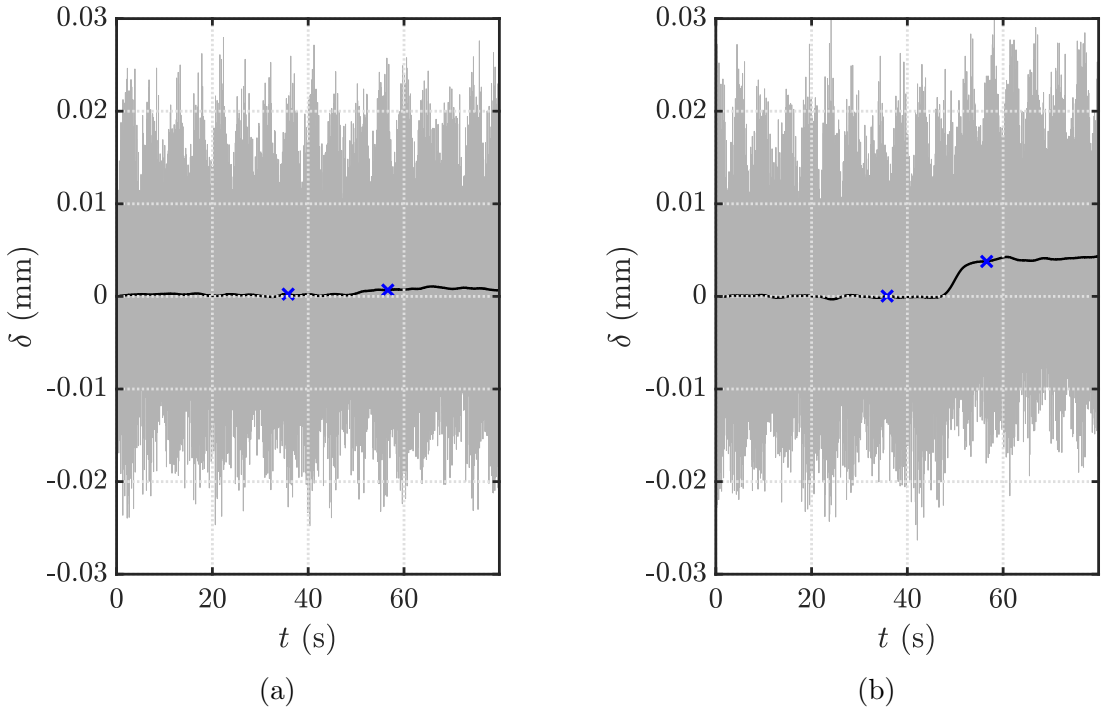

Figure 3.31: Cold gas thrust measurement for (a) 1 sccm Xe and (b) 5 sccm Xe

point was as follows: First, the thruster is brought to a quasi-steady-state operating temperature. This takes $\sim$ 1 hour depending on the operating condition. We then adjust the thruster to the specified power and flow rate settings. We allow the thruster to run until the forward and reverse powers level off, typically $\sim$ 30 seconds. At this point, we begin recording thrust data. For the thrust measurements presented here, we take the difference in displacement between the test point and the thruster off displacement.

We show a typical thrust measurement for a 24 watt (measured as delivered power), 1 sccm xenon operating condition in Fig. 3.32a. The detrended displacement is shown in Fig. 3.32b.

The data show a thrust of 0.408 mN. Incorporating the error analysis shown in Sec. 3.8.6 we get a 95% confidence interval of $F_T = 0.408\ ^{+}/_{-}\ 0.009$ mN.

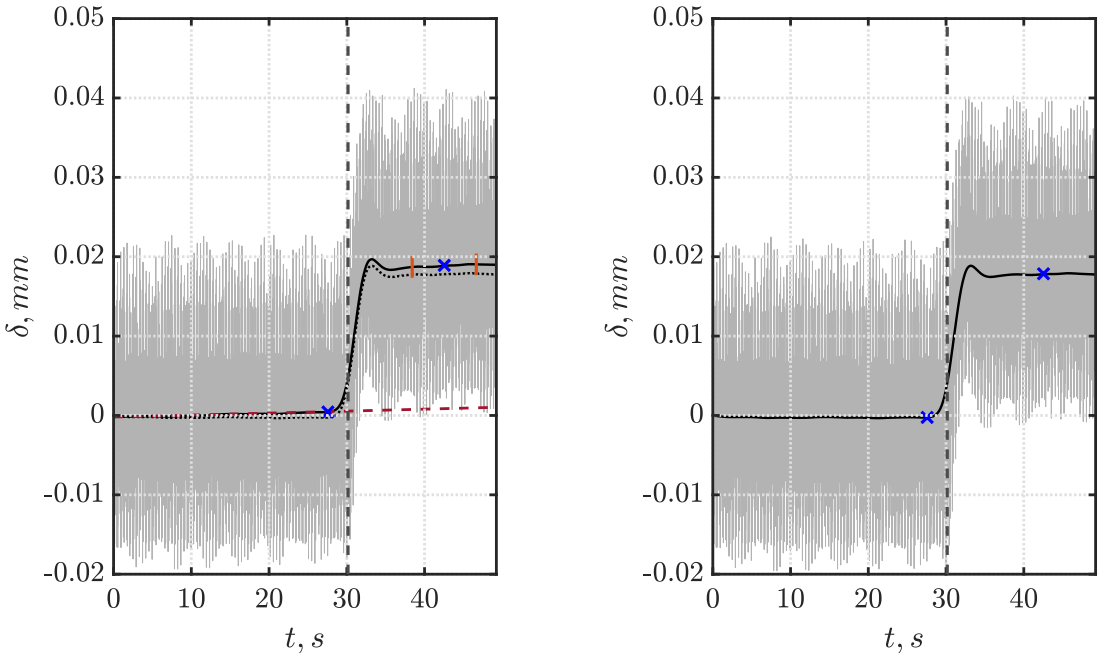

Figure 3.32: Raw thrust data for 30 W, 1 sccm Xe (left), and detrended data (right). The black line shows the five second Gaussian averaged signal. The blue x's denote the data points used in calculating thrust. The orange marks on the raw data figure show the stand and end times used for averaging the thrust off data.

3.9 Combined Power, Flow, and Thrust Measurement Uncertainty

In the previous sections, we calculated the uncertainties for mass flow rate, absorbed power, and thrust force. In this section, we combine these uncertainties to derive the total expected error for specific impulse and efficiency measurements.

We assume the uncertainties in flow rate, thrust force, and power sensor error can be modeled as random in nature. The uncertainty in absorbed power caused by directivity error, on the other hand, is systematic i.e. repeating the experiment will not yield values closer to the true value for errors caused by directivity. We therefore combine the errors in the flow rate, thrust, and power sensor uncertainty in quadrature, while the error caused by directivity is treated using a worst case scenario

approach [12].

3.9.1 Specific Impulse

The uncertainty for specific impulse, $I_{sp} = T/(g\dot{m})$, is a combination of uncertainties in thrust and mass flow rate measurements. Based on our previous assumptions, we model these errors as:

$$\Delta I_{sp} = \sqrt{\left(\frac{\partial I_{sp}}{\partial T}\Delta T\right)^2 + \left(\frac{\partial I_{sp}}{\partial \dot{m}}\Delta \dot{m}\right)^2}, \tag{3.25}$$

where the derivative terms are defined as:

$$\frac{\partial I_{sp}}{\partial T} = \frac{1}{g\dot{m}} \tag{3.26}$$

$$\frac{\partial I_{sp}}{\partial \dot{m}} = -\frac{T}{g\dot{m}^2}. \tag{3.27}$$

We take ΔT as the 95% confidence interval shown in Fig. 3.30 multiplied by the measured thrust. The flow rate uncertainty, $\Delta\dot{m}$, is assumed to be 5%. Using the thrust measurement shown in Fig. 3.32 as an example, we obtain a specific impulse of $I_{sp} = 342.8$ +/– 17.3 seconds.

3.9.2 Efficiency

The uncertainty in thrust efficiency incorporates the errors in force measurement, mass flow rate, and absorbed power. As described in Sec. 3.6.2, the absorbed power measurements is affected by both the power sensor error and the directivity error. The latter term is a systematic error and cannot be treated as a probabilistic distribution. Furthermore, the directivity error is a non-symmetrical about the nominal absorbed power, P_{Abs}. We thus determine the minimum and maximum efficiencies by adding the random errors in quadrature and incorporating this quantity into the maximum and minimum efficiencies dictated by the minimum and maximum absorbed powers

calculated based on directivity error. This formulation yields:

$$\eta_{max} = \frac{T^2}{2\dot{m}P_{min}} + \sqrt{\left(\frac{\partial\eta}{\partial T}\Delta T\right)^2 + \left(\frac{\partial\eta}{\partial\dot{m}}\Delta\dot{m}\right)^2 + \left(\frac{\partial\eta}{\partial P_{Abs}}\Delta P_{sens}\right)^2}, \tag{3.28}$$

$$\eta_{min} = \frac{T^2}{2\dot{m}P_{max}} - \sqrt{\left(\frac{\partial\eta}{\partial T}\Delta T\right)^2 + \left(\frac{\partial\eta}{\partial\dot{m}}\Delta\dot{m}\right)^2 + \left(\frac{\partial\eta}{\partial P_{Abs}}\Delta P_{sens}\right)^2}. \tag{3.29}$$

Here, the P_{min} and P_{max} terms are the minimum and maximum powers calculated from the directivity error analysis provided in Sec. 3.6.2. The derivative terms are given by

$$\frac{\partial\eta}{\partial T} = \frac{T}{\dot{m}P_{Abs}}, \tag{3.30}$$

$$\frac{\partial\eta}{\partial\dot{m}} = -\frac{T^2}{2\dot{m}^2P_{Abs}}, \tag{3.31}$$

$$\frac{\partial\eta}{\partial P_{Abs}} = -\frac{T^2}{2\dot{m}P_{Abs}^2}, \tag{3.32}$$

where P_{Abs} is given by P_{min} for the maximum efficiency and P_{max} for the minimum efficiency calculations.

Turning to the example point taken in the previous section, with a measured forward and reverse powers of $P_F^M/K = 13.0$ W and $P_R^M/K = 1.26$ W, we can calculate maximum and minimum absorbed powers of $P_{max} = 10.22$ W and $P_{min} = 7.63$ W. From here, we obtain a maximum and minimum thrust efficiency of $\eta_{max} = 7.03\%$ and $\eta_{min} = 5.25\%$.

3.10 Summary

We have presented the design and performance of a variable-sensitivity hanging pendulum thrust stand for measuring sub-millinewton forces. We demonstrated the ability to change the thrust stand's sensitivity from 40.49 mN/mm to 17.24 mN/mm

by moving its vertical counterweight. We additionally described the design and performance of a novel high bandwidth wireless power coupler for mitigating the effects of RF cable expansion during microwave-powered thruster testing. The thrust stand was tested using a low-power ECR thruster, demonstrating the ability to resolve $\sim 0.065 - 0.4\mu$N forces, with error under 3% for thrust levels above 0.1 mN. We tested the effects of environmental vibration, thermal drift, and electrostatic charge on the performance of the thrust stand. The thrust stand exhibited non-negligible thermal drift on the timescales relevant to thrust measurements; however this drift remained linear over the ~ 20 seconds needed to measure thrust. Electrostatic charging was shown to have no effect on thrust readings. Our error analysis showed a minimum viable thrust measurement on the order $\sim 25\mu$N.

CHAPTER IV

Facility Effects for Low-Power Magnetic Nozzle Thrusters

4.1 Introduction

In this chapter we explore the effects of on-ground facilities on thruster performance including finite background pressures and proximity to chamber walls. The possibility of EP thrusters interacting with the facility environment is a widely recognized problem in the field as it calls into the question our ability to extrapolate the measured performance of these systems to their intended environment in space. Understanding these effects is key to accurately assessing thruster performance and thus plays a critical role in optimizing these devices. To motivate this work, we note that typical EP vacuum facilities produce vacuum environments with neutral densities on the order of 10^{16} m^{-3} ($\sim$ 10^{-6} torr) during thruster operation. The neutral densities encountered by satellites in low-earth orbit can easily fall below 10^{14} m^{-3} [11]. Additionally, the presence of conducting walls can fundamentally alter the possible current paths generated during testing versus in space.

4.2 Finite Background Pressure Effects

Previous theoretical and experimental studies have demonstrated that thruster interaction with background neutrals can fundamentally differ between EP thruster technologies. Hall thruster thrusters, for instance, tend to exhibit higher thrusts as background pressure increases, resulting in artificially high efficiencies measured in on-ground testing [108; 47; 88]. ECR magnetic nozzle thrusters have demonstrated the opposite trend with higher background pressures resulting in a performance drop [117]. Thus the mechanisms that have been proposed to explain facility effects in Hall thrusters do not seem to apply to magnetic nozzles.

A potential explanation for the differing pressure responses between Hall thrusters and magnetic nozzle thrusters stems from the location of the ion acceleration inherent to each design. In Hall thrusters, ion acceleration tends to occur over a relatively short region, often $\sim 1/5$ the total thruster length, near the thruster exit plane [52; 20; 19]. The acceleration process in ECR thrusters, on the other hand, has been experimentally shown to take place over a distance greater than several thruster lengths [57]. This effect leads to the acceleration region being several times the volume of the thruster and thus makes these devices more susceptible to interaction with background neutrals.

4.2.1 Previous Experimental Work

There have been a number of theories to date to explain the unique response of magnetic nozzles to finite pumping speed. These have included background neutral ingestion impacting the energy balance in the upstream source region where the plasma is formed [17], as well as energy losses due to the onset of secondary discharges occurring outside the thruster plume when the neutral environment is sufficiently high [65].

Recent works by *Vialis et al.* [117] and *Collard and Jorns* [27] have shown that

the presence of excess neutrals also can directly impact the dynamics of the magnetic nozzle itself, i.e. the ability to convert thermal energy into directed kinetic energy. These works have demonstrated, for example, that the acceleration profile of ions is correlated with the presence of neutrals and that changes in performance can be explained almost entirely by these shifts in the acceleration. This suggests that neutral collisions in the plume may in fact be the dominant driver for many of the pressure-related facility effects in low-power devices. With that said, despite the existing correlation and phenomenological evidence, it has not been established causally why the presence of neutrals could yield these types of changes in the acceleration region.

Thrust stand measurements by *Vialis et al.* [117] and *Peterschmitt* [92] demonstrated that ECR thruster efficiency can decrease by more than a factor of two (9% to 3.9%) as pressure is doubled (5.4 μTorr to 9.75 μTorr). These results are re-created in Fig. 4.1.

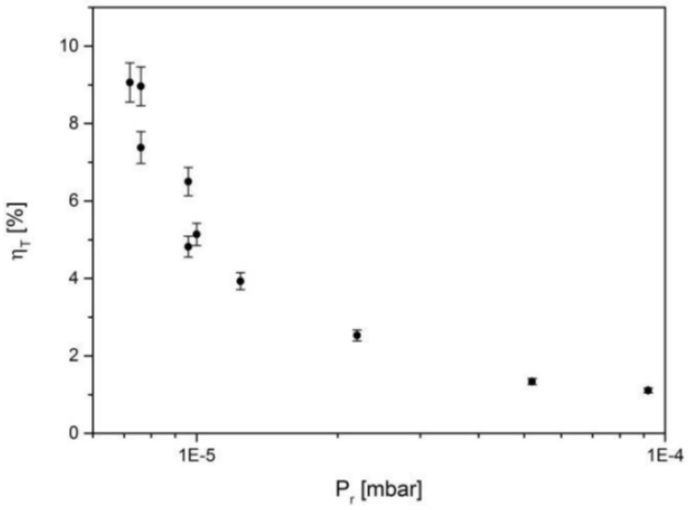

Figure 4.1: Previous thrust stand measurements showing decreasing efficiency as chamber pressure increases, from Ref. [117]

Using Faraday probe measurements, Vialis found that the divergence of plasma within the plume increased and on-axis ion current density decreased by almost 75% as background pressure was raised. Studies of magnetic nozzles employing a helicon plasma source that were conducted at higher facility pressures (14 to 66 μTorr, 100

W) revealed similar trends [17].

4.2.2 Theory Relating Background Pressure to Plume Ion Energy Losses

The governing hypothesis of this work is that changes in nozzle performance with increasing facility pressure can be explained by the unrecoverable loss of ion and electron energy that results from collisions with the background gas. This process acts as an energy sink that curtails the ability of the nozzle to effectively convert thermal energy introduced in the source into directed kinetic energy for thrust at the exit. We represent this loss explicitly by defining a power balance for the plume region of the thruster under the assumption of ambipolarity at the nozzle throat and exit, as well as quasi-1D expansion along the diverging magnetic field:

$$P_t = \frac{1}{2}\dot{m}_{i(e)}u_{i(e)}^2 + Q_{e(e)} + \frac{\dot{m}_{i(e)}}{m_i}\frac{5}{2}T_{e(e)} + P_{ec} + P_{cex}. \tag{4.1}$$

Here we have defined P_t as the power entering the plume at the nozzle's throat, and we have denoted the power that leaves the nozzle geometry at the exit as the combination of ion kinetic energy, $\frac{1}{2}\dot{m}_{i(e)}u_{i(e)}^2$, electron heat flux $Q_{e(e)}$, and the flux of thermal energy, $\frac{\dot{m}_{i(e)}}{m_i}\frac{5}{2}T_{e(e)}$. In these expressions, m_i denotes ion mass, u_i denotes ion speed, and the subscripts refer to the (e) exit and (t) throat regions shown in Fig. 4.2. We also have introduced two terms that represent the power lost by interspecies collisions: P_{ec}, the power consumed by electron-neutral ionization and excitation collisions and P_{cex}, the power absorbed by charge exchange (CEX) collisions between ions and neutrals within the plume. We provide a complete derivation of Eq. 4.1 in App. B.

The balance in Eq. 4.1 shows quantitatively that the kinetic energy of the flow (which is the component that contributes to thrust) can be decreased in two ways. The first is that there is residual thermal energy in the flow as it exits the nozzle.

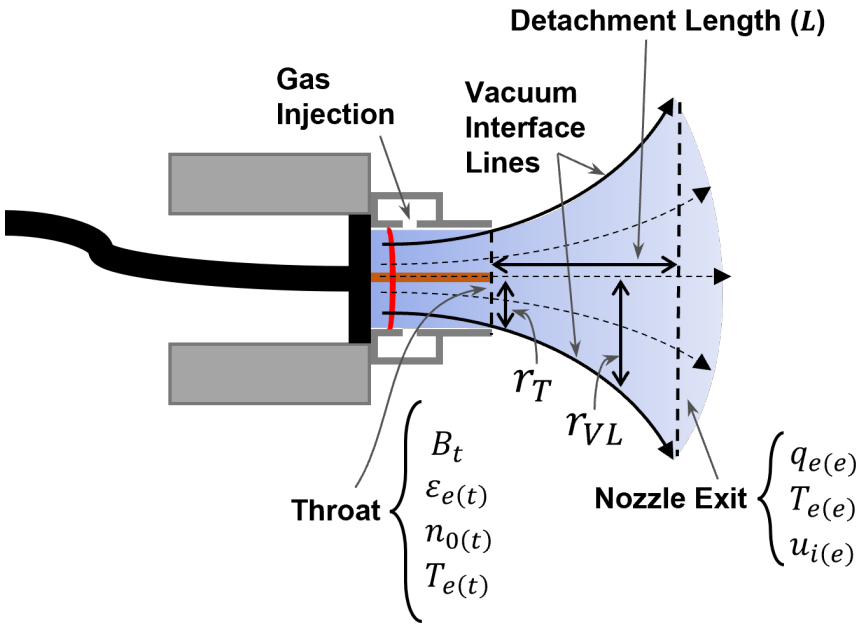

Figure 4.2: Notional cross-section for the magnetic nozzle thruster showing key features of the discharge including the throat (t), thruster radius (r_T), vacuum interface lines (r_{VL}), acceleration length, and nozzle exit (e)

This is a consequence of imperfect nozzle expansion and can be represented as a nozzle conversion efficiency (see Ref. [27] for more on this topic). The second loss—and the one which is the focus of this investigation—is the power that is absorbed by interspecies collisions that is not recovered. Using this model, we in principle can directly relate the power consumed within the plume by these collisions to a reduction in final ion velocities. Estimating the quantities involved in this expression explicitly, however, requires a detailed description of the plasma properties in the primary discharge and plume regions. In the following, we motivate simple 0D and quasi-1D models for each of these contributions.

4.2.2.1 Plume energy loss model

In this section, we present models for the loss terms in Eq. 4.1: P_{cex}, which stems from ion-neutral collisions and P_{ec}, which stems from electron-neutral collisions. To this end, we use global models based on those presented in Chapter 2 to derive plasma

properties in the thruster and plume.

Ion-neutral collisions in the plume Both CEX and elastic ion-neutral collisions can occur in the plume of the magnetic nozzle. We only consider the former, however, as they are a more dominant contributor in influencing changes in ion momentum and energy in the plume [9]. We quantify the power consumed by CEX collisions in the plume volume, V_{plume}, starting with the relation

$$P_{cex} = \int_{V_{plume}} \frac{1}{2} n_i m_i u_i^2 \nu_{cex} dV, \tag{4.2}$$

where n_i is the ion number density, u_i is the accelerated ion velocity, which we assume to be monoenergetic, and ν_{cex} is the CEX collision rate given by $\nu_{cex} = n_g \sigma_{cex} u_i$. Here, n_g is the neutral gas density and σ_{cex} is the cross section for CEX collisions in xenon given as a function of ion energy by an empirical approximation in Ref. [84].

In order to simplify this integral, we again invoke a quasi-1D approximation for the expanding nozzle flow such that $n_i d^3x = \frac{\dot{m}_i}{m_i} \frac{1}{u_i} dx$. This allows us to write Eq. 4.2 as

$$P_{cex} = \int_0^L \frac{1}{2} \dot{m}_i \nu_{cex}(x) u_i(x) dx. \tag{4.3}$$

For this expression, in addition to the quasi-1D approximation, we have assumed stationary neutrals and approximated the ion mass flow, $\dot{m}_i$, as constant throughout the plume. We similarly have introduced an effective length, L, that bounds the plume region. This length (labeled acceleration length in Fig. 4.2) corresponds to the point where the nozzle induced acceleration of the ions is complete and is commonly referred to as the detachment point. The location of this point is not fully understood and cannot easily be calculated. Using experimental measurements of ion velocity, however, we can estimate this length as the point where ion acceleration ceases [27]. Each CEX collision in this expression consumes 100% of the incoming ion's kinetic

energy. We can therefore neglect collisions between secondary ions and neutrals. We note here that this analysis gives an upper bound on P_{cex} as in practice $\dot{m}_i$ for primary ions will decrease with each CEX collision.

Electron-neutral collisions in the plume We calculate the power consumption from electron-neutral collisions in the plume using global models similar to those described in Chapter 2. Using this approach, we can write the total energy lost to electron-neutral collisions, P_{ec}, as

$$P_{ec} = \int_{V_{plume}} n_{g(plume)} n_e \left(K_{iz}\varepsilon_{iz} + K_{ex}\varepsilon_{ex} + K_{el}\varepsilon_{el}\right) dV, \tag{4.4}$$

where $n_{g(plume)}$ denotes the local neutral gas density and n_e is the local electron density.

Evaluating these expressions for electron-neutral power consumption requires that the electron temperature, neutral density, and plasma density all be known within the plume region. Additionally, an effective plume volume must be defined over which these collisions affect the ion acceleration. We can estimate these parameters using an analysis similar to that presented in Ref. [66] in which electrons are assumed to be isothermal. In practice, the complex nature of electron heat flux, such as the known cooling that occurs within the accelerations region, makes this assumption approximate [103; 81; 66]. However, this type of isothermal analysis has been successfully employed in scaling laws for these types of thruster models [7; 62]. Since the rate coefficients and energies depend only on temperature, this assumption allows us to re-write Eq. 4.4 as

$$P_{ec} = \left(K_{iz}\varepsilon_{iz} + K_{ex}\varepsilon_{ex} + K_{el}\varepsilon_{el}\right) \int_{V_{plume}} n_{g(plume)} n_e dV, \tag{4.5}$$

where we are able to remove the temperature dependent terms from the integral. For

the local plasma density, n_e, we make the assumption that the plasma undergoes a quasi-1D expansion along a surface of constant magnetic flux. We therefore can relate the density of the throat, $n_{e(t)}$ (estimated in Sec. 4.2.2.2) to the density in the plume using

$$n_e = n_{e(t)} \left(\frac{r_T}{r_{VL}(x)} \right)^2, \tag{4.6}$$

where r_T denotes the radius of the throat and $r_{VL}(x)$ denotes the location of the vacuum interface line (Fig. 4.2), which is determined by following the magnetic streamline that intersects the throat at r_T. This is shown in Fig. 3.2 for the ECR I thruster. We approximate neutral density, $n_{g(plume)}$, as constant throughout the chamber and base our estimates on pressure measurements taken during testing, as we discuss in Sec. 4.2.4.1. The effective plume volume, V_{plume}, is defined as the region bounded by the vacuum interface lines from the throat to the acceleration region exit.

4.2.2.2 Primary Discharge Model

In order to evaluate plasma properties at the nozzle throat analytically, i.e. P_t and the inlet plasma conditions, we employ a particle and energy balance for uniform density discharges based on the analysis provided in Sec. 2.5. In this version of the model, the electron energy loss term is augmented to accurately capture the power consumed by plume collisions. We additionally do not include the effects of neutral depletion in this model in order to simplify the calculations.

Electron Temperature Calculation In order to estimate the electron temperature in the nozzle plume, we consider the 0D particle balance in the source:

$$n_e u_B A_{eff} = K_{iz} n_g n_e V_{eff}, \tag{4.7}$$

where n_e is the plasma density in the source, u_B is the Bohm velocity, n_g is the neutral gas density in the source, K_{iz} is the ionization rate constant, V_{eff} is the effective ionization volume, and A_{eff} is an effective loss area given by $A_{eff} = 2\pi R^2 h_l + 2\pi R l h_R$. Here h_l and h_R are the plasma sheath edge to center density ratios for the axial and radial boundaries, respectively. For our calculations, we ignore the effects of the magnetic field within the discharge region and assume that ion diffusion can be modeled using h_l and h_R factors used in the low-pressure transport model for cylindrical geometries given in Ref. [70]. Eliminating n_e from Eq. 4.7, we can determine the electron temperature for a given geometry (which is known) and neutral density (Sec. 4.2.4.1).

Plasma Density Calculation Plasma density is calculated using an energy balance that equates the total absorbed power to the energy lost for each ion-electron pair, $\varepsilon_T = \varepsilon_c + \varepsilon_e + \varepsilon_i$, multiplied by the plasma loss rate, $u_B n_{e(s)}$, where $n_{e(s)}$ is the plasma density at the sheath edge. The energy term is composed of the collisional losses, $\varepsilon_c = \varepsilon_{iz} + \varepsilon_{ex} + \varepsilon_{el}$, ion kinetic energy loss at the sheath edge $\varepsilon_i = \frac{1}{2}T_e$, and electron energy losses at the sheath edge, $\varepsilon_e = 2T_e + \varepsilon_{ei}$. Here ε_{ei} captures the electron energy losses in excess of the thermal energy at the sheath boundary. For the radial boundaries and back wall, this term represents the energy transferred to ions as they fall through the sheath to the wall, V_s.

For the open boundary (the throat), this term is more complex and requires some knowledge of the plume dynamics. For our analysis, we take the electron energy losses at the throat to be the sum of the energy transferred to ions and neutrals in the plume, $\varepsilon_{ei(plume)}$, and an additional term representing the remaining energy contained in the electrons exiting the plume, $\varepsilon_{e(e)}$. Thus the energy loss term for electrons exiting the throat becomes

$$\varepsilon_{e(t)} = \varepsilon_{ei(plume)} + \varepsilon_{e(e)}. \tag{4.8}$$

Following Refs. [62] and [7], $\varepsilon_{e(e)}$ can be approximated as the sheath energy given in Eq. 2.26 for nozzle exits near a chamber wall or as $\frac{5}{2}T_e$ for plasmas expanding into an open boundary. We explore both limits in this Sec. 4.2.4.

We can relate the electron energy loss term given in Eq. 4.8 to those used in Eq. 4.1 using the following expressions:

$$\varepsilon_{ei(plume)} = \frac{m_i}{\dot{m_{i(e)}}}\left(\frac{1}{2}\dot{m_{i(e)}}u_{i(e)}^2 + P_{ec} + P_{cex}\right) \tag{4.9}$$

$$\varepsilon_{e(e)} = \frac{m_i}{\dot{m_{i(e)}}}Q_{e(e)} + \frac{5}{2}T_{e(e)}. \tag{4.10}$$

From these relations, we can observe that the open boundary expression is equivalent to setting the electron heat flux at the plume exit, $Q_{e(e)}$, to zero in Eq. 4.1.

A first principles assessment of $\varepsilon_{e(e)}$ requires an analytical expression for electron heat flux at the nozzle throat, which is in turn affected by the downstream magnetic nozzle dynamics. The theoretical nature of this heat flux remains an open and active area of research [45]. For the purpose of this investigation where our goal is to examine the dynamics downstream of the throat, we forgo attempting to calculate this and instead use ion velocity measurements to inform these values, as discussed below. Using these definitions, the primary discharge power balance can be written as

$$P_{abs} = n_0 u_b\Big((\pi R^2 h_l + 2\pi R l h_R)(\varepsilon_c + \varepsilon_i + \varepsilon_{e(w)}) + \pi R^2 h_l(\varepsilon_c + \varepsilon_i + \varepsilon_{e(t)})\Big), \tag{4.11}$$

where P_{abs} is the total power absorbed by the plasma and R and l are the discharge region's radius and length, respectively. The ion mass flow rate and resulting power

flowing through the thruster's throat is then given by

$$\dot{m}_i = \pi R^2 h_l u_b n_0 m_i \tag{4.12}$$

$$P_t = \frac{\dot{m}_i}{m_i}\left(\varepsilon_i + \varepsilon_{e(t)}\right). \tag{4.13}$$

Combining Eqs. 4.7-4.13, we are left with the following unknowns: n_g, $n_{g(plume)}$, P_{abs}, $u_{i(e)}$, and $Q_{e(e)}$. For the analysis presented here, we use numerical simulations to determine n_g while P_{abs}, $u_{i(e)}$, and $n_{g(plume)}$ are measured experimentally. Given values for these four unknowns and an expression for $Q_{e(e)}$, which we explore in Sec. 4.2.5, we can solve iteratively for the variables of interest, namely P_t, P_{cex}, P_{ec}, and $\varepsilon_{ei(plume)}$. Finally, by holding $\varepsilon_{ei(plume)}$ constant over a range of neutral pressures (thus assuming that the total energy transferred to the plume is constant), we can use a single measured value of $u_{i(e)}$ to calculate accelerated ion velocities as a function of background pressure.

In summary, in the previous section, we introduced a series of global power balances to assess how the exhaust velocity of ions exiting the magnetic nozzle will depend on the introduction of neutrals in this region. The prevailing hypothesis is that inelastic collisions will remove thermal energy from the flow, acting as an effective loss term, driving down performance. This is in keeping qualitatively with measurements to date. In the next sections, we examine the validity of this scaling law by employing a controlled experiment in which we characterize changes in ion velocity as a function of facility pressure.

4.2.3 Experimental Setup for Investigating Background Pressure Effects

We evaluate our theory relating background pressure to thruster performance by investigating ion velocities in the plume of an ECR thruster under varying neutral background densities. For this experiment, we used the ECR I thruster described in

Sec. 3.2.1.

The thruster was placed in the center of the chamber, approximately 1.5 meters from the end cap, where the thruster's plume terminates.The typical base pressure observed during the experiment was 2.3×10^{-7} Torr-N_2. In order to vary operating background pressure, we added a second gas injection port at the back of the chamber, as shown in Fig. 4.3. We then flowed between 0 and 40 sccm xenon to vary the background pressure.

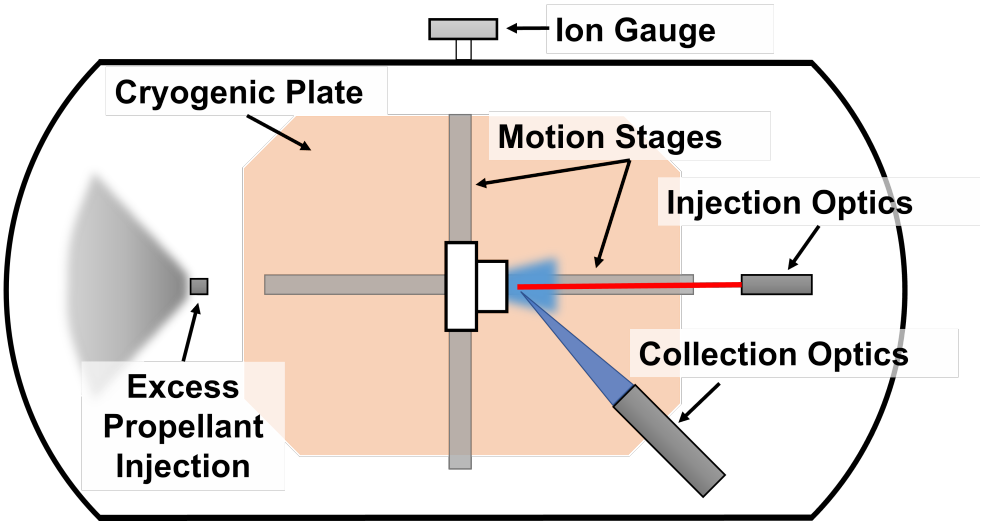

Figure 4.3: Schematic of facility and diagnostics with relative positions indicated.

4.2.4 Impact of Background Pressure Increase

In this section, we present experimental results quantifying the impact of increasing background pressure on the dynamics of the magnetic nozzle. We then compare this data to the predictions of the model outlined in Sec. 4.2.2. To this end, we first report our measurements of facility pressure and neutral density. We then investigate the role of facility pressure on the RF coupling to the plasma. Finally, we present the measured ion velocities in the magnetic nozzle at each of the three background pressures tested. We conclude by interpreting these results in the context of the governing relations resented in Sec. 4.2.2.

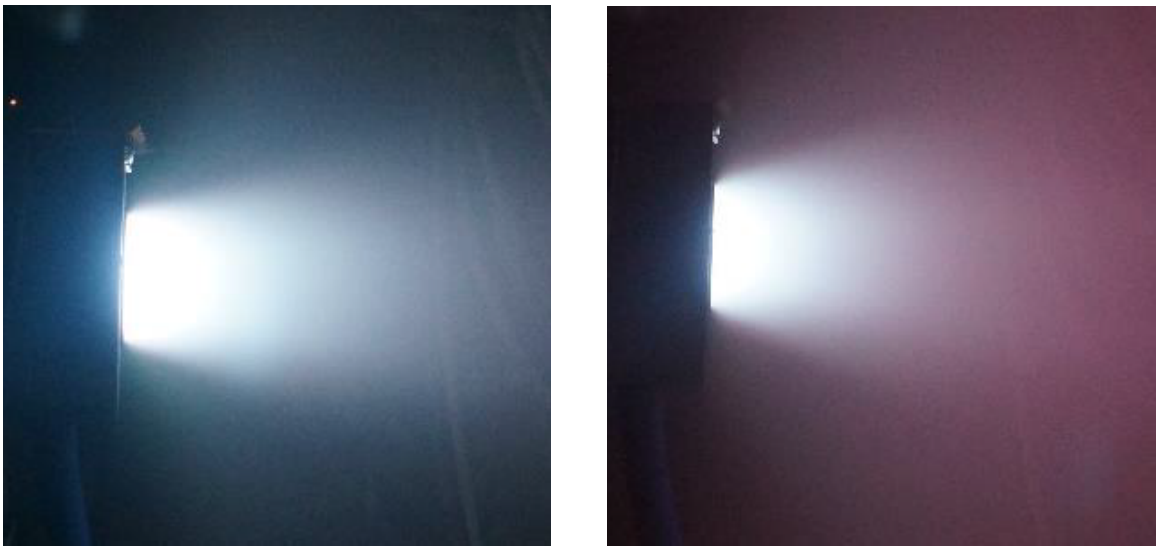

(a) (b)

Figure 4.4: ECR Thruster operating at 30 W, 1 sccm with a background pressures of (a) 1.25 μtorr and (b) 16 μtorr

4.2.4.1 Neutral density in source and plume

We calculate neutral density in the discharge region using the COMSOL Multiphysics Free Molecular Flow solver. We use a simplified axisymmetric model of the thruster and vacuum chamber to generate a mesh and subsequently solve for the neutral density at each point within the thruster and chamber. We then average over the densities within the source to obtain n_g. The simulations predict that for one sccm xenon, the average neutral density within the thruster is $n_g = 6.8 \times 10^{18}$. An approximate calculation for n_g can be performed using a 0D particle balance model: $\dot{m}/m = n_g v A$, where m is the atomic mass, v is the bulk velocity of particles exiting the throat, and A is the throat area. Here, we expect v to be between the velocity predicted by free molecular flow, $\sqrt{k_B T/2\pi m}$, and that predicted by sonic flow, $\sqrt{\gamma k_B T/m}$. Using a standard temperature of $T = 300$ K, we calculate that n_g predicted by our simulation is approximately halfway between these values.

We approximate neutral density, which includes contributions both from the plasma source and the background gas, as constant throughout the chamber (and

therefore plume region). This approximation is justified by the relatively high (> 50%) mass utilization efficiency predicted by our model, meaning that most neutrals coming from the thruster are produced during recombination on the chamber walls. The neutral densities derived from our pressure measurements are shown in Table 4.1.

Table 4.1: Neutral density in the plume, $n_{g(plume)}$

Pressure, μTorr	$n_{g(plume)}$, m^{-3}
0.98	3.15×10^{16}
13	4.18×10^{17}
26	8.37×10^{17}

4.2.4.2 Microwave power coupling

As a preliminary analysis, we investigate how background neutral density can affect RF power coupling to the plasma. To this end, we measured the forward and reflected microwave power as a function of facility pressure. These measurement techniques are given in Chap. 3. We translate these measurements to reflection coefficients in Fig. 4.5. Here, the microwave reflection coefficient, $|\Gamma|^2$, is defined as $|\Gamma|^2 = P_{Refl}/P_{Fwd}$, where P_{Fwd} and P_{Refl} are the incident and reflected powers, respectively. From here, we can calculate the load impedance using $\Gamma = (Z_L - Z_0)/(Z_L + Z_0)$, where Z_0 is the coaxial cable impedance, 50 Ω. We ultimately see that the that the load impedance, Z_L, varies by less than 4% over the conditions tested, indicating that plasma loading remains relatively unchanged for the range of background pressures produced in the experiment. This is physically intuitive as the neutral density in the source is an order of magnitude higher than in the plume and thus is expected to be relatively impervious to the variations in the lower density plume.

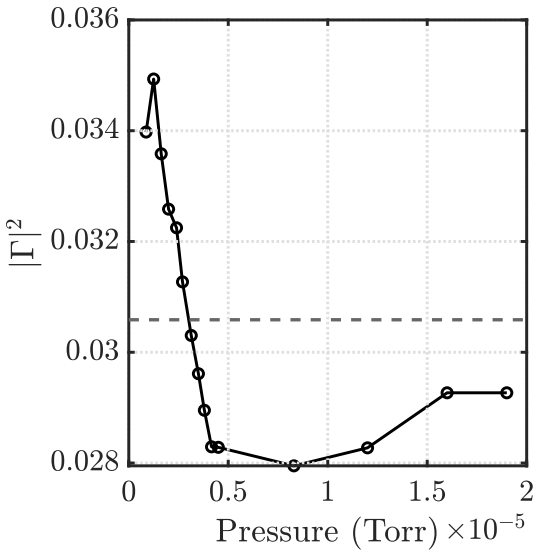

Figure 4.5: Microwave power reflection coefficient, $|\Gamma|^2$, measured as a function of chamber background pressure

4.2.4.3 Ion VDF measurements

In this section, we present our measurements of ion velocity and acceleration along thruster centerline as functions of facility pressure. Typical shapes of the IVDFs we measured in the near and far-field of the nozzle are shown in Fig. 4.6. Here, we have overlaid a fitted skewed-Gaussian distribution that we use for determining most probable velocities and calculating error. In the near-field, the IVDF for all background pressure conditions is characterized by a single, well-defined peak indicative of a near-mono-energetic drifting population. Moving downstream, the IVDFs differ in shape between the low and high pressure conditions. The low pressure (0.98 μTorr) IVDFs maintain a single, well-defined peak throughout the plume. The higher pressure cases, on the other hand, exhibit a broad, non-Maxwellian IVDF downstream of the exit plane. We can still observe a high velocity peak, reflecting an acceleration of the bulk ion population. However a second peak forms around 2,000 m/s. Between these two peaks, we observe a spreading of the accelerated population to lower velocities. The stationary population and low energy tail of the accelerated ions are indicative of ions

that are created at different positions in the nozzle and therefore experience different levels of acceleration. This is indirect evidence of downstream ionization or charge exchange collisions between ions and neutrals.

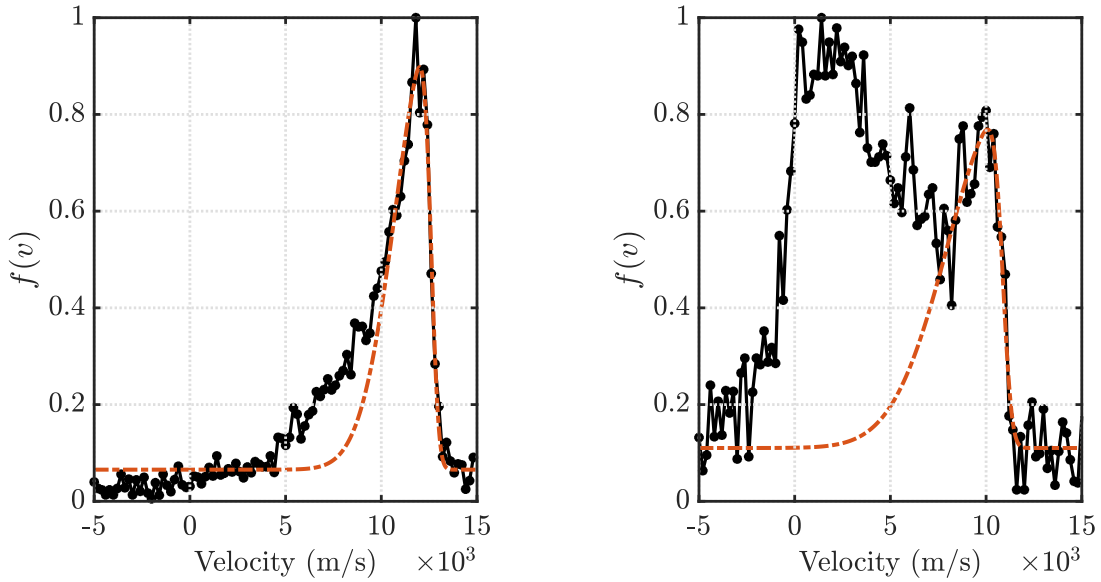

Figure 4.6: Axial ion velocity distribution function traces along center-line for the 13 μTorr condition at (a) exit plane of the thruster, and (b) 85 mm downstream of the exit plane

Fig. 4.7 further supports the idea that this lower energy population can be attributed to inelastic collisions in the plume. In these figures, we show the spatially-resolved LIF data as intensity plots where the VDFs are normalized to unity for each axial position. In these three cases, the power to the thruster remained the same, 20 W, but the facility pressure was increased from 0.98 to 26 μTorr-Xe. The data show that ion acceleration takes place over the region spanning from the exit plane to roughly 100 mm downstream. The overall shape of the acceleration profile is similar for the three pressures tested. However, the signal-to-noise ratio decreases by a factor of two as pressure is raised, and the low energy population becomes increasingly evident—suggesting more ions are being created in the plume at higher background

pressures. Moreover, in all three cases, although the ion velocity asymptotically approaches a maximum downstream, the final value decreases with increasing pressure. This reduction in maximum achievable directed kinetic energy is consistent with the observations reported in Ref. [117].

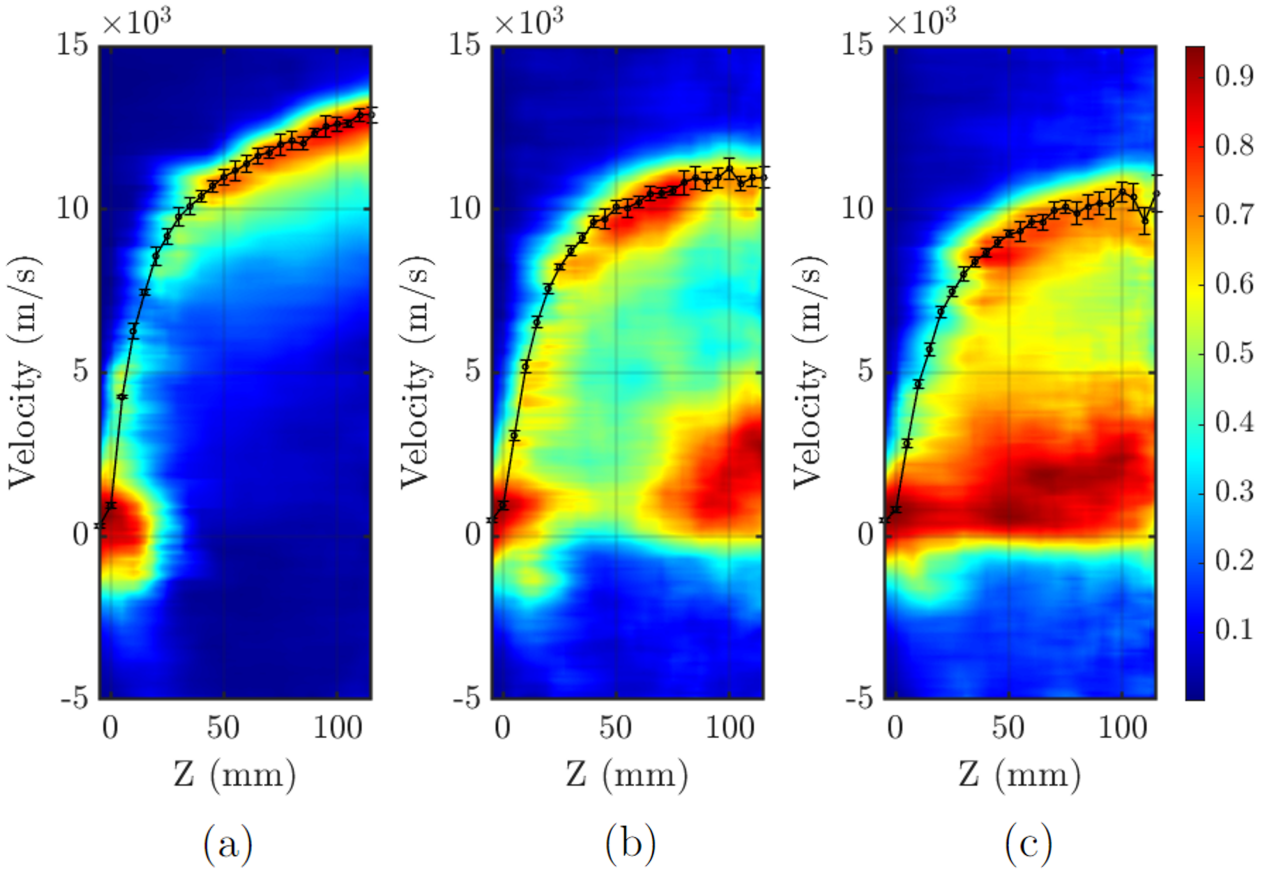

Figure 4.7: Xe II velocity distributions along thruster axis at (a) 0.98 μTorr, (b) 13 μTorr, and (c) 26 μTorr background pressure conditions. The colorbar represents the collected light intensity with peak intensity normalized to 1 for each axial position, and values are interpolated between data points. Distances are measured from the thruster exit plane

We convert the intensity maps in Fig. 4.7 to a single metric for ion acceleration by calculating the most probable velocity of the ions at each spatial location. To this end, we fit a skewed-Gaussian distribution to the high-velocity population in each IVDF and assigned the mean value to the drift speed, as shown in Fig. 4.6. The uncertainty

in these drift values, in turn, was determined by re-sampling and curve fitting each IVDF using a boot strapping method. Following this technique, we show in Fig. 4.8 the resulting values of ion speed and ion kinetic energy, $\varepsilon_i = 1/2 m_i u_i^2$. Here we can see explicitly the direct impact of increasing pressure. As pressure increases from 0.98 to 26 μTorr, ion velocities decrease by $\sim 20\%$ from 12.8 to 10.2 km/s, correlating to a decrease in ion energy of $\sim 37\%$ from 111.5 eV to 70.4 eV.

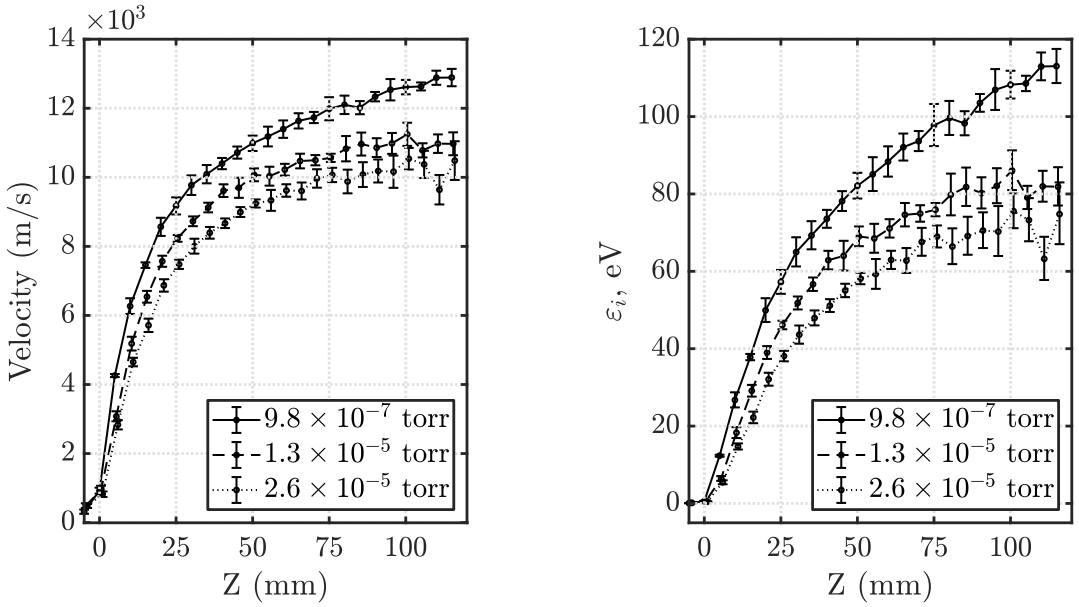

(a) (b)

Figure 4.8: (a) Most probable velocity of accelerated ions, (b) ion energy deduced from LIF data as measured from the exit plane of the thruster.

4.2.5 Power lost to electron-neutral and CEX collisions

The key remaining unknowns affecting power losses within the magnetic nozzle are the electron temperature, T_e, the plasma density, n_e, and the energy lost per electron at the throat, $\varepsilon_{e(t)}$. To estimate these values experimentally from our available data, we make a few key additional assumptions. First, we assume that 100% of the power input to the thruster (20 W) is absorbed by the plasma. Though this is an overestimate, given the low reflected powers seen during the experiment (Sec. 4.2.4.2), the

actual value may be close to this number. Additionally, as we discuss in Sec. 4.2.6, the final ion velocities predicted by our model are independent of absorbed power, so long as $Q_{e(e)}$ is constant. Second, we take $Q_{e(e)}$ to be zero in the model, corresponding to an open boundary condition with thermalized electrons at the detachment point [37]. This is justified for our experimental setup by noting that the thruster's position is several acceleration region lengths from the nearest vacuum chamber walls [62]. Finally, we use a CEX cross section of $\sigma_{cex} = 8.73 \times 10^{-19}$ m^2 corresponding to ~ 1 eV ions. Because σ_{cex} monotonically decreases with ion energy, this represents an upper bound for P_{cex}. Armed with these assumptions and the measurements of ion velocity, neutral density, and power coupling, we can evaluate the expressions given by Eqs. 4.1-4.13 to determine the power fluxing into the throat and the power lost to electron-neutral and CEX collisions. We show these values in Table 4.2. We also plot the relative power consumed by CEX and inelastic electron-neutral collisions in Fig. 4.9. It is worth clarifying here that the electron temperature is unaffected by background neutral pressure as the energy fluxing to the thruster exit plane is unaffected by downstream losses and the neutral density within the thruster is nearly independent of background pressure.

Table 4.2: Plasma properties and collisional power consumed in the plume for the background pressures tested

P, μTorr	T_e, eV	$\varepsilon_{e(t)}$, eV	n_e, m^3	$\dot{m}_i$, kg/s	P_t, W	P_{cex}, W	P_{ec}, W
0.98	10.6	113.8	3.06×10^{17}	5.36×10^{-8}	5.53	2.45×10^{-5}	0.09
13	10.6	111.9	3.07×10^{17}	5.38×10^{-8}	5.47	5.84×10^{-5}	1.22
26	10.6	132.2	2.95×10^{17}	5.18×10^{-8}	6.03	8.80×10^{-5}	2.35

From these calculations, we can observe that over a third of the power entering the throat is consumed by electron-neutral collisions within the plume as pressure rises above 20 μTorr, while no significant power losses can be attributed to ion-neutral CEX collisions. More realistic cross sections for the CEX collisions at higher energies would yield even lower values for P_{cex}, further confirming this point. This suggests

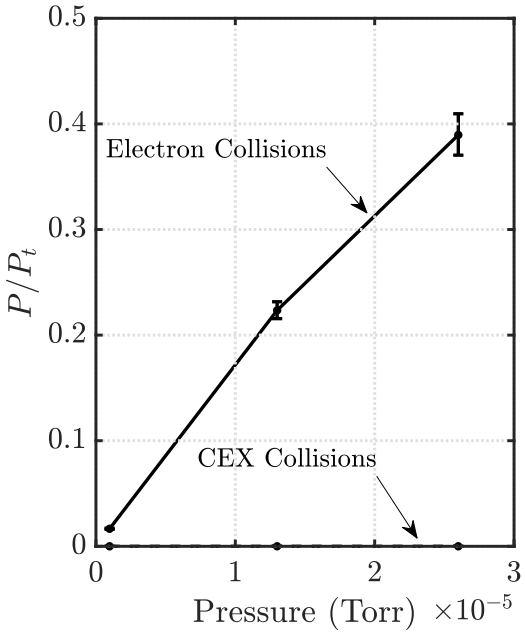

Figure 4.9: Relative powers consumed by electron and CEX collisions

quantitatively that electron impact ionization and excitation play the leading role in downstream power consumption, with values comparable to the total energy leaving the nozzle.

4.2.6 Comparison with Energy Loss Model

In this section, we explore the predictive capabilities of the model we presented in Sec. 4.2.2 by using the data from a single operating condition to predict the ultimate ion velocities for a range of background pressures. In our analysis, we use the data from the lowest background pressure measurements. This data point was chosen due to its high signal to noise ratio but is otherwise an arbitrary choice. The velocity and pressure measurements for this single point inform the value of $\varepsilon_{e(t)}$ in our model, which we then hold constant over all background pressures. This is equivalent to assuming that changes in the plume do not affect the discharge upstream of the throat. The data in Table 4.2 show that this assumption may break down at high

background pressures. However, as we show in the following, our model has good first order agreement.

Rearranging Eq. 4.1, we can relate accelerated ion energy to normalized power losses in the plume, $\frac{P}{P_t}$, where P_t is the power entering the throat:

$$\varepsilon_{i(e)} = \frac{m_i}{\dot{m}_{i(e)}} P_t \left(1 - \frac{P_{ec}}{P_t} - \frac{P_{cex}}{P_t} - \frac{Q_{e(e)}}{P_t}\right) - \frac{5}{2} T_{e(e)}. \tag{4.14}$$

Using this relation, we can calculate predicted ion energies with respect to normalized power losses, $\frac{P_{loss}}{P_t}$, where $P_{loss} = P_{ec} + P_{cex}$. Again, we assume that the electron heat flux at the end of the plume, $Q_{e(e)}$, is zero. These results are plotted in Fig. 4.10a. Here, we have overlaid the data at each background pressure presented in Table 4.2 with error bars generated by the uncertainties in the LIF measurements.

Fig. 4.10a shows that the final ion energies scale roughly linearly with power consumed by plume collisions, as is predicted by Eq. 4.1. This is a direct initial confirmation that the loss in electron energy that stems from collisions with these species may be sufficient to explain the degradation in performance of the nozzle with pressure. With that said, this conclusion is subject to a number of simplifying assumptions about the value of P_{loss}/P_t, as well as the other parameters governing Eq. 4.1. To test the rigor of our result, we therefore relax these assumptions parametrically to determine the sensitivity of our results to these assumptions.

We do this sensitivity analysis in three ways. First, we examine the role of neutral gas density in the thruster, n_g, as we have made the simplifying assumption that this is constant and can be estimated from a numerical model. We allow this value to vary by +/-50%. Second, we allow the electron temperature within the plume, $T_{e(plume)}$, to vary by +/-50%. This is an important parameter to consider as we were not able to measure it directly in the near-field region of the plume and it is critical to the ultimate acceleration process of the thruster. Third, we vary the electron heat flux at

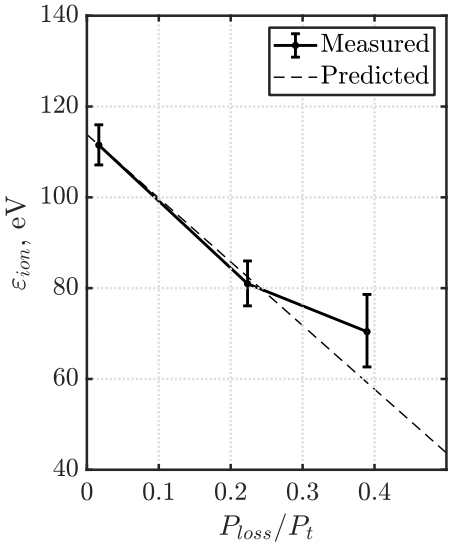

(a) $\varepsilon_{i(e)}$ vs P_{loss}/P_t predicted by Eq. 4.14 using data taken at 0.98 μTorr and measured accelerated ion energy

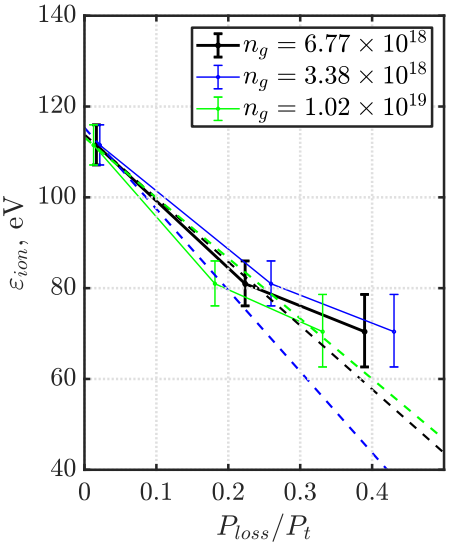

(b) Primary discharge neutral density, n_g, swept from +/-50% nominal

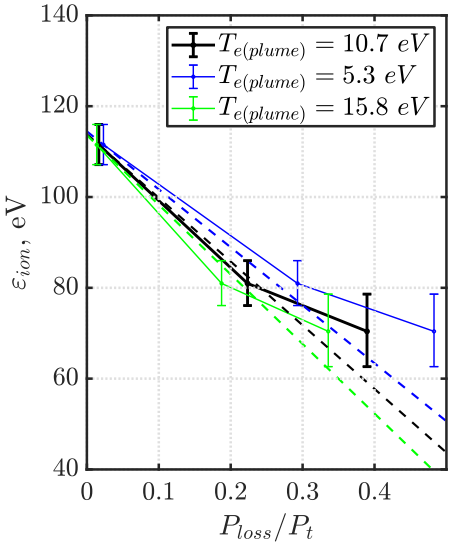

(c) Electron temperature within the plume, $T_{e(plume)}$, swept from +/-50% nominal

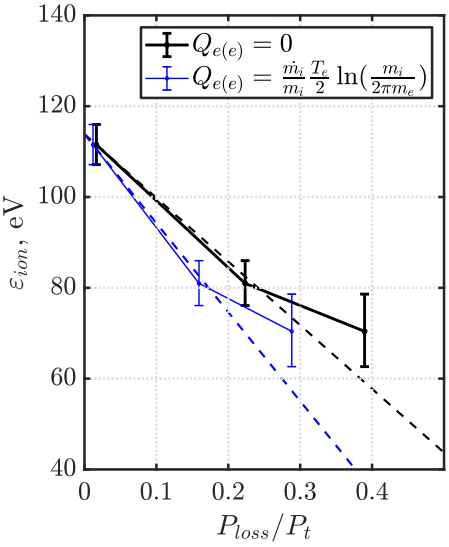

(d) Electron heat flux at the exit of the acceleration region, $Q_{e(e)}$, swept from 0 W (open boundary) to $\frac{\dot{m}_i}{m_i}\frac{Te}{2}\ln\frac{m_i}{2\pi m_e}$ W (sheath boundary)

Figure 4.10: Measured and predicted ion velocities for P_{loss}/P_t ranging from 0 to 0.5, including sensitivity analysis of n_g, $T_{e(plume)}$, and $Q_{e(e)}$

the nozzle exit, $Q_{e(e)}$ from 0 to $\frac{\dot{m}_i}{m_i}\frac{Te}{2}\ln\frac{m_i}{2\pi m_e}$, corresponding to an open boundary and sheath boundary condition, respectively. Arguably, the electron heat flux is one of the least understood and hardest parameters to measure in these devices. We elect to employ these two boundary conditions as they represent the extremes in the values of this flux. We note that we forgo a sweep of P_{abs} as it can be shown that both $P_t/\dot{m}_i$ and P_{loss}/P_t are independent of P_{abs}. Thus for a fixed $Q_{e(e)}$ and $T_{e(e)}$, $\varepsilon_{i(e)}$ is independent of P_{abs}.

With this in mind, we recalculated P_{loss}/P_t over each pressure condition and updated the output of Eq. 4.14 using the new input parameters. The results of these calculations are shown in Figs. 4.10b-4.10d. For each of these figures, the non-swept parameters are held at the conditions shown in Table 4.2. From these figures, we can observe that in all three cases, although the data and model shift (most prominently with discharge region neutral density), the agreement between the two is relatively insensitive to the changing assumptions. This suggests that the conclusion that the loss in ion energy can be attributed to electron-neutral collisions still holds.

4.2.7 Discussion of Background Pressure Effects

We discuss in the following key assumptions and potential sources of error underlying our analysis and the implications of our results in the context of facility effects and previous work.

4.2.7.1 Key assumptions

1. Free-fall diffusion in main discharge: The free-fall diffusion profile, given in Ref. [70], neglects the effect of the applied magnetic field, which likely acts to inhibit diffusion to the radial walls. This would cause the model to overestimate T_e and thus underestimate n_e. However, given the approximately linear behavior of K_{iz} and K_{ex} for the electron temperature range of interest ($T_e < 25$ eV), we

expect that P_{loss}/P_t in the plume will remain roughly constant for small changes in the T_e and n_e.

2. No neutral depletion: By neglecting neutral depletion, we have artificially raised the predicted neutral density within the thruster (n_g). Because of the relatively high ionization fractions predicted by the model ($\sim 5\%$), this negation leads to a low estimate of T_e and thus a high estimate of n_e. For small changes in n_g, this has minimal effect of P_{loss}/P_t. However at large ionization fractions ($> 50\%$), these effects can significantly alter predicted plume losses, as shown in Fig. 4.10b.

3. Ions reach Bohm speed at thruster exit: Our primary discharge model assumes that ions reach the Bohm speed at the thruster exit. Measurements on our device and previous studies have shown that this throat location is, in fact, several millimeters downstream of the thruster exit [27]. Collard and Jorns have suggested that this effect is largely due to collisions with neutrals and is a source of inefficiency in magnetic nozzles. We have shown quantitatively how this might be the case. However, because of the complex diffusion dynamics at the open end of the thruster, it is unclear how, exactly, this would affect the main discharge. One challenge moving forward would be to link the location of this sonic transition to the collisional loss term. This is done in traditional nozzles where non-adiabatic and non-isentropic flow move the choking point downstream of the physical throat.

4. Plume expansion with magnetic field lines and isothermal electrons: The choice of plasma expansion with the magnetic field and isothermal electrons gives us a first order approximation for collisional power consumed in the plume. While this neglects several of the more complex electron cooling and diffusion processes that occur in magnetic nozzles, the sensitivity analysis presented in Fig. 4.10c

shows that our loss model is largely unaffected by plume electron temperature. This is due to the plasma density in the plume scaling inversely with plume electron temperature, partially offsetting the changes in K_{iz} and K_{exc}.

5. Electron temperature unaffected by downstream ionization: By keeping the main discharge electron temperature independent of plume collisions, we have assumed that relatively few electrons generated downstream of the throat drift into the main discharge region. Relaxing this assumption would lead to a lower electron temperature in the discharge as cool electrons back-stream into the thruster. This would in turn lower the acceleration potential as each ion-electron pair exiting the throat carries less energy into the nozzle. Fully capturing this phenomenon requires a more complete picture of electron heat flux in the nozzle, and we therefore do not include these effects in our model. However, it should be noted that previous measurements of the thruster's floating potential showed decreases in the magnitude of the floating potential (with respect to chamber walls) that were greater than corresponding changes in ion energy [121]. This is perhaps indicative of decreased electron temperature inside the thruster at higher background pressures.

6. Neglect of role of boundary conditions: Finally, it is possible that additional facility effects, such as secondary electrons emitted from the chamber walls, can influence plume dynamics. This can give rise to non-thermalized distributions that fundamentally impact the electron thermodynamics and heat flux. An investigation of these effects is beyond the scope of this dissertation. With that said, while the good agreement of our global model with experimental measurements would suggest that these other facility effects may not have had a substantial contribution over our range of studied pressures, these effects ultimately may have a more prominent role as pressures are reduced or smaller

facilities are employed. We explore these boundary condition effects further in Sec. 4.3.

4.2.7.2 Implications for thruster testing standards and extrapolation to on orbit performance

The key finding from our investigation is that it is inelastic electron-neutral collisions in the plume with facility neutrals that adversely impact magnetic nozzle thruster performance. This indicates that collisionless models of magnetic nozzle acceleration regions, such as those presented in Refs. [7; 62; 29], can accurately describe plume dynamics only for very low background pressures. Having identified a potential cause and validated a model for this effect, we now can turn to the key question of how a thruster will behave in a relevant, space like environment. To this end, in our model, extrapolating to unmeasured pressures requires an expression for $\varepsilon_{e(t)}$, the energy deposited in each electron entering the throat. The study presented in Sec. 4.2.6 holds $\varepsilon_{e(t)}$ constant across all pressures using the value obtained from our lowest pressure results. This choice was somewhat arbitrary, corresponding to the highest signal to noise ratio data gathered during the experiment. However, the results show good agreement at low pressures. It is notable that the trend with facility pressure does appear to change inflection at high pressure, indicating a potentially nonlinear response. This was not captured in our model and could perhaps be attributed to feedback effects such as electron thermalization becoming more important at these higher pressures. With this in mind, at least at lower pressures where there is better agreement between model and experiment, this work suggests a recommendation for how ground tests in the future may be extrapolated to orbit. Most notably, we see that the deviation scales linearly with neutral density. This indicates that we may be able to extrapolate to zero pressure by fitting a line. For example, our current results suggest that ions would achieve a kinetic energy of $\sim$ 120 eV on orbit. While we

were able to capture some of the effects of background pressure using these relatively simeple models, future studies into these types of effects could include the role of cross-field diffusion within the magnetic nozzle, which is likely enhanced at higher pressures.

4.3 Role of Chamber Walls in ECR Thruster Performance

In this section, will briefly touch upon the effects of conductive vacuum chamber walls on thruster performance. These walls in theory can provide conduction paths for neutralization of the plume that would not exist on orbit. Furthermore, the presence of downstream surfaces can effect upstream electron dynamics due to the bouncing motion of electrons within the plume. Previous ECR experiments by *Peterschmitt* [92] (see Fig. 80) using the same thruster in two different vacuum chambers provided some evidence that larger chamber sizes could lead to increased thruster performance, though the exact mechanisms by which this may occur remain unknown.

4.3.1 Experimental Setup for Testing Chamber Wall Effects

In order to test the effects of chamber size, we mounted a modified version of the ECR II thruster in the Large Vacuum Test Facility (LVTF) at PEPL, as shown in Fig. 4.11. This chamber measures 6 meters in diameters and 9 meters in length and features roughly 600,000 l/s pumping speed on xenon. More details on LVTF are provided in Ref. [119]. The thruster was mounted roughly on chamber center-line approximately 4 meters away from the downstream graphite beam dump. Compared to the Junior test facility, the walls were approximately six times as far from the thruster.

During the experiment, a 1 meter by 1 meter stainless steel foil panel was added to the rotating motion stage in LVTF, allowing for the addition of a downstream conducting surface that could act as a simulated chamber wall. The panel was elec-

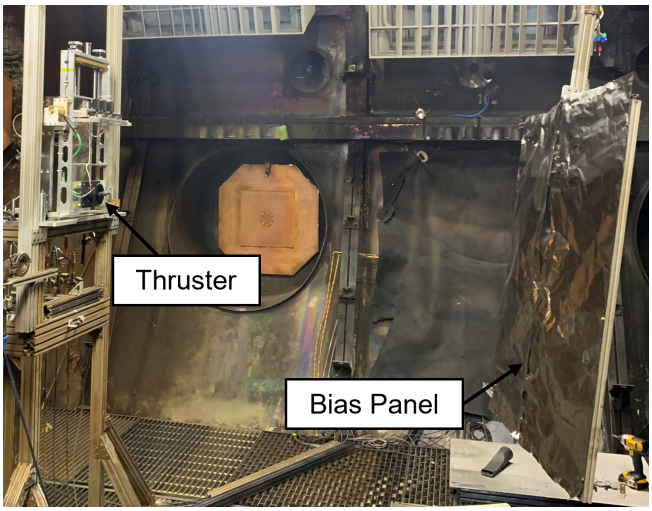

Figure 4.11: ECR thruster mounted in LVTF with stainless steel bias panel positioned downstream of the thruster to simulate varying chamber size.

trically isolated from the chamber walls and attached to an external DC power supply and ammeter thus enabling it to act as a large planar electrostatic probe. We show an electrical schematic of the setup in Fig. 4.12.

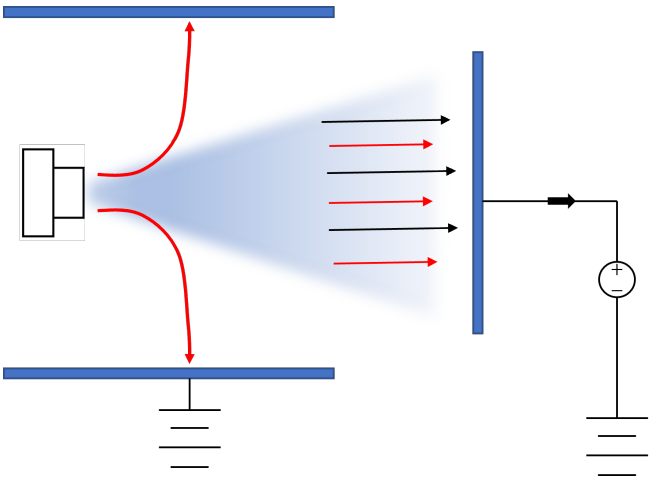

Figure 4.12: Schematic diagram of the thruster in LVTF showing the chamber walls (top and bottom blue rectangles) and the foil bias plate (right blue rectangle). The nominal electron (red) and ion (black) trajectories are shown in the plume. The net current through the ammeter is shown as the thick black arrow.

4.3.2 Chamber Size Experimental Results

Figure 4.13 shows the measured thrust and efficiency versus power for three different panel positions: no panel, 1.7 meters downstream of the thruster, and 0.7 meters downstream of the thruster. In these tests, the panel was tied to chamber ground through the external ammeter. The flow rate was set to 1 sccm xenon with the absorbed power swept from 20 to 26 watts at 2450 MHz. The chamber pressure, as measured at the chamber wall by a Stabil ionization gauge, was between 3×10^{-7} and 5×10^{-7} torr-xenon during thruster operation. For the no panel data points, the panel was positioned to the side of the thrust stand, ideally minimizing its influence. We show the measured current through the ammeter in Fig. 4.14.

The force measurements show a modest increase in thrust when the panel does not interfere with the plume. However, the thrust does not change substantially when the panel distance decreases. Interestingly, the current measured through the panel is positive when it is positioned in the plume indicating that it is ion-collecting when at chamber wall potential. When it is positioned to the side of the thruster, however, the measured current is negative. This indicates that there may exist a current path in the chamber walls through which electrons ejected at wide angles can neutralize downstream ions.

Biasing the downstream panel provides some indication of the influence of chamber walls on the thruster operation. Figure 4.15 shows the results of sweeping the panel potential from -200 to 200 volts while it is positioned 0.7 meters from the thruster exit plane. While not shown here, thrust measurements taken at -200 and 200 volts showed less than 2% change in thrust. The thruster body floating potential shows that, when the panel is in an electron collecting mode, the potential structure in the plume will adjust itself so that the thrust maintains a set voltage with respect to the downstream panel. Thus it is possible that once the plasma detaches from the magnetic field lines it can adjust to accommodate the downstream boundary

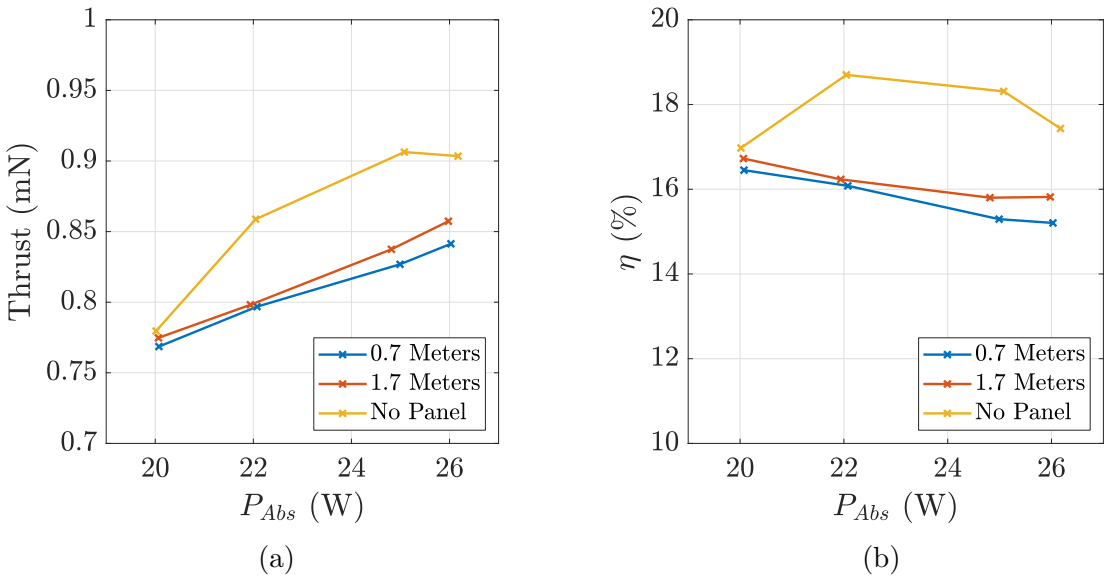

Figure 4.13: (a) Thrust and (b) efficiency versus power for the grounded conducting panel in three different positions. The flow rate was held at 1 sccm xenon for all data points.

conditions without affecting thruster performance.

While these experiments seem to indicate that there is some dependence between the wall position and thruster performance, it is difficult to draw any firm conclusions from these data. Because the flow rates used in testing were so small compared to the high pumping speed of the test facility, the majority of the background pressure seen in testing was due to chamber outgassing and not residual propellant. It was therefore difficult to maintain a constant pressure while testing as facility outgassing rates fluctuated. Furthermore, it is possible that the addition of a downstream barrier had the effect of increasing neutral density within the plume as ions neutralized at the bias plate drifted back towards the thruster. Because of these effects, the results do not discount the possibility that pressure differences account for much of the performance changes seen in testing.

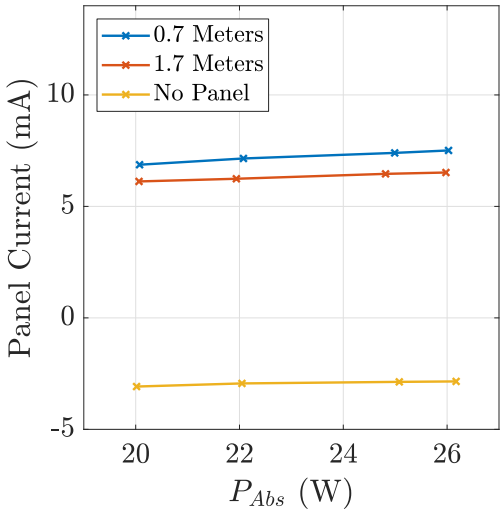

Figure 4.14: Panel current versus power corresponding to the thrust measurements in Fig. 4.13.

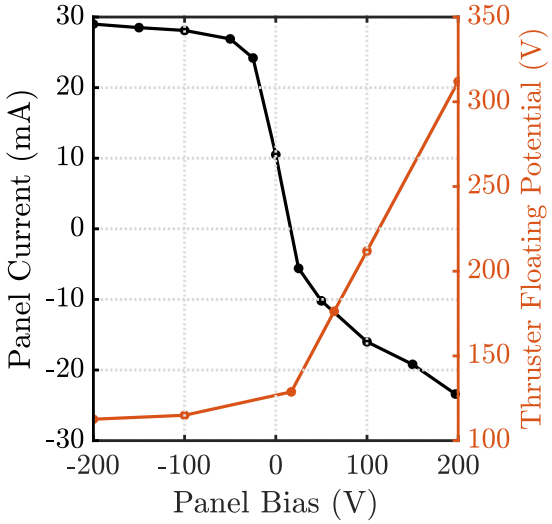

Figure 4.15: Panel current and thruster body floating potential versus bias voltage for the panel located 0.7 meters from the thruster exit plane.

4.4 Summary

In an interesting departure from state-of-the-art EP devices such as Hall thrusters, which show a general improvement in performance with increased facility pressure, magnetic nozzle performance decreases with background neutral density. In this chapter, we have demonstrated that this degradation in performance largely can be attributed to electron-neutral collisions within the plume that significantly reduce the amount of power available to accelerate ions through the diverging magnetic nozzle. By raising the background pressure from 0.98 μTorr to 26 μTorr, we calculated that 39% of the power entering the plume, in the form of both ion inertia and electron pressure, is consumed by ionization and excitation collisions. Physically, these collisions remove the critical thermal energy introduced to the electrons in the source region before it can be successfully converted to kinetic energy of the ions. Our calculations for how the loss in energy scales with facility pressure are commensurate with our LIF measurements, which show a broadening of ion VDFs and a reduction in accelerated ion energy of 37%. We further demonstrated that, while currents exist in chamber walls during on-ground testing, their effect on thruster performance may be overshadowed by pressure effects. Practically, our results have two major implications for the field. First, these findings suggest that collisionless models must be augmented to accurately describe plume dynamics in thrusters operating in finite background pressure conditions [7; 62; 29]. Second, we have found that at low densities, the dependence of ion velocity on pressure is linear. This suggests a potential future strategy for mapping ground based tests to on orbit behavior.

CHAPTER V

Optimization Experiments Using Custom Waveforms

5.1 Introduction

Having explored best practices for thruster testing, we now turn to optimizing thruster performance. In this chapter we present the setup and results of an experimental campaign seeking to optimize the performance of the ECR thruster by changing the input microwave waveforms. Specifically, we explore the effects of single frequency tuning, the addition of a second input frequency, and the effects of pulsing the microwave power. We use direct thrust measurements (described in Chap. 2) paired with a surrogate-based optimization algorithm to increase the thruster's efficiency.

Previous parametric experiments have shown that small changes to thruster geometry can have substantial effects on overall performance [117; 101]. These studies additionally have found that the changing the thruster wall material can further increase thrust [117; 92]. Similarly, changes in the magnetic field topology can improve the the thruster's efficiency [116]. Given the lack of predictive models for these types of thrusters, there is no reason to believe that these devices cannot be improved further through modification of these factors.

However, changing these physical parameters often comes at a great cost both in terms of testing time and fabrication expenses. As such, it is highly desirable to find design variables that do not require physical changes be made to the thruster geometry. One potential avenue for improving ECR performance that we will explore in this chapter is to manipulate the power conditioning of the microwave input power. These techniques have been employed extensively in the design of ECR ion sources for highly charged ion production and ECR plasma processing chambers but have been largely untouched in EP [39; 77; 99; 89; 127; 18].

The three waveform manipulation techniques we explore in this chapter are single-frequency tuning, two-frequency tuning, and pulsed modulation. In single-frequency tuning, described in Sec. 5.1.3, we attempt to optimize thruster efficiency by shifting the input frequency between 1050 and 2500 MHz. Physically, this moves the resonance zone back and forth within the thruster and changes the wave propagation properties as the input frequency approaches the plasma cutoff frequency. This technique has been previously attempted in an ECR thruster with a very limited input frequency range (2300-2600 MHz) [116].

Two-frequency tuning, described in Sec. 5.1.4, mixes waves with two different frequencies before injecting them into the thruster. This adds a second resonance zone to the thruster, giving electrons two locations to undergo resonant heating. This technique is commonly applied in ECR ion sources to boost highly charge state ion production, but has not yet been applied to thrusters [89; 127].

Using pulsed power, described in Sec. 5.1.6, allows the thruster to break free of normal limitations that stem from 0D power balance. This enables transient plasma properties, i.e. high electron temperatures and densities, that cannot be supported in steady state. Pulsed techniques are common in plasma processing but have not been applied to low power magnetic nozzle thrusters to date [39].

One of the major challenges with adopting this approach to optimization is the

dimensionality of the problem. Without complete models of the underlying physics, optimization requires a gradient-free approach. With only two free parameters, exploring the design space can require tens or hundreds of sample points. Thus the need is apparent for tools that can more efficiently test each design point. In Sec. 5.1.2, we describe the algorithm used in choosing each new test point during our experiments.

This Chapter is organized as follows: in Sec. 5.1.1, we describe the general optimization procedure used for each experiment. Section 5.1.2 describes the optimization algorithm used in the experiments. Sections 5.1.3-5.1.6 describe the setup and results of each of the optimization techniques, and in Sec. 5.2 we provide an analysis of the experimental results.

5.1.1 Optimization Procedure

The experimental campaign presented in this chapter seeks to optimize the thruster's efficiency, η, defined as $\eta = T^2/(2\dot{m}P_{Abs})$, where T is the measured thrust, $\dot{m}$ is the propellant mass flow rate, and P_{Abs} is the power absorbed by the thruster, as described in Sec. 3.6.2. For the purposes of this campaign, we restricted each experiment to use a constant absorbed power and mass flow rate, thus making the microwave waveform the single varying parameter for each test. The tests were performed using the ECR II thruster, described in detail in Sec. 3.2.2.

The overall optimization scheme can be described as follows: an optimization algorithm selects a new test point (i.e. frequency or pulse width). This test point is fed to the thruster control program which transitions the thruster to this operating point. When the thruster reaches steady state, the control program initiates a thrust measurement. Once the thrust measurement is complete, the thrust and power data are fed back to the optimization algorithm. The optimizer then processes the data and selects a new test point (see Fig. 5.1). The optimization process terminates when the user manually ends the program.

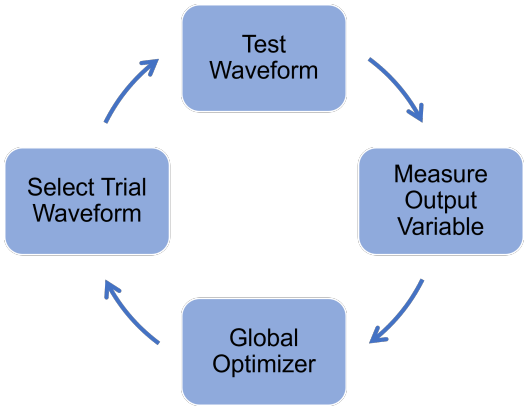

Figure 5.1: General optimization procedure.

For our experiments, we use a LabVIEW program to control the thruster set point and automate thrust measurements. The program features a PID control function to maintain constant power to the thruster. The LabVIEW program is set up to communicate with an optimizer running in parallel allowing for closed-loop optimization experiments.

We begin each test by measuring thrust at a default low-power operating point (typically ~ 7 W at 2400 MHz). During the optimization process, we measure only the difference in thrust between the test point and a default low-power operating point. By measuring changes in thrust, as opposed to taking absolute thrust measurements, we are able to keep the plasma lit throughout the experiments. This avoids thruster re-starts, which typically take several minutes.

We transition between test points using an automated sequence during which the thruster is kept in a powered on state to avoid time consuming restarts. Each modulation scheme requires a unique transition procedure to keep the thruster stable while switching test points. We provide the specific procedures for each optimization experiment in Sec. 5.1.3-Sec. 5.1.6.

The average time per test point, including transitioning to a new point, settling time, and thrust measurement, is between one and two minutes. hus we are able to perform hundreds of measurements per day with minimal human intervention.

Figure 5.2 shows a single-frequency optimization experiment running in the Junior Test Facility with the LabVIEW program in the foreground.

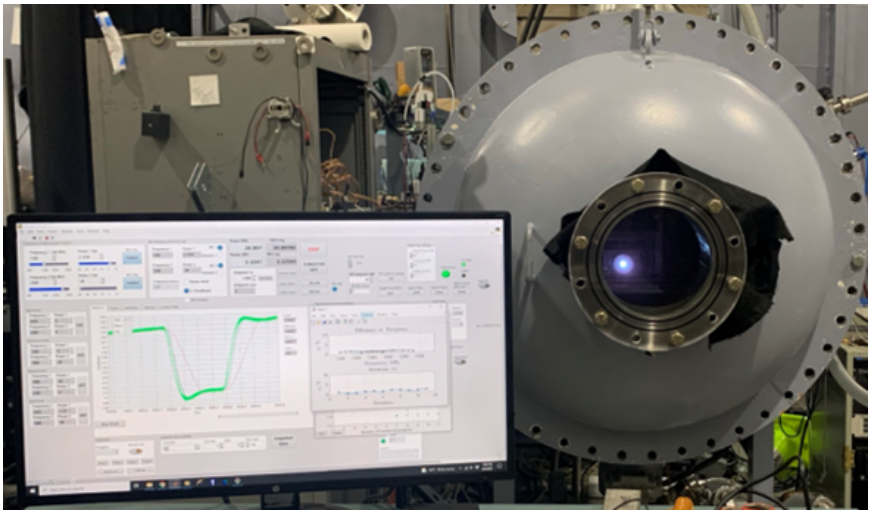

Figure 5.2: Automated optimization experiment during operation in the Junior Test Facility. The LabVIEW thruster control program is shown in the foreground.

5.1.2 Optimization Algorithm

Our experiments include single and two variable optimization problems. The shape of the output function, i.e. efficiency versus frequency, is not known a priori, and may be composed of several peaks and valleys. We therefore require a non-convex optimization algorithm (an algorithm capable exploring parameter spaces outsides of local minima) to perform the experiment. To this end, we use a surrogate-based global optimization algorithm to select each new test point.

The algorithm is implemented using the Matlab `surrogateopt` function, one of several algorithms available in the Matlab Global Optimization Toolbox. A diagram of the optimizer is shown in Fig. 5.3. The algorithm works by first randomly sampling the parameter space. The number of random samples can be selected by the user. It then builds a surrogate model of the system based on radial basis functions. At each iteration, the algorithm selects a new test point by employing a merit function based on a weighted combination of the expected improvement and uncertainty in

the model [42]. After testing a new point, the surrogate model is updated and the process repeats. The incumbent point shown in Fig. 5.3 is the prior test point with the best performance. The algorithm resets to random sampling when it predicts little improvement with each new sample point.

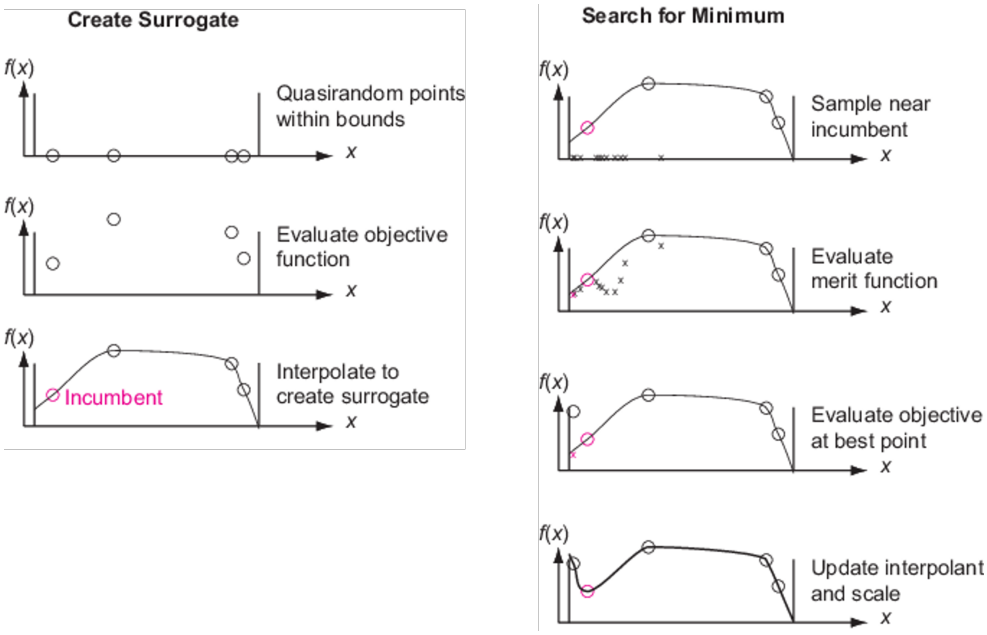

Figure 5.3: Matlab surrogate optimization algorithm. Reproduced from Ref. [1].

5.1.3 Single Frequency Optimization

The single frequency optimization experiment attempts to maximize the thruster efficiency by shifting the single input microwave frequency, f. This effectively moves the resonance zone within the thruster with higher frequencies corresponding to resonance zones closer to the back of the discharge region, as shown in Fig. 5.4. A detailed diagram of the magnetic field strength and corresponding ECR frequencies is shown in Sec. 3.2.2. For this experiment the input frequency is restricted to a ranges from $f = 1050$ MHz to $f = 2500$ MHz with the minimum frequency step set to 1 MHz. These frequency constraints are dictated largely by the amplifier and wireless power coupler bandwidths, though initial tests showed that at frequencies below 1050 MHz,

the thruster could not sustain a discharge for more than a few seconds at low flow rates.

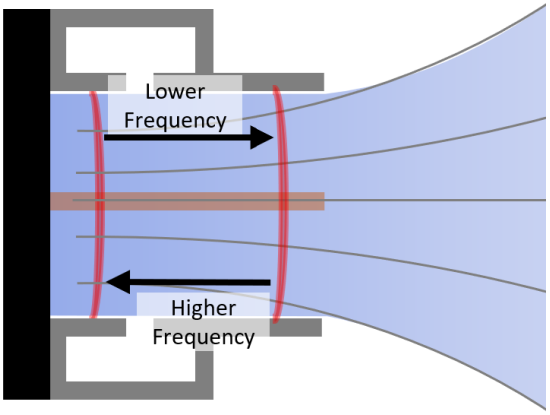

Figure 5.4: Effect of changing frequency during single frequency optimization.

We performed several tests to determine how the optimal frequency was affected by total absorbed power and flow rate. The overall test matrix included 20, 30, and 40 Watt absorbed powers with xenon flow rates set to 0.75, 1.00, 1.25, 1.50, 1.75, 2.00, 3.00, 4.00, and 5.00 sccm. The 40 Watt tests included only the 0.75, 1.00, and 5 sccm flow rates due to high reflected powers putting the coaxial cable at risk of melting.

The single frequency experiment used the following procedure: We warm up the thruster for approximately one hour until it reaches a thermal quasi-steady state. The thruster is then transitioned to a default low-power set point, typically 7 W and 2400 MHz. While the thruster is in its default state, we run the full thrust stand calibration procedure. We then measure the total thrust at the default low-power set point. After taking this data, we restart the thruster and initiate the single frequency optimization routine. The optimizer will then select a test point which is sent to the thruster control LabVIEW program. The program sends a command to the signal generator to switch to the new input frequency. A special timing mechanism is used to ensure that the plasma does not extinguish. Once at the new frequency, a software-

controlled PID loop is enabled to stabilize the thruster at the absorbed power set point. When the thruster stays within ±0.5 Watts of the desired power for a total of 5 consecutive seconds, the PID loop is turned off. The thruster is then kept at the new set point for 10 seconds to further stabilize. Finally, the thruster is transitioned back to the default set point. Thrust is measured by taking the difference between the test set point and the default set point. The thrust data is then sent back to the optimizer, and the process repeats. To avoid long-term errors caused by thermal drift, we run a thrust stand calibration procedure every 5 test points. For the experiments presented in this section, the optimizer uses 30 randomized points to begin each test.

5.1.3.1 Single Frequency Optimization Results

We show the results of a typical single frequency optimization experiment in Fig. 5.5. This plot underscores how the optimizer employs a combination of randomization and guided search to narrow on a region of optimal efficiency. The first 30 trials are randomly selected, as can be seen in the highly variable outputs. The next 20 points are selected using the surrogate optimization algorithm. At trial 48, the optimizer determined that it had reached an optimum and resets to picking random points. The experiment was manually terminated after 58 trials as it did not appear to be improving any further. This entire experiment took $\sim$ 90 minutes to run, excluding thruster warm-up time.

We show the post-processed efficiency and specific impulse for the single frequency experiments in Figs. 5.6-5.8. The uncertainty in these plots is calculated using the procedure outlined in Sec. 3.9. The large error bars correspond to data points with high values of measured reflected power. For clarity, we show only the data for the thruster operating at 0.75, 1.00, and 5.00 sccm flow rates. We provide the complete data sets, including the 1.25, 1.50, 1.75, 2.00, and 3.00 sccm data in App. C.

The data show that at low flow rates, the optimal frequency tends to be $f_{optim} \approx$

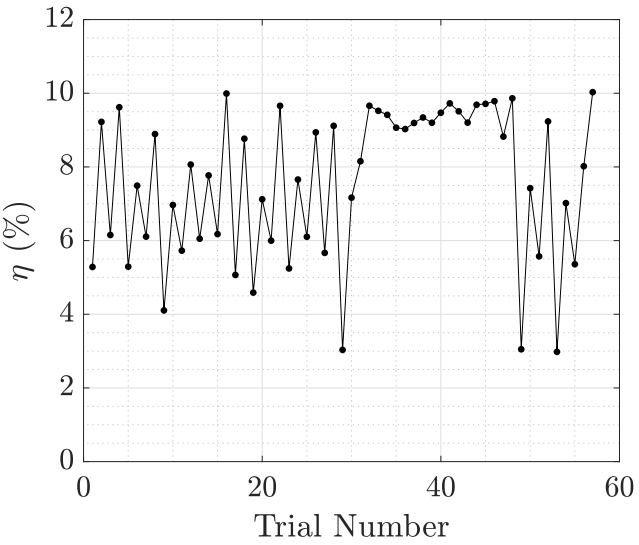

Figure 5.5: Example of a single frequency optimization experiment showing the measured efficiency vs. trial number. The first 30 points are randomly selected while the remaining points are chosen by the the surrogate optimization algorithm.

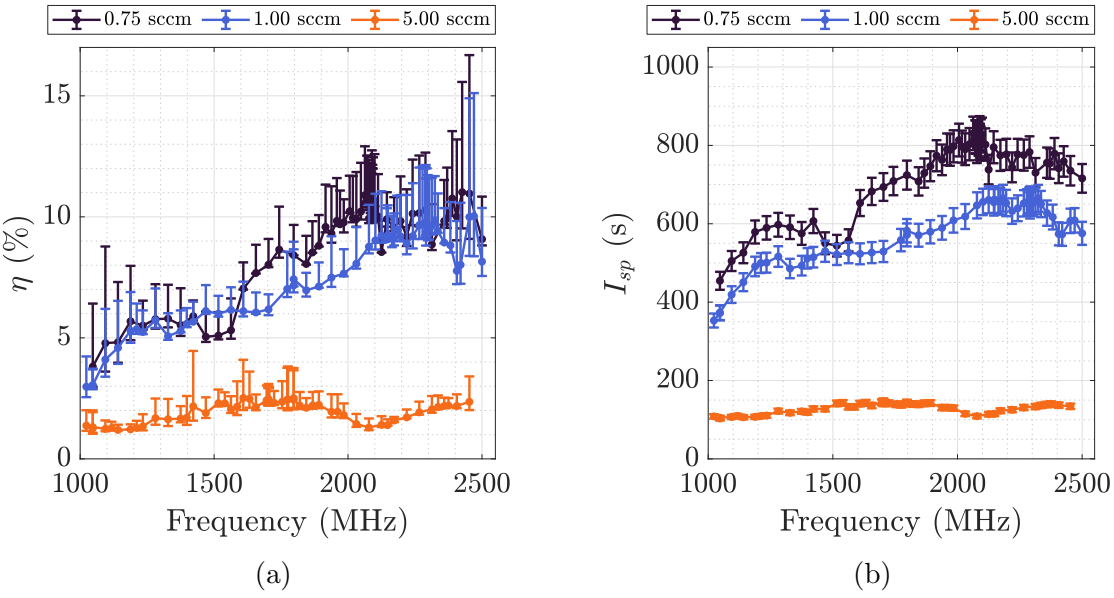

Figure 5.6: Results of the single frequency optimization experiment for 20 W absorbed power. (a) Efficiency vs. frequency (b) specific impulse vs. frequency.

2300 MHz. Lower flow rates and powers tend to correspond to higher optimal efficiencies with the maximum efficiency occurring at 0.75 sccm and 20 W absorbed power. Interestingly, at higher flow rates, the optimal frequency shifts to $f_{optim} \approx 1650$ MHz.

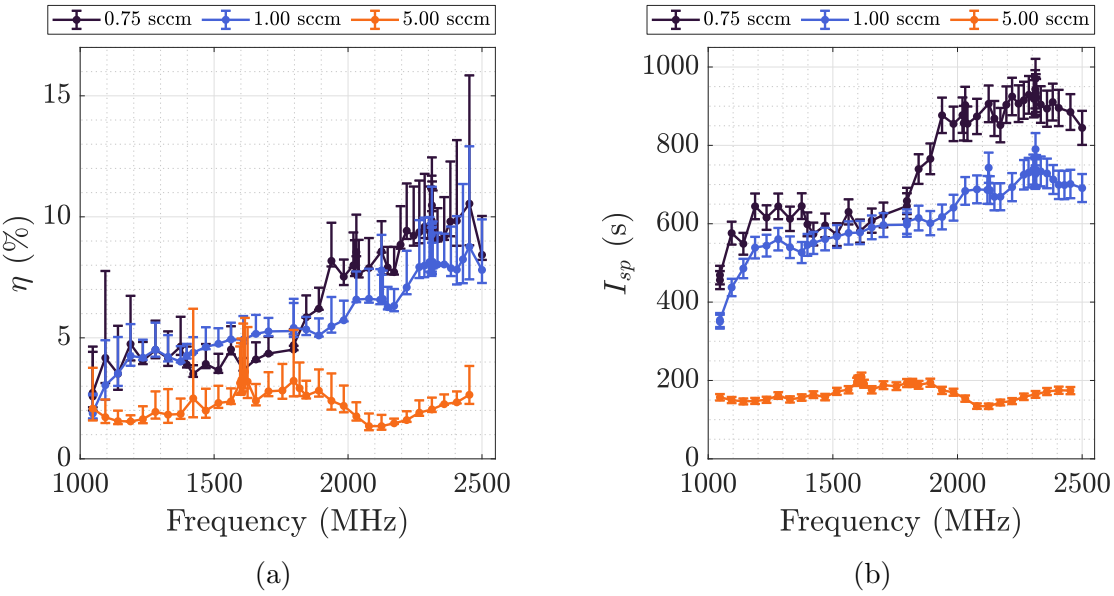

Figure 5.7: Results of the single frequency optimization experiment for 30 W absorbed power. (a) Efficiency vs. frequency (b) specific impulse vs. frequency.

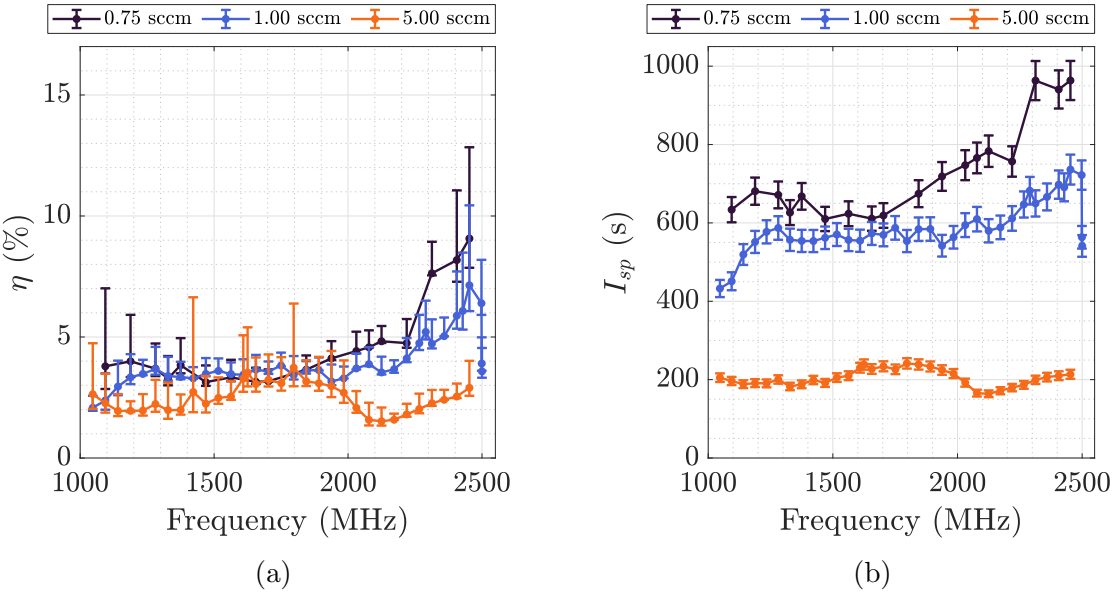

Figure 5.8: Results of the single frequency optimization experiment for 40 W absorbed power. (a) Efficiency vs. frequency (b) specific impulse vs. frequency.

However, higher powers do not appear to affect the overall shape of the thrust versus frequency response at a set flow rate.

5.1.4 Two Frequency Optimization

The two-frequency optimization experiment seeks to find the frequency combination, (f_1, f_2), that maximizes thruster efficiency. For the experiment presented here, we divide the total absorbed power equally between f_1 and f_2. For this experiment, f_1 ranges from 1200 MHz to 2500 Mhz while f_2 ranges from 1000 to 2500 MHz. The minimum frequency gap between f_1 and f_2 is set to 50 MHz to ensure stability.

The two-frequency experiment used the following procedure: We warm up the thruster for approximately one hour until it reaches a thermal quasi-steady state. The thruster is then transitioned to a default low-power set point, typically 7 W and 2400 MHz. While the thruster is in its default state, we run the full thrust stand calibration procedure. We then measure the total thrust at the default low-power set point. After taking this data, we restart the thruster and initiate the two-frequency optimization routine. The optimizer selects a test point consisting of frequencies (f_1, f_2) which is sent to the thruster control LabVIEW program. The program sends a command to the signal generator to switch to the operating frequency to f_1. A special timing mechanism is used to ensure that the plasma does not extinguish. Once at f_1, a software-controlled PID loop is enabled to stabilize the thruster at half of the total absorbed power set point. When the thruster stays within ± 0.5 Watts of the half power for a total of 5 consecutive seconds, the control program adds the second frequency, f_2. The PID loop then controls the power of the second frequency output until the total desired absorbed power is reached. Once the thruster with both frequencies enabled stays within ± 0.5 Watts of the total desired absorbed power for 5 consecutive seconds, the PID loop is turned off. The thruster is then kept at the new set point for 10 seconds to further stabilize. Finally, the thruster is transitioned back to the default set point. Thrust is measured by taking the difference between the test set point and the default set point. The thrust data is then sent back to the optimizer, and the process repeats. To avoid long-term errors caused by thermal drift,

we run a thrust stand calibration procedure every 5 test points. For the experiment presented in this section, the optimizer uses 150 randomized points to initialize the test.

5.1.5 Two-Frequency Results

We show the results of a two-frequency frequency optimization experiment in Fig. 5.9. Here, the first 150 trials are randomly selected. This entire experiment took $\sim$ 24 hours to run. Largely owing to time constraints, we were only able to run a single two-frequency experiment to completion.

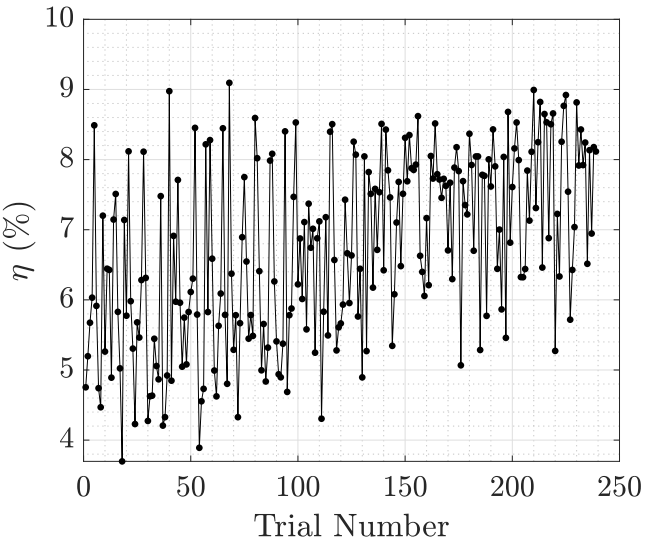

Figure 5.9: Two frequency optimization experiment showing the measured efficiency vs. trial number. The first 150 points are randomly selected while the remaining points are chosen by the the surrogate optimization algorithm.

Figure 5.10 shows the measured efficiency versus f_1 and f_2. We show the upper and lower uncertainty bounds in App. C. While there still remain many unexplored frequency combinations, a clear pattern emerges from the data: set points with frequencies close to the single-frequency optimum tend to perform better.

Overall, however, these two-frequency results do not reach the efficiencies of the single frequency optimal point for the 20 W, 1 sccm operating condition.

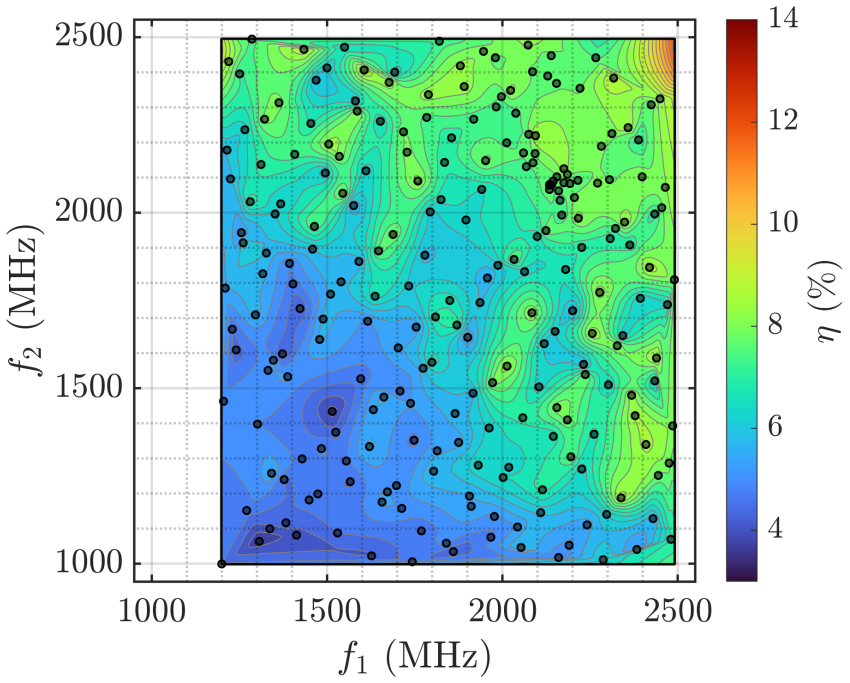

Figure 5.10: Two frequency optimization experiment showing the measured efficiency vs. trial number. The flow rate was set to 1 sccm xenon and the total absorbed power was set to 20 Watts, with each frequency contributing 10 Watts.

5.1.6 Pulsed Optimization

The pulsed optimization experiment used two free parameters: pulse frequency and pulse duty cycle. The total average power is kept constant, and thus the peak power is a function of the set point duty cycle. Here, the pulse frequency was allowed to vary from 10 Hz to 250 KHz while the duty cycle ranged between 40% and 90%. Lower duty cycles were not possible due to the maximum output power of the amplifier. In order to keep the plasma stable, we do not fully turn off the power between pulses. Instead, the minimum power is held at 7 W. This is similar to the simulations presented in Sec. 2.6.2. The testing procedure uses the same steps as the single frequency optimization, with the optimizer and thruster control program commanding a new pulse period and pulse on and off times based on the desired pulse frequency and duty cycle. Using this process, we ran an optimization experiment

with the total average absorbed power set to 20 W and the flow rate set to 1 sccm xenon. The 100 test points took approximately 12 hours to perform largely due to thruster instabilities at certain duty cycles and pulse frequencies.

5.1.6.1 Pulsed Results

Figure 5.11 shows the output efficiency versus pulse frequency and duty cycle. We see from these results that higher duty cycles tend to produce higher efficiencies, regardless of the pulse frequency. This trend can be explained by the low mass utilization efficiencies caused by long off (low-power) periods, as predicted by the simulations in Sec. 2.6.2. We additionally can observe a peak in efficiency for a pulse frequency around 24 KHz. Above these frequencies, the thruster highly unstable, and the plasma would frequently extinguish, forcing a time consuming restart. The cause of this instability is unknown and could be a result of underlying plasma conditions or intermittent loss of power stemming from the signal generator.

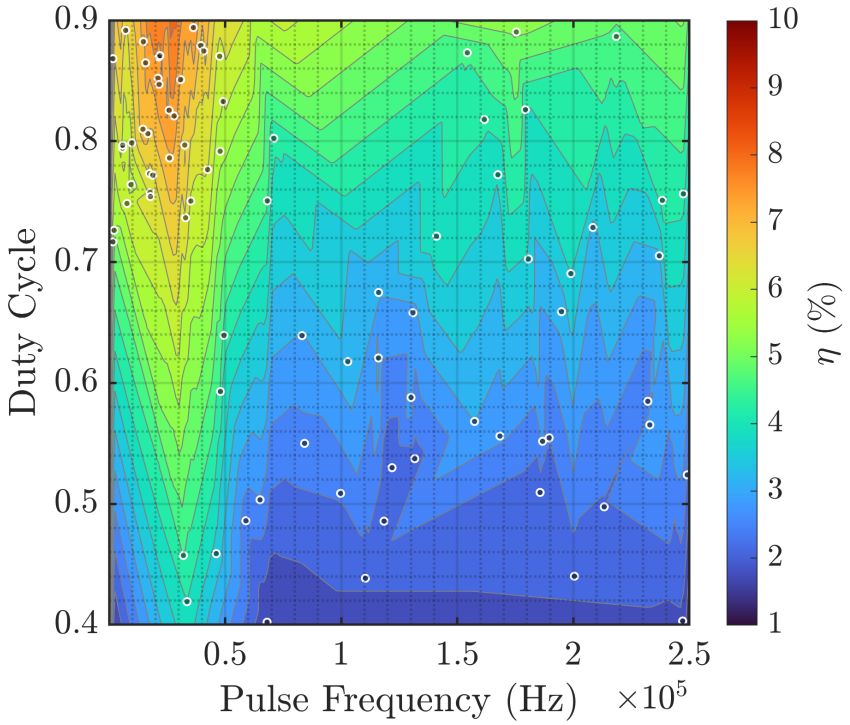

Figure 5.11: Pulsed optimization experiment showing the measured efficiency vs. pulse frequency and duty cycle. The total absorbed power is set to 20 W and the flow rate is 1 sccm xenon.

5.2 Discussion

The results of the single frequency experiments show that thruster performance is strongly linked to input frequency. In the 1 sccm, 20 W operating condition, for example, the maximum measured efficiency was over 3 times the minimum. Similar dependencies were found for higher flow rates despite much lower efficiencies across all frequencies.

Looking at the optimal frequencies, we find that low flow rate conditions have efficiency peaks at higher frequencies, correlating to resonance zones in close proximity to the back wall of the thruster, where the microwave power is injected. These data suggest suggest that the input electromagnetic wave is damped as it travels from the back plane through the plasma. Therefore, having resonance zones closer to the back could utilize the microwave power more efficiently. Classical theory states that

electromagnetic waves will penetrate the plasma over a distance of a few skin depths (δ) given by

$$\delta = \frac{c}{(\omega_{pe}^2 - \omega_{RF}^2)^{\frac{1}{2}}}, \tag{5.1}$$

where c is the speed of light. For the values calculated in Chap. 2, this equation predicts a skin depth on the order of 1 cm. Thus we do expect a substantial change in damping between resonance zones at the back and front of the thruster.

However, the same patterns are not observed in the high flow rate frequency optimization experiments. Here, the optimal frequency tend to concentrate around 1600 MHz. Thus it is possible that a different heating mechanism dominates as collisionality increases, causing the optimal frequency to decrease. Alternatively, the tendency to of the optimal frequency to decrease with higher flow rates could be indicative of an optimal neutral density at the location of ECR resonance and a corresponding optimal reduced electric field strength (E/N).

As shown in the simulations presented in Chap. 2, we suspect that the plasma density within the thruster exceeds the critical density for electromagnetic wave propagation (ω_{pe}). As such, the plasma generated by our experiment exists in a so-called overdense state. The physics behind these overdense plasmas can be quite complex, with several possible plasma waves being excited by the input electromagnetic wave [40]. Thus understanding the underlying cause of the frequency and density response of the thruster may require more in depth simulations.

The two frequency results suggest that it is beneficial, at least in the case of low flow rates, to concentrate the input power within a single frequency. Thus it is possible that performance is maximized by increasing the local resonant electric field intensity at the resonance zone. These results are corroborated by recent ECR thruster experiments using waveguide excitation to power the thruster [94]. In these tests, it was shown that the waveguide thruster performed significantly worse than a thruster with a central conductor. One possible explanation for this behavior is the

weaker local electric field intensity produced within a waveguide when compared to a coaxial design. Thus it is possible that local field strength can play a key role in thruster performance.

Our pulsed modulation experiments demonstrated that, as predicted by our global model simulations, continuous operation leads to higher performance. This effect is likely caused by a higher proportion of input neutrals leaking out of the thruster while it is in a low-power state between high power pulses. While it is theoretically possible to utilize the input propellant more efficiently while pulsing, it is difficult to maintain a stable plasma between pulses. If this technical challenge is overcome, it may be possible to achieve higher efficiencies while pulsing at very low flow rates.

5.3 Summary

In this section we have presented the setup and results of a series of optimization experiments testing whether the thruster's efficiency can be increased using single frequency tuning, two-frequency mixing, and pulsed modulation. We detailed the test procedures, including the optimization algorithm used during testing. The results show that significant gains can be made using single frequency tuning with the efficiencies at the optimal frequencies typically ~ 3 times higher than those at the least optimal frequencies. However, the optimal frequency was found to depend on the input flow rate. The underlying cause of this efficiency gain remains a topic for future research.

The results of the two-frequency experiment suggest that adding a second resonance zone does not improve efficiency when compared to the single frequency optimum. While certain frequency combinations were not explored, such as two very close frequencies (< 50 MHz separation), the initial data suggest that this approach may not lead to efficiency gains. Finally, our test using pulsed modulation demonstrated that, over the duty cycles and frequencies tested, the thruster performed best

with continuously applied power, suggesting that input propellant was being wasted between pulses.

CHAPTER VI

Conclusions and Future Work

6.1 Summary

ECR magnetic nozzle technology shows great promise for small satellite missions. The efficiencies measured as part of this dissertation and at other laboratories put ECR thrusters well in line with competing low-power EP thruster technologies. Their simple architecture and resilient operation, including the potential to use alternative propellants, may someday make them a ubiquitous on-orbit technology. In this dissertation, we have covered three facets of ECR magnetic nozzle thruster development: modelling thruster performance using relatively simple global plasma models, practical testing procedures for accurate on-ground performance measurements, and closed-loop efficiency optimization using custom microwave waveforms.

The global plasma models presented in Chapter 2 provide a framework for understanding the energy loss mechanisms and avenues for improvement in designing these thrusters. These models assume a uniform plasma and neutral density and do not consider the electron heating mechanism. Thus they cannot capture the subtleties involved in thruster operation including wave-coupling, plasma confinement, magnetic nozzle plasma expansion, and electron heat transfer. However, using free parameters, we can utilize these models to predict the effects of better confining plasma and more efficient nozzle expansion. Using time-dependent solvers, we can further predict the

impact of pulsing the power absorbed by the thruster. Our findings suggest that a large portion of the input power is lost to collisions with the radial and back walls when increased plasma confinement from magnetic field effects is not included. These simulations further showed that at low powers, there are substantial losses associated with low mass utilization efficiency. Finally, these simulations suggested that pulsing the power would likely decrease performance by further lowering the mass utilization efficiency as neutrals escape the thruster during power-off times.

The ladder part of this dissertation concerned experimental techniques and campaigns using ECR thrusters. To this end, we have provided an architecture for generating and measuring microwave power, measuring thrust forces, and finally, understanding facility effects inherent to ECR thruster operation. We described in Chapter 3 a methodology for generating broadband microwave power and accurately assessing the power deposited to the thruster. This included an in-depth error analysis for determining the range of delivered powers absorbed by a microwave thruster, with the bulk of the uncertainty arising from directivity errors associated with microwave directional couplers. In the second half of Chapter 3, we presented the design and operation of a thrust stand for measuring these low thrust-to-power devices. This included a novel wireless power coupler that eliminated the stiffness and thermal deformation typically caused by high-power coaxial cables while maintaining a large operational bandwidth.

Chapter 4 provided an experimental and theoretical framework for understanding the role of facility effects in testing ECR thrusters. Our work confirmed previous findings that high background pressures can adversely affect ECR thruster performance. By measuring ion velocities using laser induced fluorescence, we showed that the ion VDFs were broadened to lower velocities, thus explaining the lower thrust. Using global models, we showed that these effects were a consequence of electron-neutral collisions within the plume of the thruster. This tool allowed for extrapolation of

on-ground performance with finite background pressures to space-like environments. In this chapter, we additionally provided a preliminary investigation of the effects of conducting facility walls in the near vicinity of the thruster. Our experiments in the Large Vacuum Test Facility showed that, while it was possible that nearby walls could adversely affect thruster performance, it was likely that lower background pressures accounted for much of the observed changes in thrust.

The final Chapter of this thesis explores the optimization of the ECR thruster using changes in input microwave frequency and waveform. Using an automated optimization program, we tested single frequency, two-frequency, and pulsed waveforms. The single frequency results showed that by shifting the frequency over a span of a few tens of MHz, we could significantly improve performance of the thruster. Interestingly, this optimal frequency changed as flow rate increased. Adding a second frequency was not found to improve performance versus the single frequency optimal. Finally, we showed that pulsing the power to the thruster did not improve performance. This was likely caused by increased neutral losses, as predicted in our global models.

6.2 Major Contributions

The major contributions stemming from this dissertation can be summarized as follows:

1. Zero-dimensional global models for investigating trends in magnetic nozzle thruster performance.

2. Framework for testing ECR thrusters and characterizing uncertainty in performance measurements.

3. Explanation for magnetic nozzle efficiency decreases when operating in high background pressures.

4. Experimental evidence demonstrating the utility of frequency tuning for ECR thrusters.

6.3 Future Work

While ECR thrusters may have reached efficiency levels competitive with other low-power EP thruster technologies, many avenues for future exploration and optimization remain.

The experiments presented in this dissertation suggest that two frequency and pulsed waveforms likely do not improve thruster efficiency beyond what is obtainable through single frequency tuning. However, other waveforms may prove to be more beneficial. These include chirped waveforms and frequency modulation, which would move the resonance zone back and forth within the thruster. Additionally, the optimization experiments could be expanded to include the input power and mass flow rate as free parameters, thus allowing us to find a global optimally efficient operating condition.

Beyond waveform optimization, there is still potential to improve thruster performance by changing the thruster geometry and materials, magnetic field topology, and gas injection mechanisms. Our research suggests that radial wall losses are largely mitigated by the magnetic field, however moving to higher magnetic field strength, and thus higher resonance frequencies, may prove to reduce wall losses to a greater extent. The increase in frequency will inevitably lead to more skin-effect losses, and thus there may exist an optimal field strength. Given the low mass utilization efficiency predicted and measured at low powers, there are likely ways to combat these losses. Alternative neutral injection schemes are already a topic of research [112].

Each of these optimization schemes will benefit from more advanced simulation and modelling techniques that can capture wave coupling, magnetic nozzle effects, and downstream boundary conditions. For instance, capturing the ECR power absorption

will enable us to understand the effects of shifting the location of the resonance zone within the discharge. Some of these models are under currently under development. Given the decades long efforts to model Hall thrusters that have not yet yielded fully predictive models, it will be beneficial to run these efforts in parallel.

From an engineering perspective, it will be critical to develop high efficiency microwave power processing units, both to ensure high system efficiency and prevent excessive on-orbit thermal loads.

Finally, work should continue on developing these thrusters with alternative propellants—especially given the recent price of xenon. This includes other rare gasses such as krypton and argon, and, ideally, condensable propellants such as metals and water. While iodine has been proven as a viable propellant for small satellite propulsion [100; 14], future research could include other condensables such as water or bismuth [104; 78].

APPENDICES

APPENDIX A

Thrust Stand Appendix

A.1 Thrust Stand Static Model

Using Fig. 3.15 as a reference, we derive a static sum of moments as follows:

$$0 = -F_T l_T - m_{CW} g \left(l_{CW} \sin(\theta) + d_{CW} \cos(\theta)\right) - m_{cal} g l_{cal} \cos(\theta) \\ - m_{arm} g l_{arm} \cos(\theta) + m_T g \left(l_{COM} \sin(\theta) + d_{COM} \cos(\theta)\right) + k\theta, \quad \text{(A.1)}$$

where F_T is the thrust force, l_T is the length from the pivot to the center of thrust, m_{cal} is the added calibration mass, and l_{cal} is the length from the pivot to the location where the calibration masses are applied. The lengths d_{CW}, l_{CW}, d_{COM}, and l_{COM}, are the horizontal and vertical coordinates of the center of masses of the counterweight (CW) and thruster (COM) with respect to the pivot point. The length l_{arm} is the horizontal length of the center of mass of the calibration arm. These dimensions and the masses, m_{CW}, m_T, and m_{arm} include support structure masses.

Employing the small angle approximation simplifies Eq. A.1 to

$$0 = -F_T l_T - m_{CW} g \left(l_{CW}\theta + d_{CW}\right) - m_{cal} g l_{cal} - m_{arm} g l_{arm} + m_T g \left(l_{COM}\theta + d_{COM}\right) + k\theta. \tag{A.2}$$

Solving for θ gives:

$$\theta = \frac{-F_T l_T - m_{CW} g d_{CW} - m_{cal} g l_{cal} - m_{arm} g l_{arm} + m_T g d_T}{m_{CW} g l_{CW} - m_T g l_{COM} - k}. \tag{A.3}$$

We can now solve for the measurable quantity, δ_{disp}, by making the substitution $\delta_{disp} = \delta_0 - l_{sens}\sin(\theta)$, where δ_0 is the distance to the sensor when $\theta = 0$. Again employing the small angle approximation, we find

$$\theta = \frac{\delta_0 - \delta_{disp}}{l_{sens}}. \tag{A.4}$$

Substituting this expression into Eq. A.3 and solving for δ_{disp} gives:

$$\delta_{disp} = -l_{sens}\left[\frac{-F_T l_T - m_{CW} g d_{CW} - m_{cal} g l_{cal} - m_{arm} g l_{arm} + m_T g d_T}{m_{CW} g l_{CW} - m_T g l_{COM} - k} + \delta_0\right]. \tag{A.5}$$

From Eq. A.5, we can derive the change in displacement, $\Delta\delta_{disp}$, caused by changes in thrust (F_T) and changes in calibration mass (m_{cal}):

$$\Delta\delta_{disp} = l_{sens}\left[\frac{(F_T - F_{T,0})l_T + (m_{cal} - m_{cal,0})g l_{cal}}{m_{CW} g l_{CW} - m_T g l_{COM} - k}\right], \tag{A.6}$$

where $F_{T,0}$ and $m_{cal,0}$ are initial thrust and calibration forces, typically 0 for our purposes. We can thus relate the displacement to changes in thrust by setting $m_{cal} = m_{cal,0} = 0$. Simplifying the resulting expression yields

$$\Delta\delta_{disp} = A_T F_T + b_{T,0}, \tag{A.7}$$

where the slope of the line, A_T, is given by

$$A_T = l_{sens} \frac{l_T}{m_{CW} g l_{CW} - m_{COM} g l_{COM} - k}. \tag{A.8}$$

A.2 Relation Between Calibration and Thrust Forces

Using Eq. A.6 we solve for the displacement caused by changes in calibration mass by setting $F_T = T_{T,0} = 0$. Simplifying the resulting expression yields

$$\Delta\delta_{cal} = A_{cal} F_{cal} + b_{cal,0}, \tag{A.9}$$

where the calibration force $F_{cal} = g m_{cal}$. The slope of the calibration line, A_{cal}, is given by

$$A_{cal} = l_{sens} \frac{l_{cal}}{m_{CW} g l_{CW} - m_{COM} g l_{COM} - k}. \tag{A.10}$$

Using Eqs. A.10 and A.8 we can relate the displacement caused by thrust force to that from calibration force as

$$\frac{A_T}{A_{cal}} = \frac{l_T}{l_{cal}}. \tag{A.11}$$

Thus applying a force F at the calibration arm is equivalent to applying a for $F\frac{l_{cal}}{l_T}$ at the thruster.

APPENDIX B

Ion Energy Formulation

The total energy flux term is given by:

$$\mathbf{Q}_i = \mathbf{q}_i + p_i \mathbf{u}_i + \frac{3}{2} p_i \mathbf{u}_i + \frac{1}{2} m_i n_i u_i^2 \mathbf{u}_i, \tag{B.1}$$

where q_i is the heat conductivity,p_i is ion pressure, $\mathbf{u}_i$ is drift velocity and m_i is ion mass. For electrons, we have

$$\mathbf{Q}_e = \mathbf{q}_e + p_e \mathbf{u}_e + \frac{3}{2} p_e \mathbf{u}_e + \frac{1}{2} m_e n_e u_e^2 \mathbf{u}_e, \tag{B.2}$$

where q_e is the heat conductivity,p_e is electron pressure, $\mathbf{u}_e$ is drift velocity and m_e is electron mass.

The ion and electron energy equations can be expressed as

$$\nabla \cdot \mathbf{Q}_i - q n_i \mathbf{E} \cdot \mathbf{u}_i = W_i + \mathbf{u}_i \cdot \mathbf{F}_i, \tag{B.3}$$

$$\nabla \cdot \mathbf{Q}_e + q n_e \mathbf{E} \cdot \mathbf{u}_e = W_e + \mathbf{u}_e \cdot \mathbf{F}_e. \tag{B.4}$$

Adding these expressions together yields

$$\nabla \cdot (\mathbf{Q}_i + \mathbf{Q}_e) + qn_i\mathbf{E} \cdot (\mathbf{u}_e - \mathbf{u}_i) = W_i + W_e + \mathbf{u}_i \cdot \mathbf{F}_i + \mathbf{u}_e \cdot \mathbf{F}_e. \tag{B.5}$$

Focusing on the second term of the LHS, we assume the fields are electrostatic such that $\nabla\phi = -\mathbf{E}$. This allows us to write

$$qn_i\mathbf{E} \cdot (\mathbf{u}_e - \mathbf{u}_i) = -qn_i\nabla\phi \cdot (\mathbf{u}_e - \mathbf{u}_i) \tag{B.6}$$

$$= -q\nabla \cdot (\phi n_e (\mathbf{u}_e - \mathbf{u}_i)) + q\phi\nabla \cdot [n_e (\mathbf{u}_e - \mathbf{u}_i)] \tag{B.7}$$

From the ion and electron continuity equations we have

$$\nabla \cdot (n_e\mathbf{u}_e) = n_e\nu_{ion} \tag{B.8}$$

$$\nabla \cdot (n_u\mathbf{u}_i) = n_i\nu_{ion}, \tag{B.9}$$

where ν_{ion} denotes the ionization frequency. Subtracting the top from the bottom and assuming quasi-neutrality yields

$$\nabla \cdot [n_e (\mathbf{u}_e - \mathbf{u}_i)] = 0. \tag{B.10}$$

Substituting this into Eq. B.7, we find

$$qn_i\mathbf{E} \cdot (\mathbf{u}_e - \mathbf{u}_i) = -q\nabla \cdot (\phi n_e (\mathbf{u}_e - \mathbf{u}_i)). \tag{B.11}$$

Finally, we substitute into Eq. B.5 to find

$$\nabla \cdot (\mathbf{Q}_i + \mathbf{Q}_e - q\phi n_e (\mathbf{u}_e - \mathbf{u}_i)) = W_i + W_e + \mathbf{u}_i \cdot \mathbf{F}_i + \mathbf{u}_e \cdot \mathbf{F}_e. \tag{B.12}$$

We can simplify further by recognizing that electron inertia is negligible, ions are

cold, and the inelastic energy lost from ions from collisions is negligible

$$\nabla \cdot \left(\frac{1}{2} m_i n_i u_i^2 + \mathbf{q}_e + \frac{5}{2} n_e T_e \mathbf{u}_e - q\phi n_e \left(\mathbf{u}_e - \mathbf{u}_i \right) \right) = W_e + \mathbf{u}_i \cdot \mathbf{F}_i + \mathbf{u}_e \cdot \mathbf{F}_e. \quad \text{(B.13)}$$

Performing a quasi-1D control volume analysis for the nozzle we find

$$\begin{aligned} \frac{1}{2} \left[\dot{m}_{i(e)} u_{i(e)}^2 - \dot{m}_{i(t)} u_{i(t)}^2 \right] =& q\phi_e \left(I_{e(e)} - I_{i(e)} \right) - \phi_t \left(I_{e(t)} - I_{i(t)} \right) \\ &+ Q_{t(e)} - Q_{e(e)} \\ &+ \frac{1}{m_e} \frac{5}{2} \left(\dot{m}_{e(t)} T_{e(t)} - \dot{m}_{e(e)} T_{e(e)} \right) \\ &+ \int_V \left[W_e + \mathbf{u}_i \cdot \mathbf{F}_i + \mathbf{u}_e \cdot \mathbf{F}_e \right] dV, \end{aligned} \quad \text{(B.14)}$$

where Q denotes total heat flux out of each surface, I is the current from each species flowing through each surface, $\dot{m}$ denotes mass flux, V denotes the control volume, and subscripts t and$e$ refer to throat and exit respectively.

Now, let us assume ambipolarity *at the exit and nozzle* such that the currents cancel. This allows us to write

$$\begin{aligned} \frac{1}{2} \left[\dot{m}_{i(e)} u_{i(e)}^2 - \dot{m}_{i(t)} u_{i(t)}^2 \right] =& Q_{t(e)} - Q_{e(e)} \\ &+ \frac{1}{m_i} \frac{5}{2} \left(\dot{m}_{i(t)} T_{e(t)} - \dot{m}_{i(e)} T_{e(e)} \right) \\ &+ \int_V \left[W_e + \mathbf{u}_i \cdot \mathbf{F}_i + \mathbf{u}_e \cdot \mathbf{F}_e \right] dV. \end{aligned} \quad \text{(B.15)}$$

Dividing through by $\dot{m}_{i(e)}$ we find

$$\begin{aligned} \frac{1}{2} u_{i(e)}^2 = & \frac{\dot{m}_{i(t)}}{\dot{m}_{i(e)}} u_{i(t)}^2 + \frac{1}{\dot{m}_{i(e)}} \left[Q_{t(e)} - Q_{e(e)} \right] + \frac{1}{m_i} \frac{5}{2} \left(\frac{\dot{m}_{i(t)}}{\dot{m}_{i(e)}} T_{e(t)} - T_{e(e)} \right) \\ &+ \frac{1}{\dot{m}_{i(e)}} \int_V \left[W_e + \mathbf{u}_i \cdot \mathbf{F}_i + \mathbf{u}_e \cdot \mathbf{F}_e \right] dV. \end{aligned} \quad \text{(B.16)}$$

We next recognize that assuming Bohm speed for the ions at the throat we can write

this as

$$\begin{aligned}\frac{1}{2}u_{i(e)}^2 = &\frac{1}{\dot{m}_{i(e)}}\left[Q_{t(e)} - Q_{e(e)}\right] + \frac{1}{m_i}\left(\frac{\dot{m}_{i(t)}}{\dot{m}_{i(e)}}\frac{7}{2}T_{e(t)} - \frac{5}{2}T_{e(e)}\right) \\ &+ \frac{1}{\dot{m}_{i(e)}}\int_V \left[W_e + \mathbf{u}_i \cdot \mathbf{F}_i + \mathbf{u}_e \cdot \mathbf{F}_e\right] dV.\end{aligned} \tag{B.17}$$

As an intermediate step, we can introduce the following relationships

$$\int_V \left[W_e + \mathbf{u}_e \cdot \mathbf{F}_e\right] dV = -\int_V n_i \nu_{ion}\left(\epsilon_{ion} + m_e u_e^2\right) dV = -P_{ion} \tag{B.18}$$

$$\int_V \mathbf{u}_i \cdot \mathbf{F}_i dV = -\int_V n_i \nu_{cex} u_i^2 dV = -P_{cex} \tag{B.19}$$

For the first term though, we can make the approximation that $m_e u_e^2 \approx T_e$. With these definitions we can write the following expression for the ion energy

$$\frac{1}{2}u_{i(e)}^2 = \frac{1}{\dot{m}_{i(e)}}\left[Q_{t(e)} - Q_{e(e)}\right] + \frac{1}{m_i}\left(\frac{\dot{m}_{i(t)}}{\dot{m}_{i(e)}}\frac{7}{2}T_{e(t)} - \frac{5}{2}T_{e(e)}\right) - \frac{1}{\dot{m}_{i(e)}}\left[P_{ion} + P_{cex}\right]. \tag{B.20}$$

With this result, we can write down the circumstances in which there are no neutrals and the chamber dynamics remain unchanged.

$$\frac{1}{2}u_{i(e)}^2|_{ideal} = \frac{1}{\dot{m}_{i(t)}}\left[Q_{t(e)} - Q_{e(e)}|_{ideal}\right] + \frac{1}{m_i}\left(\frac{7}{2}T_{e(t)} - \frac{5}{2}T_{e(e)}|_{ideal}\right). \tag{B.21}$$

$$= \frac{1}{\dot{m}_{i(t)}}\left[Q_{t(e)} + \frac{\dot{m}_{i(t)}}{m_i}\frac{7}{2}T_{e(t)}\right] - \frac{1}{\dot{m}_{i(t)}}\left[Q_{e(e)}|_{ideal} + \frac{\dot{m}_{i(t)}}{m_i}\frac{5}{2}T_{e(e)}|_{ideal}\right] \tag{B.22}$$

We thus can write in Eq. B.20 that

$$\begin{aligned}\frac{1}{2}u_{i(e)}^2 = &\frac{1}{2}\left(\frac{\dot{m}_{i(t)}}{\dot{m}_{i(e)}}\right)u_{i(e)}^2|_{ideal} + \frac{1}{\dot{m}_{i(e)}}\left(Q_{e(e)}|_{ideal} - Q_{e(e)}\right) \\ &+ \frac{1}{m_i}\left(\frac{5}{2}\right)\left(T_{e(e)}|_{ideal} - T_{e(e)}\right) - \frac{1}{\dot{m}_{i(e)}}\left[P_{ion} + P_{cex}\right]\end{aligned} \tag{B.23}$$

Returning to Eq. B.20, we can also recognize that the power fluxing through the throat can be written as

$$P_t = Q_{e(t)} + \frac{\dot{m}_{i(t)}}{m_i}\frac{7}{2}T_{e(t)} \tag{B.24}$$

Thus, we can re-write the expression as

$$\frac{1}{2}u_{i(e)}^2 = -\frac{1}{\dot{m}_{i(e)}}Q_{e(e)} - \frac{1}{m_i}\frac{5}{2}T_{e(e)} + \frac{1}{\dot{m}_{i(e)}}\left[P_t - P_{ion} - P_{cex}\right], \tag{B.25}$$

which simplifies to

$$\frac{1}{2}u_{i(e)}^2 = \frac{P_t}{\dot{m}_i}\left[-\frac{\dot{m}_i}{\dot{m}_{i(e)}}\frac{Q_{e(e)}}{P_t} - \frac{\dot{m}_i}{m_i}\frac{5}{2}\frac{T_{e(e)}}{P_t} + \frac{\dot{m}_i}{\dot{m}_{i(e)}}\left[1 - \frac{P_{ion}}{P_t} - \frac{P_{cex}}{P_t}\right]\right]. \tag{B.26}$$

APPENDIX C

Optimization Experiment Data

C.1 One-Frequency Full Data Set

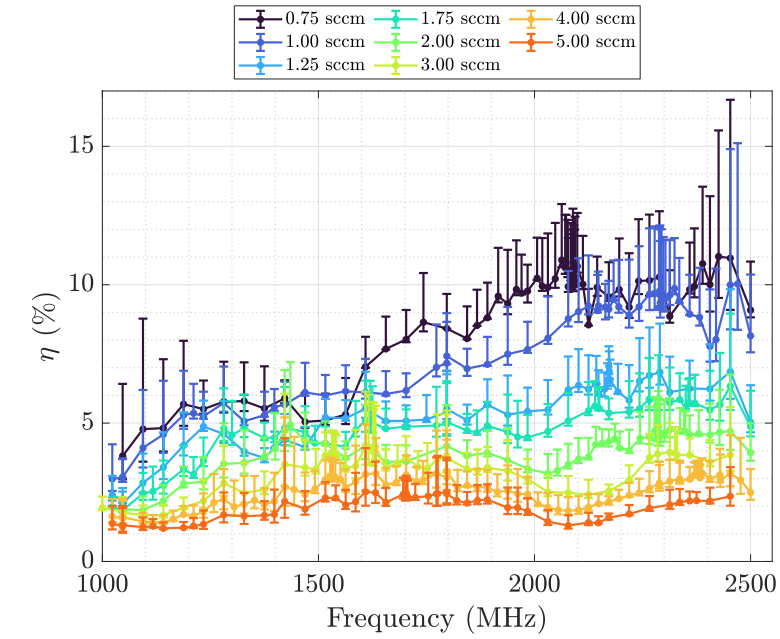

(a)

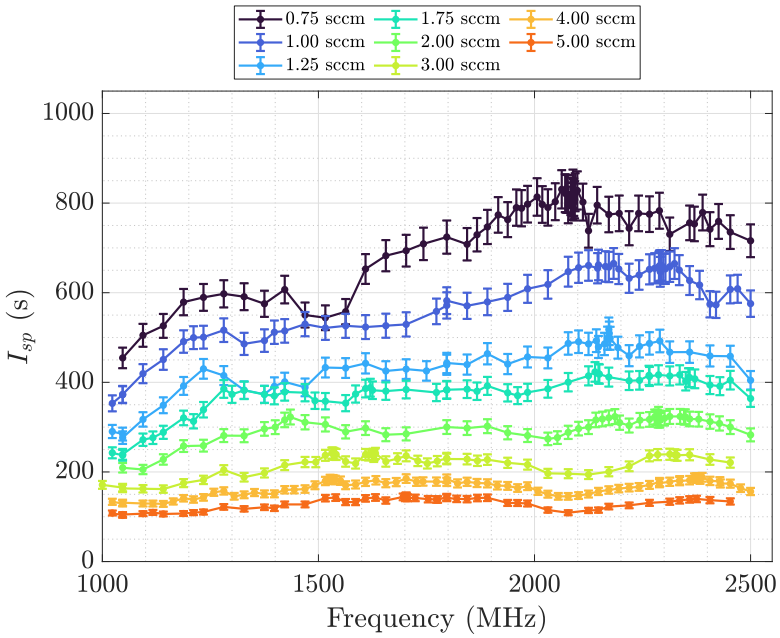

(b)

Figure C.1: (a) Efficiency vs. frequency and (b) I_{sp} vs. frequency for 20 W operating condition.

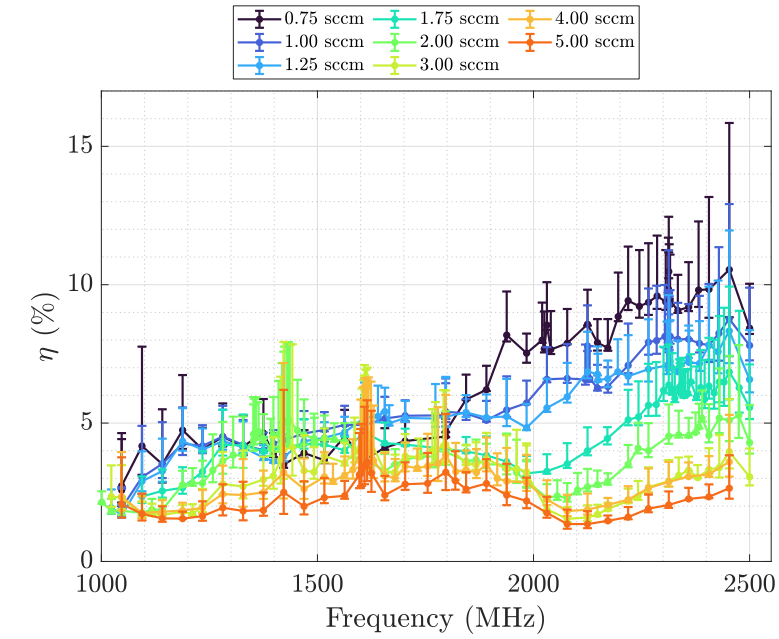

(a)

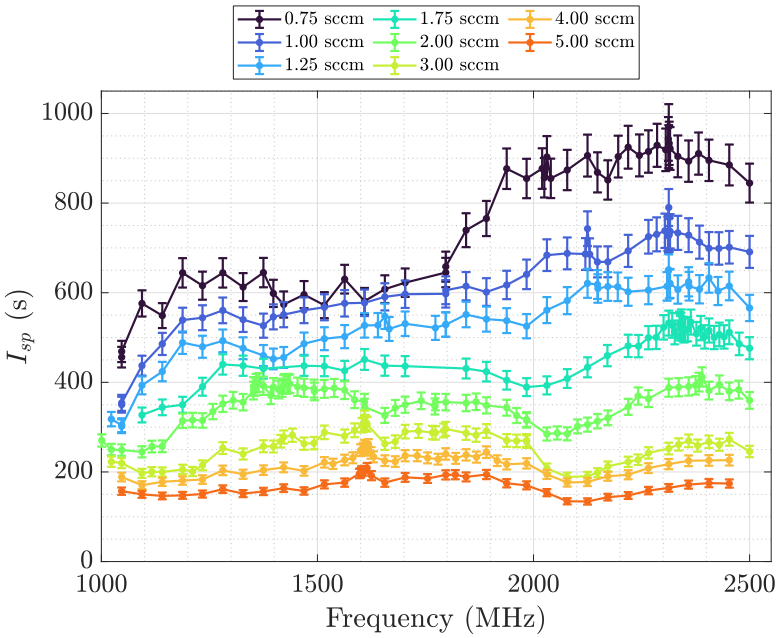

(b)

Figure C.2: (a) Efficiency vs. frequency and (b) I_{sp} vs. frequency for 30 W operating condition.

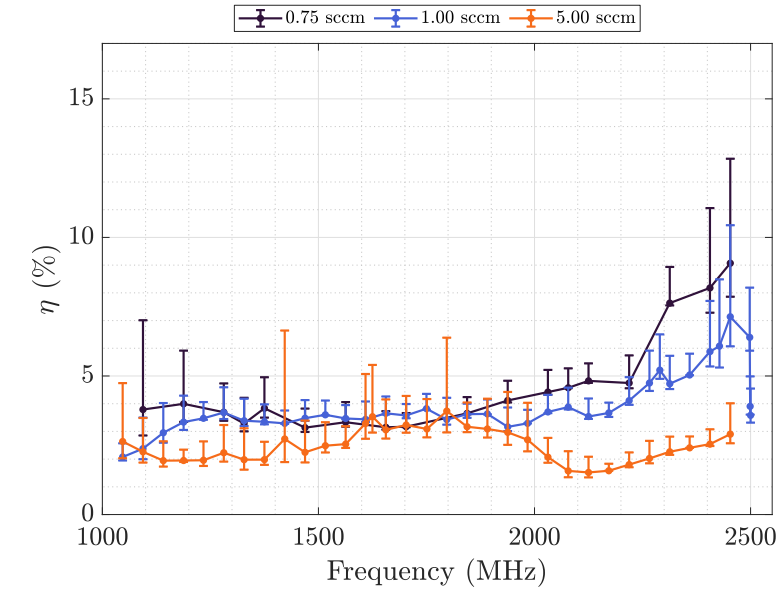

(a)

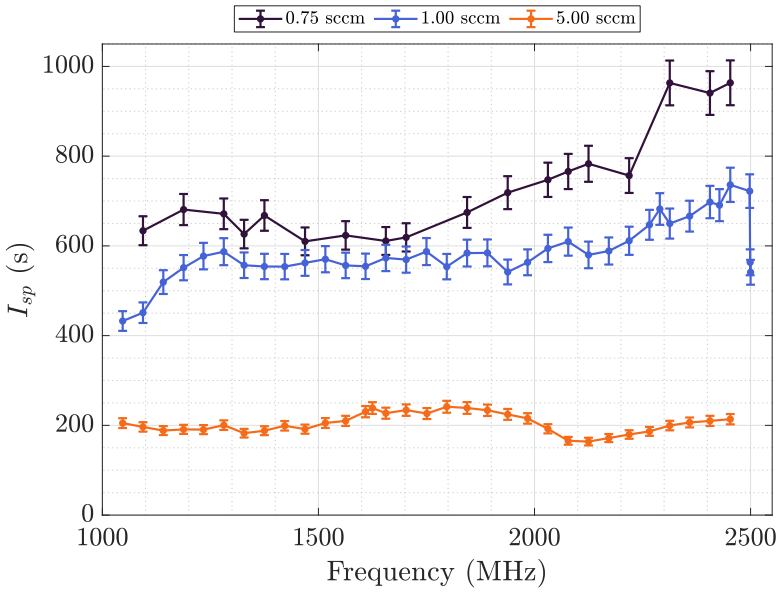

(b)

Figure C.3: (a) Efficiency vs. frequency and (b) I_{sp} vs. frequency for 40 W operating condition.

C.2 Two-Frequency Uncertainty

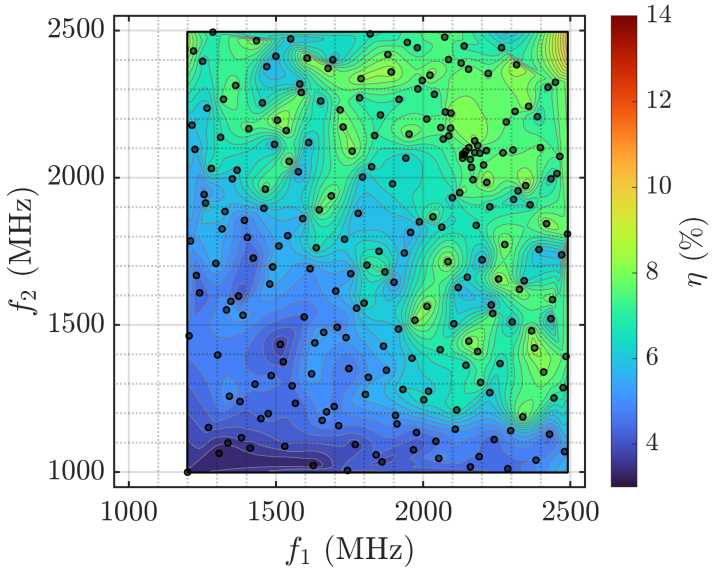

(a)

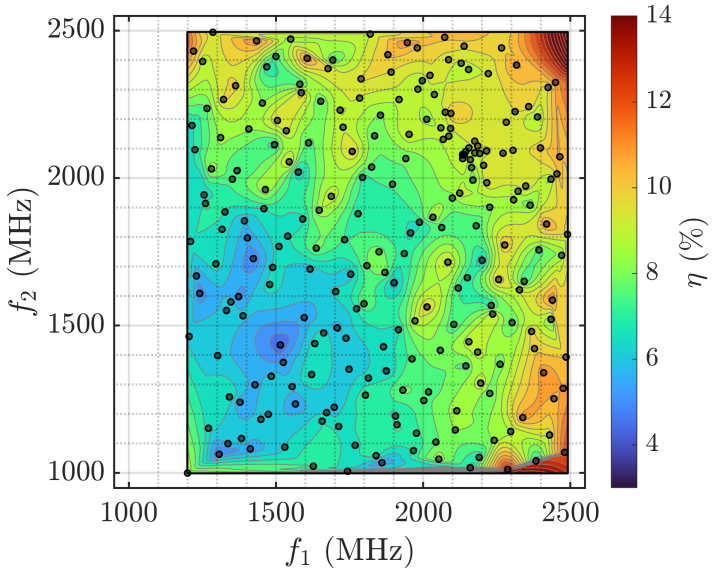

(b)

Figure C.4: (a) Minimum efficiency vs. f_1 and f_2 and (b) minimum efficiency vs. f_1 and f_2 based on the uncertainty analysis presented in Chap. 3. The total absorbed power is 20 W and flow rate is 1 sccm xenon.

BIBLIOGRAPHY

BIBLIOGRAPHY

[1] (), Surrogate Optimization Algorithm - MATLAB & Simulink.

[2] (2019), Solutions for Measurment Uncertainty Minimize Measurement Uncertainty and Estimate Uncertainty Due to Mismatch, *Application Note 5991-0673EN*, Keysight Technologies.

[3] (2021), State-of-the-Art Small Spacecraft Technology, *Tech. Rep. TP—20210021263*, NASA, Ames Research Center, Moffett Field, California.

[4] (2022), Smallsats by the Numbers, *Tech. rep.*, Bryce Tech.

[5] Ahedo, E., and M. Merino (2010), Two-dimensional supersonic plasma acceleration in a magnetic nozzle, *Physics of Plasmas*, *17*(7), 073,501, doi: 10.1063/1.3442736.

[6] Ahedo, E., and M. Merino (2011), On plasma detachment in propulsive magnetic nozzles, *Physics of Plasmas*, *18*(5), 053,504, doi:10.1063/1.3589268.

[7] Ahedo, E., and J. Navarro-Cavallé (2013), Helicon thruster plasma modeling: Two-dimensional fluid-dynamics and propulsive performances, *Physics of Plasmas*, *20*(4), 043,512, doi:10.1063/1.4798409.

[8] Ahedo, E., S. Correyero, J. Navarro-Cavallé, and M. Merino (2020), Macroscopic and parametric study of a kinetic plasma expansion in a paraxial magnetic nozzle, *Plasma Sources Science and Technology*, *29*(4), 045,017, doi: 10.1088/1361-6595/ab7855.

[9] Araki, S. J., and R. E. Wirz (2013), Ion–Neutral Collision Modeling Using Classical Scattering With Spin-Orbit Free Interaction Potential, *IEEE Transactions on Plasma Science*, *41*(3), 470–480, doi:10.1109/TPS.2013.2241457.

[10] Arefiev, A. V., and B. N. Breizman (2004), Theoretical components of the VASIMR plasma propulsion concept, *Physics of Plasmas*, *11*(5), 2942–2949, doi:10.1063/1.1666328.

[11] Atmosphere, U. S. (1976), *US standard atmosphere*, National Oceanic and Atmospheric Administration.

[12] Baird, D. C. (1962), *Experimentation: an introduction to measurement theory and experiment design.*, Prentice-Hall, Englewood Cliffs, N.J.

[13] Bathgate, S. N., M. M. M. Bilek, and D. R. Mckenzie (2017), Electrodeless plasma thrusters for spacecraft: a review, *Plasma Science and Technology*, *19*(8), 083,001, doi:10.1088/2058-6272/aa71fe.

[14] Bellomo, N., et al. (2022), Design and In-orbit Demonstration of REGULUS, an Iodine electric propulsion system, *CEAS Space Journal*, *14*(1), 79–90, doi:10.1007/s12567-021-00374-4.

[15] Cannat, F., J. Jarrige, P.-Q. Elias, and D. Packan (2014), Experimental investigation of magnetic gradient influence in a coaxial ECR plasma thruster, in *Space Propulsion 2014*.

[16] Cannat, F., T. Lafleur, J. Jarrige, P. Chabert, P.-Q. Elias, and D. Packan (2015), Optimization of a coaxial electron cyclotron resonance plasma thruster with an analytical model, *Physics of Plasmas*, *22*(5), 053,503, doi:10.1063/1.4920966.

[17] Caruso, N. R. S., and M. L. R. Walker (2018), Neutral Ingestion Effects on Plume Properties of a Radio-Frequency Plasma Discharge, *Journal of Propulsion and Power*, *34*(1), 58–65, doi:10.2514/1.B36404.

[18] Celona, L., et al. (2008), Observations of the frequency tuning effect in the 14 GHz CAPRICE ion source, *Review of Scientific Instruments*, *79*(2), 023,305, doi:10.1063/1.2841694.

[19] Chaplin, V. H., B. A. Jorns, A. Lopez Ortega, I. G. Mikellides, R. W. Conversano, R. B. Lobbia, and R. R. Hofer (2018), Laser-induced fluorescence measurements of acceleration zone scaling in the 12.5 kW HERMeS Hall thruster, *Journal of Applied Physics*, *124*(18), 183,302, doi:10.1063/1.5040388.

[20] Chaplin, V. H., R. W. Conversano, A. Lopez Ortega, I. G. Mikellides, R. B. Lobbia, and R. R. Hofer (2019), Ion Velocity Measurements in the Magnetically Shielded Miniature (MaSMi) Hall Thruster Using Laser-Induced Fluorescence, Vienna, Austria.

[21] Charles, C., R. W. Boswell, and M. A. Lieberman (2006), Xenon ion beam characterization in a helicon double layer thruster, *Applied Physics Letters*, *89*(26), 261,503, doi:10.1063/1.2426881.

[22] Chen, F. F. (2008), Permanent Magnet Helicon Source for Ion Propulsion, *IEEE Transactions on Plasma Science*, *36*(5), 2095–2110, doi:10.1109/TPS.2008.2004039, conference Name: IEEE Transactions on Plasma Science.

[23] Chen, F. F. (2015), Helicon discharges and sources: a review, *Plasma Sources Science and Technology*, *24*(1), 014,001, doi:10.1088/0963-0252/24/1/014001.

[24] Choueiri, E. Y. (2004), A Critical History of Electric Propulsion: The First 50 Years (1906-1956), *Journal of Propulsion and Power*, *20*(2), 193–203, doi:10.2514/1.9245.

[25] Collard, T., and J. Sheehan (2016), Preliminary Measurements of an Integrated Prototype of the CubeSat Ambipolar Thruster, in *52nd AIAA/SAE/ASEE Joint Propulsion Conference*, American Institute of Aeronautics and Astronautics, Salt Lake City, UT, doi:10.2514/6.2016-5042.

[26] Collard, T., M. Byrne, S. Hepner, C. J. Durot, and B. Jorns (2017), Investigation of Detachment in a Miniature Magnetic Nozzle Source, Atlanta, GA.

[27] Collard, T. A., and B. A. Jorns (), Nozzle Efficiency in a Low Power Magnetic Nozzle, *Plasma Sources Science and Technology*, p. 30.

[28] Collard, T. A., and B. A. Jorns (2019), Magnetic nozzle efficiency in a low power inductive plasma source, *Plasma Sources Science and Technology*, *28*(10), 105,019, doi:10.1088/1361-6595/ab2d7d.

[29] Correyero, S., J. Jarrige, D. Packan, and E. Ahedo (2018), Ion acceleration in the magnetic nozzle of an ECR thruster: Comparison of experimental measurements with a quasi 1D kinetic model, in *Space Propulsion 2018*, Seville, Spain.

[30] Correyero, S., M. Merino, P.-Q. Elias, J. Jarrige, D. Packan, and E. Ahedo (2019), Characterization of diamagnetism inside an ECR thruster with a diamagnetic loop, *Physics of Plasmas*, *26*(5), 053,511, doi:10.1063/1.5093980.

[31] Courtney, D. G., S. Dandavino, and H. Shea (2016), Comparing Direct and Indirect Thrust Measurements from Passively Fed Ionic Electrospray Thrusters, *Journal of Propulsion and Power*, *32*(2), 392–407, doi:10.2514/1.B35836.

[32] Deline, C. A., R. D. Bengtson, B. N. Breizman, M. R. Tushentsov, J. E. Jones, D. G. Chavers, C. C. Dobson, and B. M. Schuettpelz (2009), Plume detachment from a magnetic nozzle, *Physics of Plasmas*, *16*(3), 033,502, doi:10.1063/1.3080206.

[33] Diamant, K., J. Pollard, M. Crofton, M. Patterson, and G. Soulas (2010), Thrust Stand Characterization of the NASA NEXT Thruster, in *46th AIAA/ASME/SAE/ASEE Joint Propulsion Conference & Exhibit*, American Institute of Aeronautics and Astronautics, Nashville, TN, doi:10.2514/6.2010-6701.

[34] Díaz, F. R. (2000), The Vasimr Rocket, *Scientific American*, *283*(5), 90–97, publisher: Scientific American, a division of Nature America, Inc.

[35] Durot, C. J., B. A. Jorns, E. T. Dale, and A. D. Gallimore (2017), Laser-Induced Fluorescence Measurement of the Anomalous Collision Frequency in a 9-kW Magnetically-Shielded Hall Thruster, Atlanta, GA.

[36] Ebersohn, F. H., J. P. Sheehan, A. D. Gallimore, and J. V. Shebalin (2015), Quasi-one-dimensional particle-in-cell simulation of magnetic nozzles.

[37] Fruchtman, A. (2008), Neutral Depletion in a Collisionless Plasma, *IEEE Transactions on Plasma Science*, *36*(2), 403–413, doi:10.1109/TPS.2008.918777.

[38] Fruchtman, A. (2011), The Thrust of a Collisional-Plasma Source, *IEEE Transactions on Plasma Science*, *39*(1), 530–539, doi:10.1109/TPS.2010.2089067, conference Name: IEEE Transactions on Plasma Science.

[39] Fujiwara, N., T. M. T. Maruyama, and M. Y. M. Yoneda (1996), Pulsed Plasma Processing for Reduction of Profile Distortion Induced by Charge Buildup in Electron Cyclotron Resonance Plasma, *Japanese Journal of Applied Physics*, *35*(4S), 2450, doi:10.1143/JJAP.35.2450, publisher: IOP Publishing.

[40] Geller, R. (1996), *Electron Cyclotron Resonance Ion Sources and ECR Plasmas*, CRC Press, google-Books-ID: DtcVZnquQCAC.

[41] Guaita, M., M. Magarotto, M. Manente, D. Pavarin, and M. Lavagna (2022), Semi-Analytical Model of a Helicon Plasma Thruster, *IEEE Transactions on Plasma Science*, pp. 1–14, doi:10.1109/TPS.2022.3146088, conference Name: IEEE Transactions on Plasma Science.

[42] Gutmann, H.-M. (2001), A Radial Basis Function Method for Global Optimization, *Journal of Global Optimization*, *19*(3), 201–227, doi:10.1023/A:1011255519438.

[43] Hayashi, M. (1983), Determination of electron-xenon total excitation cross-sections, from threshold to 100 eV, from experimental values of Townsend's α, *Journal of Physics D: Applied Physics*, *16*(4), 581–589, doi:10.1088/0022-3727/16/4/018.

[44] Hendel, H., and T. Reboul (1963), CONTINUOUS PLASMA ACCELERATION AT ELECTRON CYCLOTRON RESONANCE, in *Electric Propulsion Conference*, American Institute of Aeronautics and Astronautics, Colorado Springs,CO,U.S.A., doi:10.2514/6.1963-1.

[45] Hepner, S. T., and B. Jorns (2021), Anomalous electron thermal conductivity in a magnetic nozzle, in *AIAA Propulsion and Energy 2021 Forum*, American Institute of Aeronautics and Astronautics, VIRTUAL EVENT, doi:10.2514/6.2021-3399.

[46] Hey, F. G. (2018), *Micro Newton Thruster Development*, Springer Fachmedien Wiesbaden, Wiesbaden, doi:10.1007/978-3-658-21209-4.

[47] Hofer, R. R., and J. R. Anderson (2014), Finite Pressure Effects in Magnetically Shielded Hall Thrusters, in *50th AIAA/ASME/SAE/ASEE Joint Propulsion Conference*, American Institute of Aeronautics and Astronautics, Cleveland, OH, doi:10.2514/6.2014-3709.

[48] Holste, K., et al. (2020), Ion thrusters for electric propulsion: Scientific issues developing a niche technology into a game changer, *Review of Scientific Instruments*, *91*(6), 061,101, doi:10.1063/5.0010134.

[49] Hooper, E. B. (1993), Plasma detachment from a magnetic nozzle, *Journal of Propulsion and Power*, *9*(5), 757–763, doi:10.2514/3.23686.

[50] Hooper, E. B. (1995), Plasma flow resulting from electron cyclotron resonance heating on a magnetic hill, *Physics of Plasmas*, *2*(12), 4563–4569, doi:10.1063/1.871014.

[51] Huang, W. (2011), Study of Hall Thruster Discharge Channel Wall Erosion via Optical Diagnostics, Ph.D. thesis, University of Michigan.

[52] Huang, W., B. Drenkow, and A. Gallimore (2009), Laser-Induced Fluorescence of Singly-Charged Xenon Inside a 6-kW Hall Thruster, in *45th AIAA/ASME/SAE/ASEE Joint Propulsion Conference & Exhibit*, American Institute of Aeronautics and Astronautics, Denver, Colorado, doi:10.2514/6.2009-5355.

[53] Hudson, J., S. Spangelo, A. Hine, D. Kolosa, and K. Lemmer (2016), Mission Analysis for CubeSats with Micropropulsion, *Journal of Spacecraft and Rockets*, *53*(5), 836–846, doi:10.2514/1.A33564.

[54] Jahn, R. G. (2006), *Physics of electric propulsion*, Dover books on physics, dover ed., unabridged republication ed., Dover Publ, Mineola, NY, oCLC: 836917110.

[55] Jarrige, J., P.-Q. Elias, D. Packan, and F. Cannat (2013), Characterization of a coaxial ECR plasma thruster, in *44th AIAA Plasmadynamics and Lasers Conference*, American Institute of Aeronautics and Astronautics, San Diego, CA, doi:10.2514/6.2013-2628.

[56] Jarrige, J., P. Thobois, C. Blanchard, P.-Q. Elias, D. Packan, L. Fallerini, and G. Noci (2014), Thrust Measurements of the Gaia Mission Flight-Model Cold Gas Thrusters, *Journal of Propulsion and Power*, *30*(4), 934–943, doi:10.2514/1.B35091.

[57] Jarrige, J., P.-Q. Elias, and D. Packan (2017), Investigation on the ion velocity distribution in the magnetic nozzle of an ECR plasma thruster using LIF measurements, Atlanta, GA.

[58] Kinder, R. L., and M. J. Kushner (1999), Consequences of mode structure on plasma properties in electron cyclotron resonance sources, *Journal of Vacuum Science & Technology A: Vacuum, Surfaces, and Films*, *17*(5), 2421–2430.

[59] Kosmahl, H. G., D. B. Miller, and G. W. Bethke (1967), Plasma Acceleration with Microwaves near Cyclotron Resonance, *Journal of Applied Physics*, *38*(12), 4576–4582, doi:10.1063/1.1709188.

[60] Krejci, D., and P. Lozano (2018), Space Propulsion Technology for Small Spacecraft, *Proceedings of the IEEE*, *106*(3), 362–378, doi: 10.1109/JPROC.2017.2778747, conference Name: Proceedings of the IEEE.

[61] Krejci, D., A. Reissner, T. Schönherr, B. Seifert, Z. Saleem, and R. Alejos (2019), Recent flight data from IFM Nano Thrusters in a low earth orbit, in *36th International Electric Propulsion Conference*, Vienna, Austria.

[62] Lafleur, T. (2014), Helicon plasma thruster discharge model, *Physics of Plasmas*, *21*(4), 043,507, doi:10.1063/1.4871727.

[63] Lafleur, T., and A. Aanesland (2014), Ambipolar and non-ambipolar diffusion in an rf plasma source containing a magnetic filter, *Physics of Plasmas*, *21*(6), 063,510, doi:10.1063/1.4885109.

[64] Lafleur, T., and N. Apffel (2021), Low-Earth-Orbit Constellation Phasing Using Miniaturized Low-Thrust Propulsion Systems, *Journal of Spacecraft and Rockets*, *58*(3), 628–642, doi:10.2514/1.A34905.

[65] Lafleur, T., C. Charles, and R. W. Boswell (2011), Electron temperature characterization and power balance in a low magnetic field helicon mode, *Journal of Physics D: Applied Physics*, *44*(18), 185,204, doi:10.1088/0022-3727/44/18/185204.

[66] Lafleur, T., F. Cannat, J. Jarrige, P. Q. Elias, and D. Packan (2015), Electron dynamics and ion acceleration in expanding-plasma thrusters, *Plasma Sources Science and Technology*, *24*(6), 065,013, doi:10.1088/0963-0252/24/6/065013.

[67] Lev, D., R. M. Myers, K. M. Lemmer, J. Kolbeck, H. Koizumi, and K. Polzin (2019), The technological and commercial expansion of electric propulsion, *Acta Astronautica*, *159*, 213–227, doi:10.1016/j.actaastro.2019.03.058.

[68] Levchenko, I., et al. (2018), Space micropropulsion systems for Cubesats and small satellites: From proximate targets to furthermost frontiers, *Applied Physics Reviews*, *5*(1), 011,104, doi:10.1063/1.5007734.

[69] Lieberman, M. A., and R. A. Gottscho (1994), Design of High-Density Plasma Sources for Materials Processing, in *Physics of Thin Films*, vol. 18, pp. 1–119, Elsevier, doi:10.1016/B978-0-08-092513-4.50006-4.

[70] Lieberman, M. A., and A. J. Lichtenberg (2005), *Principles of plasma discharges and materials processing*, 2nd ed ed., Wiley-Interscience, Hoboken, N.J, oCLC: ocm56752658.

[71] Little, J. (2015), Performance Scaling of Magnetic Nozzles for Electric Propulsion, Ph.D. thesis.

[72] Little, J. M., and E. Y. Choueiri (2015), Critical condition for plasma confinement in the source of a magnetic nozzle flow, *IEEE Transactions on Plasma Science*, *43*(1), 277–286, doi:10.1109/TPS.2014.2322522.

[73] Little, J. M., and E. Y. Choueiri (2019), Electron Demagnetization in a Magnetically Expanding Plasma, *Physical Review Letters*, *123*(14), 145,001, doi:10.1103/PhysRevLett.123.145001, publisher: American Physical Society.

[74] Longmier, B. W., B. M. Reid, A. D. Gallimore, F. R. Chang-Diaz, J. P. Squire, T. W. Glover, G. Chavers, and E. A. Bering (2009), Validating a Plasma Momentum Flux Sensor to an Inverted Pendulum Thrust Stand, *Journal of Propulsion and Power*, *25*(3), 746–752, doi:10.2514/1.35706.

[75] Longmier, B. W., et al. (2011), Ambipolar ion acceleration in an expanding magnetic nozzle, *Plasma Sources Science and Technology*, *20*(1), 015,007, doi:10.1088/0963-0252/20/1/015007.

[76] Lozano, P. C. (2003), Studies on the Ion-Droplet Mixed Regime in Colloid Thrusters, Ph.D. thesis.

[77] Maimone, F., L. Celona, R. Lang, J. Mäder, J. Roßbach, P. Spädtke, and K. Tinschert (2011), Influence of frequency tuning and double-frequency heating on ions extracted from an electron cyclotron resonance ion source, *Review of Scientific Instruments*, *82*(12), 123,302, doi:10.1063/1.3665673.

[78] Massey, D. R. (2008), Development of a direct evaporation bismuth Hall thruster, Doctor of Philosophy in Mechanical Engineering–Engineering Mechanics, Michigan Technological University, Houghton, Michigan, doi:10.37099/mtu.dc.etds/385.

[79] Mazouffre, S., and L. Grimaud (2018), Characteristics and Performances of a 100-W Hall Thruster for Microspacecraft, *IEEE Transactions on Plasma Science*, *46*(2), 330–337, doi:10.1109/TPS.2017.2786402.

[80] McDonald, M., M. Nurnberger, and L. Williams (2017), Preparations for Thrust Measurement and Error Discussion of the IMPULSE Resonant Microwave Cavity, Atlanta, GA.

[81] Merino, M., and E. Ahedo (2015), Influence of Electron and Ion Thermodynamics on the Magnetic Nozzle Plasma Expansion, *IEEE Transactions on Plasma Science*, *43*(1), 244–251, doi:10.1109/TPS.2014.2316020.

[82] Merino, M., J. Nuez, and E. Ahedo (2021), Fluid-kinetic model of a propulsive magnetic nozzle, *Plasma Sources Science and Technology*, *30*(11), 115,006, doi:10.1088/1361-6595/ac2a0b.

[83] Mikellides, I. G., I. Katz, D. M. Goebel, K. K. Jameson, and J. E. Polk (2008), Wear Mechanisms in Electron Sources for Ion Propulsion, II: Discharge Hollow Cathode, *Journal of Propulsion and Power*, *24*(4), 866–879, doi:10.2514/1.33462.

[84] Miller, J. S., S. H. Pullins, D. J. Levandier, Y.-h. Chiu, and R. A. Dressler (2002), Xenon charge exchange cross sections for electrostatic thruster models, *Journal of Applied Physics*, *91*(3), 984–991, doi:10.1063/1.1426246.

[85] Miller, S., M. L. R. Walker, J. Agolli, and J. Dankanich (2021), Survey and Performance Evaluation of Small-Satellite Propulsion Technologies, *Journal of Spacecraft and Rockets*, *58*(1), 222–231, doi:10.2514/1.A34774.

[86] Morgan, W. L. (1990), Morgan database.

[87] Nagatomo, M. (1967), Plasma acceleration by high frequency electromagnetic wave in staticmagnetic field gradient, in *6th Electric Propulsion and Plasmadynamics Conference*, American Institute of Aeronautics and Astronautics, Colorado Springs,CO,U.S.A., doi:10.2514/6.1967-660.

[88] Nakles, M. R., and W. A. Hargus (2011), Background Pressure Effects on Ion Velocity Distribution Within a Medium-Power Hall Thruster, *Journal of Propulsion and Power*, *27*(4), 737–743, doi:10.2514/1.48027.

[89] Naselli, E., et al. (2019), Impact of two-close-frequency heating on ECR ion source plasma radio emission and stability, *Plasma Sources Science and Technology*, *28*(8), 085,021, doi:10.1088/1361-6595/ab32f9.

[90] Navarro-Cavallé, J., M. Wijnen, P. Fajardo, and E. Ahedo (2018), Experimental characterization of a 1 kW Helicon Plasma Thruster, *Vacuum*, *149*, 69–73, doi:10.1016/j.vacuum.2017.11.036.

[91] Olsen, C. S., et al. (2015), Investigation of Plasma Detachment From a Magnetic Nozzle in the Plume of the VX-200 Magnetoplasma Thruster, *IEEE Transactions on Plasma Science*, *43*(1), 252–268, doi:10.1109/TPS.2014.2321257.

[92] Peterschmitt, S. (2020), Development of a Stable and Efficient Electron Cyclotron Resonance Thruster with Magnetic Nozzle, Ph.D. thesis.

[93] Peterschmitt, S., and D. Packan (2019), Comparison of Waveguide Coupled and Coaxial Coupled ECRA Magnetic Nozzle Thruster using a Thrust Balance, in *36th International Electric Propulsion Conference*.

[94] Peterschmitt, S., and D. Packan (2021), Impact of the Microwave Coupling Structure on an Electron-Cyclotron Resonance Thruster, *Journal of Propulsion and Power*, pp. 1–10, doi:10.2514/1.B38156.

[95] Polk, J. E., A. Pancotti, T. Haag, S. King, M. Walker, J. Blakely, and J. Ziemer (2017), Recommended Practice for Thrust Measurement in Electric Propulsion Testing, *Journal of Propulsion and Power*, *33*(3), 539–555, doi: 10.2514/1.B35564.

[96] Porto, J., and P.-Q. Elias (2019), Full-PIC Simulation of an ECR Plasma Thruster with Magnetic Nozzle, in *36th International Electric Propulsion Conference*, Vienna, Austria.

[97] Pottinger, S., V. Lappas, C. Charles, and R. Boswell (2011), Performance characterization of a helicon double layer thruster using direct thrust measurements, *Journal of Physics D: Applied Physics*, *44*(23), 235,201, doi:10.1088/0022-3727/44/23/235201.

[98] Pottinger, S. J., D. Lamprou, A. K. Knoll, and V. J. Lappas (2012), Impact of plasma noise on a direct thrust measurement system, *Review of Scientific Instruments*, *83*(3), 033,504, doi:10.1063/1.3692740.

[99] Rácz, R., et al. (2018), Effect of the two-close-frequency heating to the extracted ion beam and to the X-ray flux emitted by the ECR plasma, *Journal of Instrumentation*, *13*(12), C12,012–C12,012, doi:10.1088/1748-0221/13/12/C12012.

[100] Rafalskyi, D., et al. (2021), In-orbit demonstration of an iodine electric propulsion system, *Nature*, *599*(7885), 411–415, doi:10.1038/s41586-021-04015-y.

[101] Rosati Azevedo, E., et al. (2021), XJET: Design Upgrade and Preliminary Characterization for an Electrodeless ECR Thruster, Estoril, Portugal.

[102] Sercel, J. (1993), An experimental and theoretical study of the ECR plasma engine, Ph.D. thesis, California Institute of Technology.

[103] Sheehan, J. P., et al. (2014), Temperature gradients due to adiabatic plasma expansion in a magnetic nozzle, *Plasma Sources Science and Technology*, *23*(4), 045,014, doi:10.1088/0963-0252/23/4/045014.

[104] Sheppard, A. J., and J. M. Little (2020), Scaling laws for electrodeless plasma propulsion with water vapor propellant, *Plasma Sources Science and Technology*, *29*(4), 045,007, doi:10.1088/1361-6595/ab759e.

[105] Shimozuma, T., et al. (1997), Development of an ECRH System for Large Helical Device, in *Fusion Technology 1996*, pp. 553–556, Elsevier, doi:10.1016/B978-0-444-82762-3.50108-7.

[106] Siddiqui, M. U., C. Cretel, J. Synowiec, A. G. Hsu, J. A. Young, and R. Spektor (2017), First Performance Measurements of the Phase Four RF Thruster, Atlanta, GA.

[107] Simon, A. (1955), Ambipolar Diffusion in a Magnetic Field, *Physical Review*, *98*(2), 317–318, doi:10.1103/PhysRev.98.317.

[108] Snyder, J. S., G. Lenguito, J. D. Frieman, T. W. Haag, and J. A. Mackey (2020), Effects of Background Pressure on SPT-140 Hall Thruster Performance, *Journal of Propulsion and Power*, *36*(5), 9, doi:10.2514/1.B37702.

[109] Spangelo, S., and B. Longmier (2015), Optimization of CubeSat System-Level Design and Propulsion Systems for Earth-Escape Missions, *Journal of Spacecraft and Rockets*, *52*(4), 1009–1020, doi:10.2514/1.A33136.

[110] Swar, K., D. Staab, A. Garbayo, L. Shadbolt, S. Masillo, A. Lucca Fabris, B. Karadag, and R. Moloney (2019), Design and testing of a uN - mN torsional thrust balance with wireless microwave power transmission, Vienna, Austria.

[111] Takahashi, K. (2019), Helicon-type radiofrequency plasma thrusters and magnetic plasma nozzles, *Reviews of Modern Plasma Physics*, *3*(1), 3, doi:10.1007/s41614-019-0024-2.

[112] Takahashi, K. (2021), Magnetic nozzle radiofrequency plasma thruster approaching twenty percent thruster efficiency, *Scientific Reports*, *11*(1), 2768, doi:10.1038/s41598-021-82471-2.

[113] Takahashi, K., C. Charles, R. Boswell, and A. Ando (2013), Performance improvement of a permanent magnet helicon plasma thruster, *Journal of Physics D: Applied Physics*, *46*(35), 352,001, doi:10.1088/0022-3727/46/35/352001.

[114] Takahashi, K., C. Charles, R. W. Boswell, and A. Ando (2020), Thermodynamic Analogy for Electrons Interacting with a Magnetic Nozzle, *Physical Review Letters*, *125*(16), 165,001, doi:10.1103/PhysRevLett.125.165001.

[115] Takahashi, K., et al. (2011), Direct thrust measurement of a permanent magnet helicon double layer thruster, *Applied Physics Letters*, *98*(14), 141,503, doi:10.1063/1.3577608.

[116] Vialis, T. (2019), Développement d'un propulseur plasma à résonance cyclotron électronique pour les satellites, Ph.D. thesis.

[117] Vialis, T., J. Jarrige, and D. Packan (2017), Geometry optimization and effect of gas propellant in an electron cyclotron resonance plasma thruster, Atlanta, GA.

[118] Vialis, T., J. Jarrige, A. Aanesland, and D. Packan (2018), Direct Thrust Measurement of an Electron Cyclotron Resonance Plasma Thruster, *Journal of Propulsion and Power*, *34*(5), 1323–1333, doi:10.2514/1.B37036.

[119] Viges, E., B. A. Jorns, A. D. Gallimore, and J. P. Sheehan (2019), University of Michigan's Upgraded Large Vacuum Test Facility, Vienna, Austria.

[120] Vinci, A. E., Q. Delavière–Delion, and S. Mazouffre (2022), Electron thermodynamics along magnetic nozzle lines in a helicon plasma, *Journal of Electric Propulsion*, *1*(1), 4, doi:10.1007/s44205-022-00003-0.

[121] Wachs, B., and B. Jorns (2018), Effect of Background Pressure on Ion Dynamics in an Electron Cyclotron Resonance Thruster, in *2018 Joint Propulsion Conference*, American Institute of Aeronautics and Astronautics, Cincinnati, Ohio, doi:10.2514/6.2018-4585.

[122] Wekerle, T., J. B. Pessoa Filho, L. E. V. L. d. Costa, and L. G. Trabasso (2017), Status and Trends of Smallsats and their Launch Vehicles — An Up-to-date Review, *Journal of Aerospace Technology and Management*, *9*(3), 269–286, doi:10.5028/jatm.v9i3.853.

[123] Weng, Y., and M. J. Kushner (1992), Electron energy distributions in electron cyclotron resonance discharges for materials processing, *Journal of applied physics*, *72*(1), 33–42.

[124] Williams, L. T., and M. L. R. Walker (2013), Thrust Measurements of a Radio Frequency Plasma Source, *Journal of Propulsion and Power*, *29*(3), 520–527, doi:10.2514/1.B34574.

[125] Williams, S., and I. Hrbud (2010), RF Cable Heating Effects on a Micronewton-scale Torsional Thrust Stand, in *46th AIAA/ASME/SAE/ASEE Joint Propulsion Conference & Exhibit*, American Institute of Aeronautics and Astronautics, Nashville, TN, doi:10.2514/6.2010-6864.

[126] Wirz, R., J. Polk, C. Marrese, and J. Mueller (2002), Experimental and Computational Investigation of the Performance of a Micro-Ion Thruster, American Institute of Aeronautics and Astronautics, doi:10.2514/6.2002-3835.

[127] Xie, Z. Q., and C. M. Lyneis (1995), Two-frequency plasma heating in a high charge state electron cyclotron resonance ion source, *Review of Scientific Instruments*, *66*(8), 4218–4221, doi:10.1063/1.1145372.